Development of Constraint Force Equation Methodology for Application to Multi-Body Dynamics Including Launch Vehicle Stage Separation

Bandu N. Pamadi, Matthew D. Toniolo, Paul V. Tartabini, Carlos M. Roithmayr,
Cindy W. Albertson and Christopher D. Karlgaard
Langley Research Center, Hampton, Virginia

NASA STI Program . . . in Profile

Since its founding, NASA has been dedicated to the advancement of aeronautics and space science. The NASA scientific and technical information (STI) program plays a key part in helping NASA maintain this important role.

The NASA STI program operates under the auspices of the Agency Chief Information Officer. It collects, organizes, provides for archiving, and disseminates NASA's STI. The NASA STI program provides access to the NTRS Registered and its public interface, the NASA Technical Reports Server, thus providing one of the largest collections of aeronautical and space science STI in the world. Results are published in both non-NASA channels and by NASA in the NASA STI Report Series, which includes the following report types:

- TECHNICAL PUBLICATION. Reports of completed research or a major significant phase of research that present the results of NASA Programs and include extensive data or theoretical analysis. Includes compilations of significant scientific and technical data and information deemed to be of continuing reference value. NASA counter-part of peer-reviewed formal professional papers but has less stringent limitations on manuscript length and extent of graphic presentations.

- TECHNICAL MEMORANDUM. Scientific and technical findings that are preliminary or of specialized interest, e.g., quick release reports, working papers, and bibliographies that contain minimal annotation. Does not contain extensive analysis.

- CONTRACTOR REPORT. Scientific and technical findings by NASA-sponsored contractors and grantees.

- CONFERENCE PUBLICATION. Collected papers from scientific and technical conferences, symposia, seminars, or other meetings sponsored or co-sponsored by NASA.

- SPECIAL PUBLICATION. Scientific, technical, or historical information from NASA programs, projects, and missions, often concerned with subjects having substantial public interest.

- TECHNICAL TRANSLATION. English-language translations of foreign scientific and technical material pertinent to NASA's mission.

Specialized services also include organizing and publishing research results, distributing specialized research announcements and feeds, providing information desk and personal search support, and enabling data exchange services.

For more information about the NASA STI program, see the following:

- Access the NASA STI program home page at http://www.sti.nasa.gov

- E-mail your question to help@sti.nasa.gov

- Phone the NASA STI Information Desk at 757-864-9658

- Write to:
  NASA STI Information Desk
  Mail Stop 148
  NASA Langley Research Center
  Hampton, VA 23681-2199

Development of Constraint Force Equation Methodology for Application to Multi-Body Dynamics Including Launch Vehicle Stage Separation

Bandu N. Pamadi, Matthew D. Toniolo, Paul V. Tartabini, Carlos M. Roithmayr,
Cindy W. Albertson and Christopher D. Karlgaard
Langley Research Center, Hampton, Virginia

Acknowledgments

Available from:

NASA STI Program / Mail Stop 148
NASA Langley Research Center
Hampton, VA 23681-2199
Fax: 757-864-6500

Abstract

The objective of this report is to develop and implement a physics based method for analysis and simulation of multi-body dynamics including launch vehicle stage separation. The constraint force equation (CFE) methodology discussed in this report provides such a framework for modeling constraint forces and moments acting at joints when the vehicles are still connected. Several stand-alone test cases involving various types of joints were developed to validate the CFE methodology. The results were compared with ADAMS® and Autolev, two different industry standard benchmark codes for multi-body dynamic analysis and simulations. However, these two codes are not designed for aerospace flight trajectory simulations. After this validation exercise, the CFE algorithm was implemented in Program to Optimize Simulated Trajectories II (POST2) to provide a capability to simulate end-to-end trajectories of launch vehicles including stage separation. The POST2/CFE methodology was applied to the STS-1 Space Shuttle solid rocket booster (SRB) separation and Hyper-X Research Vehicle (HXRV) separation from the Pegasus booster as a further test and validation for its application to launch vehicle stage separation problems. Finally, to demonstrate end-to-end simulation capability, POST2/CFE was applied to the ascent, orbit insertion, and booster return of a reusable two-stage-to-orbit (TSTO) vehicle concept. With these validation exercises, POST2/CFE software can be used for performing conceptual level end-to-end simulations, including launch vehicle stage separation, for problems similar to those discussed in this report.

THIS PAGE INTENTIONALLY LEFT BLANK

Table of Contents

List of Tables

List of Figures

THIS PAGE INTENTIONALLY LEFT BLANK

Nomenclature

A^*, B^*	mass centers of body A and body B
a_x, a_y, a_z	sensed acceleration components along body axes (excludes gravity) in Space Shuttle SRB separation problem, ft/sec²
$\hat{\mathbf{a}}$	acceleration vectors with components a_x, a_y, a_z
$\hat{\mathbf{a}}_1, \hat{\mathbf{a}}_2, \hat{\mathbf{a}}_3$	unit vectors fixed in body A
$\hat{\mathbf{b}}_1, \hat{\mathbf{b}}_2, \hat{\mathbf{b}}_3$	unit vectors fixed in body B
$\mathbf{e}_A, \mathbf{e}_B$	generic unit vectors fixed in body A and in body B
f	generalized force matrix
$\mathbf{F}^{(CON)}$	joint constraint force vector with components F_x, F_y, F_z
$\mathbf{F}_A^{(EXT)}, \mathbf{F}_B^{(EXT)}$	external force vectors acting on body A and body B, Euclidean vectors, independent of reference frame
g	Baumgarte constraint function
$\mathbf{I}_A, \mathbf{I}_B$	inertia dyadic of body A and body B
I_{xx}, I_{yy}, I_{zz}	moment of inertia about body x, y, and z axes, slugs ft²
l_{ref}	vehicle reference length, ft
M	generalized mass matrix as defined in Eq. (29) and Eq. (71)
m_A, m_B	mass of body A and body B, slugs
$\hat{\mathbf{n}}_1, \hat{\mathbf{n}}_2, \hat{\mathbf{n}}_3$	unit vectors fixed in inertial reference frame
p, q, r	angular velocity components along x, y and z body axes, deg/s
q_i	generalized coordinates, $i = 1, 2, ...$
$\mathbf{r}^{OA^*}$	inertial position vector of mass center of body A, ft
$\mathbf{r}^{OB^*}$	inertial position vector of mass center of body B, ft
$\mathbf{r}^{\bar{A}\bar{\bar{A}}}$	position vector from $\bar{A}$ to $\bar{\bar{A}}$, ft
$\mathbf{T}^{(CON)}$	joint constraint torque vector with components $\mathbf{T}_x, \mathbf{T}_y, \mathbf{T}_z$
u	generalized motion variable matrix with elements u_i, $i = 1, 2, 3 ....$
$\mathbf{v}$	mass center velocity vector, with components v_x, v_y, v_z
$\Delta x, \Delta y, \Delta z$	joint displacements in x, y, z direction, also separation distance between OET and SRBs in x, y, z directions, ft
$\boldsymbol{\alpha}$	angular acceleration vector, rad/sec²
α	matrix defined in Eq. (30)
ϕ, θ, ψ	Euler angles in roll, pitch and yaw, deg
$\Delta\phi, \Delta\theta, \Delta\psi$	joint rotational constraint errors, deg
γ	matrix defined in Eq. (31)
λ	Lagrange multiplier (column matrix)

ω	angular velocity vectors relative to an inertial reference frame with components ω_x, ω_y, ω_z, rad/sec
η	Baumgarte parameter

Suffixes

A, B	body *A*, body *B*
b	body axes system

Acronyms

Abs Max Diff	absolute maximum difference
CFE	constraint force equation
CG	center of gravity
ConSep	Conceptual Separation
DOF	degrees of freedom
ET	external tank
HXLV	Hyper-X launch vehicle
IRVE	Inflatable Reentry Vehicle Experiment
LGBB	Langley Glide Back Booster
LSRB	left solid rocket booster
NASA	National Aeronautics and Space Administration
NGLT	next generation launch technology
OET	Orbiter and external tank
POST2	Program to Optimize Simulated Trajectories II
RKF45	Runge-Kutta-Fehlberg 45 (MATLAB® function)
RSRB	right solid rocket booster
RV	research vehicle
SRB	solid rocket booster
SSME	Space Shuttle main engine
SSTO	single-stage-to-orbit
STS	space transportation system
SVDS	Shuttle vehicle dynamic simulation
TSTO	two-stage-to-orbit

Section 1. Introduction

The problems with the dynamic separation of multiple bodies within the atmosphere are complex and challenging. A few problems that have received significant attention in the literature are the store separation from aircraft (ref. 1), and the separation of the X-15 research vehicle from the B-52 carrier aircraft (ref. 2). For both of these cases, the store and the X-15 vehicle are much smaller in size than the parent vehicle. The other class of stage separation problem involves the separation of two vehicles of comparable sizes as in the case of multi-stage reusable launch vehicles where the integrity of each stage is important after separation. Reference 3 presents a method for computing six degrees of freedom (DOF) trajectories of hinged/linked vehicles. Reference 4 reports a summary of stage separation capabilities in the 1960s and 1970s.

NASA studies on stage separation of multistage reusable launch vehicles date back to the 1960s (refs. 5–9). More recently, Naftel et al. (refs. 10–12) considered the staging of two wing-body vehicles. NASA's Next Generation Launch Technology (NGLT) Program identified stage separation as one of the critical technologies needed for the successful development and operation of next generation multistage reusable launch vehicles (ref. 13). In response to this directive, the stage separation analysis and simulation tool called Conceptual Separation (ConSep) was developed (ref. 14). ConSep is a MATLAB® based front end to the ADAMS® solver, which is an industry standard commercial software for solving dynamics problems involving multiple bodies connected by joints. References 14 and 15 discuss applications of ConSep for two-body (two-stage-to-orbit, TSTO) and three-body (Space Shuttle solid rocket booster, SRB) separations. However, for performing seamless end-to-end simulations of complete launch vehicle trajectories including stage separation, as recommended by the X-43A (Hyper-X) Return-To-Flight Review Board (ref. 16), ADAMS® has to be linked to a trajectory simulation code like the Program to Optimize Simulated Trajectories II (POST2) because POST2 cannot model internal forces and moments at the joints. However, linking ADAMS® (ref. 17) with POST2 for end-to-end simulations is user-intensive and requires elaborate pre and post processing to run ConSep as an interface to ADAMS®. Moreover, linking codes is not generic and typically involves extensive customization for analysis of each stage separation problem. Instead, it would be preferable to have a built-in generic multi-body dynamics simulation capability, including stage separation, as an integral part of trajectory simulation and optimization software like POST2. The availability of such a capability greatly facilitates end-to-end simulation of launch vehicle trajectories and eliminates any chance for possible hand-off errors.

This report discusses application of the constraint force equation (CFE) method for calculating internal constraint forces and constraint moments associated with ideal joints that connect multiple rigid bodies belonging to a flight vehicle. Constraint forces and constraint moments are applied as though they were external forces and moments. The calculations are based on a well-known approach involving Lagrange multipliers, sometimes referred to as undetermined multipliers (refs. 18-20), where the scalar multipliers have very clear relationships to the force and moment vectors as established in ref. 21. Thus, with application of the CFE methodology, the problem of the motion of multiple bodies connected by joints is reduced to one of multiple free body motions subject to the applied external forces and moments and the additional constraint forces and moments computed by CFE. When the joints connecting the vehicles are released, these additional forces and moments vanish, and the vehicles are in free motion. Basically, CFE methodology properly simulates the motion of these bodies in close proximity and assigns proper initial conditions for the free, unconstrained motion of multiple vehicles following joint release. To demonstrate the CFE methodology, several individual test cases were developed featuring various

types of simple joints. To validate CFE methodology, the test case results were compared with those predicted using the ADAMS® solver, except for fixed joint case, where the CFE results were compared with those predicted using AUTOLEV (ref. 22), which is another industry standard software. Having tested and validated each of these cases individually, the concept of a generalized joint was developed that greatly facilitates the use of CFE because the user can simply assign proper DOFs to joints connecting multiple bodies without needing to know the details of CFE methodology.

The CFE methodology discussed in this report is generic and can be implemented and integrated in any trajectory optimization software. This report discusses the implementation of CFE in POST2 (ref. 23), an industry-standard trajectory simulation and optimization software package developed in the early 1970s. Since then, POST2 has been under continuous development and improvement. POST2 can be used to simulate three and six DOF motion for multiple, unconnected free-flying vehicles. For the simulation of launch vehicle staging, it is necessary to model two or more vehicles connected by simple joints, the release of those joints, and the subsequent free flight motion of each body. The current version of POST2 does not have the capability to model internal joint forces and moments prior to separation when the separating bodies are still connected. With CFE implementation, POST2 will have the capability for seamless and efficient end-to-end simulation of launch vehicle trajectories including stage separation. This approach allows the user to use all modeling and optimization features of POST2.

The POST2/CFE methodology has been applied to launch vehicle stage separation problems. Three cases are discussed: (i) the Space Shuttle SRB separation from the Orbiter and external tank (OET), (ii) the Hyper-X research vehicle separation from the Pegasus booster, and, (iii) the end-to-end simulation of a conceptual TSTO Bimese vehicle. For the first two cases, the POST2/CFE predictions are compared with available flight test data. The objective of the third case is to demonstrate the convenience of POST2/CFE for the seamless end-to-end simulation of launch vehicle trajectories including stage separation.

It should be noted that even though emphasis in this report is on the application of CFE methodology to multi-body separation problems, it is not necessary that the bodies become separated during the simulation. The basic CFE methodology is applicable to multiple bodies that stay connected throughout the simulation. Such an application of the CFE algorithm to the IRVE (Inflatable Reentry Vehicle Experiment) vehicle is discussed in ref. 24.

Section 2. Constraint Force Equation Methodology and Implementation in POST2

The basic concept of CFE methodology can be illustrated with the help of an example involving the motion of two rigid bodies A and B connected by a single revolute joint, as shown in Fig. 1(a). The set of external forces acting on A is equivalent to a force $\mathbf{F}_A^{(EXT)}$ applied at A^*, the mass center of A, together with a couple whose torque is $\mathbf{T}_A^{(EXT)}$; this set typically includes gravitational, aerodynamic, and propulsive forces. Similarly, the set of external forces acting on B is equivalent to a force $\mathbf{F}_B^{(EXT)}$ applied at B^*, the mass center of B, together with a couple whose torque is $\mathbf{T}_B^{(EXT)}$. The constraints imposed by the joint are satisfied when a set of internal forces is applied by body A to body B. The set is equivalent to a single constraint force $\mathbf{F}^{(CON)}$ applied at a single point of contact, together with a couple whose torque is $\mathbf{T}^{(CON)}$, as shown in Fig. 1(b). According to the law of action and reaction, a force of equal magnitude and opposite direction, $-\mathbf{F}^{(CON)}$, is applied by B to A, along with a couple whose torque is $-\mathbf{T}^{(CON)}$. The objective of the CFE algorithm is to compute $\mathbf{F}^{(CON)}$ and $\mathbf{T}^{(CON)}$; they depend on the type of joint and the external forces acting on A and B. Figure 1(c) illustrates the way in which the CFE algorithm can be implemented in trajectory simulation software like POST2. At each integration time step, POST2 computes all the external forces and moments acting on each vehicle. This information, along with specific geometric information about the joint, is passed to the CFE algorithm, which works in parallel with POST2. The CFE algorithm computes the internal constraint forces and moments and passes the data back to POST2, which applies them as additional external forces and moments on each body. Thus, the net external forces and moments on each vehicle are the sum of the usual external forces and moments and the joint loads applied to each vehicle as additional external forces and moments. Then, POST2 computes the rotational and translational accelerations of each body, and the solution is propagated in the usual manner with POST2 communicating to CFE at each time step. Consequently, the CFE joint model simply augments the vehicle's external loads and does not require major modification to the equations of motion built in POST2. If the joint connecting the two bodies is released, the constraint forces and moments vanish, and the two bodies move independently of each other.

Two approaches to the CFE method are presented in what follows. The first approach, discussed in Sec. 2.1, is a variation of what the authors reported in Refs. 25 and 26. (Some of the nomenclature and notation in this report differs from what is in Refs. 25 and 26.) In general, it involves a number of unnecessary equations used to indicate an absence of constraint forces and/or constraint torques in certain directions. In contrast, there are no more equations than absolutely necessary in the second approach; it is presented in Sec. 2.2, and is known as the conventional Lagrange multiplier method. In this study, we employ the more computationally efficient Lagrange multiplier method.

(a) External forces and moments.

(b) Internal forces and moments.

(c) Revolute joint implementation.

(d) Translational joint implementation.
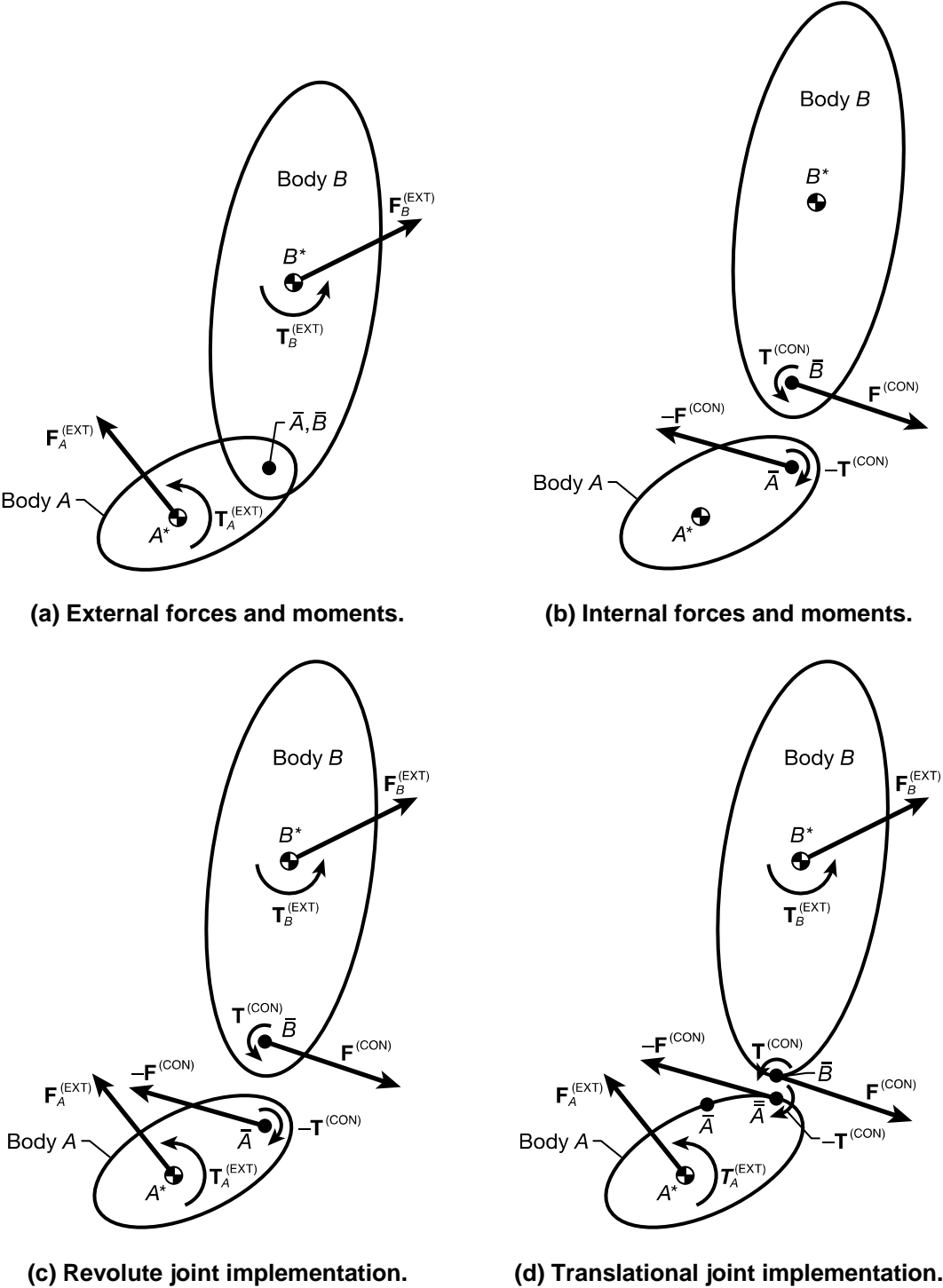
Figure 1. Schematic Illustration of CFE methodology.

2.1   Method I

When two rigid bodies A and B are connected by a single revolute joint as shown in Fig. 1(c), dynamical equations governing constrained motion in an inertial reference frame can be expressed in terms of vectors (denoted by boldface symbols) as follows. For body A,

$$\mathbf{F}_A^{(\text{EXT})} - \mathbf{F}^{(\text{CON})} = m_A\,\mathbf{a}_A \tag{1}$$

$$\mathbf{T}_A^{(\text{EXT})} - \mathbf{r}^{A^*\bar{A}} \times \mathbf{F}^{(\text{CON})} - \mathbf{T}^{(\text{CON})} = \mathbf{I}_A \cdot \boldsymbol{\alpha}_A + \boldsymbol{\omega}_A \times \mathbf{I}_A \cdot \boldsymbol{\omega}_A \tag{2}$$

where m_A is the mass of A, $\boldsymbol{\omega}_A$ is the angular velocity of A in an inertial reference frame, $\boldsymbol{\alpha}_A$ is the angular acceleration of A in an inertial reference frame, $\mathbf{a}_A$ is the acceleration in an inertial reference frame of A^*, the mass center of A, and where $\mathbf{I}_A$ is the inertia dyadic of A with respect to A^*. The position vector from A^* to $\bar{A}$, the joint location of body A, is denoted by $\mathbf{r}^{A^*\bar{A}}$. Likewise, the corresponding equations for body B are

$$\mathbf{F}_B^{(\text{EXT})} + \mathbf{F}^{(\text{CON})} = m_B\,\mathbf{a}_B \tag{3}$$

$$\mathbf{T}_B^{(\text{EXT})} + \mathbf{r}^{B^*\bar{B}} \times \mathbf{F}^{(\text{CON})} + \mathbf{T}^{(\text{CON})} = \mathbf{I}_B \cdot \boldsymbol{\alpha}_B + \boldsymbol{\omega}_B \times \mathbf{I}_B \cdot \boldsymbol{\omega}_B \tag{4}$$

where $\mathbf{r}^{B^*\bar{B}}$ represents the position vector from B^*, the mass center of B, to $\bar{B}$, the joint location of B.

Suppose that the revolute joint is replaced by a joint that permits relative translation between body A and body B as shown in Fig. 1(d). In that case the contact point $\bar{B}$ fixed in B does not in general remain coincident with $\bar{A}$, and $\bar{\bar{A}}$ denotes the point of A that is instantaneously coincident with $\bar{B}$. Because the constraint force $-\mathbf{F}^{(\text{CON})}$ is presumed to be applied to A at $\bar{\bar{A}}$, the moment of this constraint force about A^* is simply $\mathbf{r}^{A^*\bar{\bar{A}}} \times [-\mathbf{F}^{(\text{CON})}]$, and Eq. (2) is replaced with

$$\mathbf{T}_A^{(\text{EXT})} - \mathbf{r}^{A^*\bar{\bar{A}}} \times \mathbf{F}^{(\text{CON})} - \mathbf{T}^{(\text{CON})} = \mathbf{I}_A \cdot \boldsymbol{\alpha}_A + \boldsymbol{\omega}_A \times \mathbf{I}_A \cdot \boldsymbol{\omega}_A \tag{5}$$

In the case of unconstrained motion, $\mathbf{F}^{(\text{CON})}$ and $\mathbf{T}^{(\text{CON})}$ are identically zero and Eqs. (1), (3), (4), and either (2) or (5) reduce to standard dynamical equations of motion for two independent rigid bodies, yielding a total of 12 scalar equations for 12 unknown quantities, namely, three scalars associated with each of the accelerations, $\mathbf{a}_A$ and $\mathbf{a}_B$, and the angular accelerations, $\boldsymbol{\alpha}_A$ and $\boldsymbol{\alpha}_B$. The present method is based on the assumption that during constrained motion there are three additional unknown scalar quantities associated with each of $\mathbf{F}^{(\text{CON})}$ and $\mathbf{T}^{(\text{CON})}$. (In fact, it is well established in the literature that the required number of additional unknowns is equal to the number of independent constraint equations that characterize a joint, and that this number is always less than six.) Hence, we are in search of six additional scalar equations, and they are obtained by considering the joint constraints in the following way. First, form linearly independent constraint equations that describe restrictions imposed by the joint on relative translation and/or relative rotation. Second, consider the translation or rotation that is permitted by the joint, assume the joint is ideal (with perfectly smooth, frictionless bearing surfaces), and write equations that state certain components of $\mathbf{F}^{(\text{CON})}$ and/or $\mathbf{T}^{(\text{CON})}$ are zero.

When a joint constrains relative translation, the distance in a particular direction between $\bar{A}$ and $\bar{B}$ must remain zero; that is,

$$(\mathbf{r}^{O\bar{B}} - \mathbf{r}^{O\bar{A}}) \cdot \mathbf{e}_A = 0 \tag{6}$$

where $\mathbf{r}^{O\bar{B}}$ is the position vector to $\bar{B}$ from a point O fixed in an inertial reference frame, $\mathbf{r}^{O\bar{A}}$ is the position vector from O to $\bar{A}$, and where $\mathbf{e}_A$ is taken to be a unit vector fixed in A in a direction for which translational motion is prohibited by the joint. One relationship having the form of Eq. (6) is needed to account for each direction in which translation is constrained. For example, a fixed joint constrains translation in three orthogonal directions; therefore, three relationships having the form of Eq. (6) are required. In each such equation, the role of $\mathbf{e}_A$ is played by one of three mutually orthogonal unit vectors fixed in A. For a prismatic (sliding) joint that permits translation in only one direction (and restricts translation in two perpendicular directions), two expressions having the form of Eq. (6) are required.

A constraint on relative rotation can be viewed as a requirement that two unit vectors, $\mathbf{e}_A$ and $\mathbf{e}_B$, must remain perpendicular to each other throughout the constrained motion; $\mathbf{e}_A$ is fixed in body A, and $\mathbf{e}_B$ is fixed in body B, such that they are each perpendicular to the axis about which rotation would take place if the constraint were not present. The constraint is expressed by setting the scalar product of the two unit vectors equal to zero,

$$\mathbf{e}_B \cdot \mathbf{e}_A = 0 \tag{7}$$

One relationship having the form of Eq. (7) is required for each direction about which rotation is constrained; no more than three such relationships are associated with any one joint.

Equations (6) and (7) must be differentiated twice with respect to time so that the resulting constraint equations involve the unknown mass center accelerations $\mathbf{a}_A$ and $\mathbf{a}_B$, and angular accelerations $\boldsymbol{\alpha}_A$ and $\boldsymbol{\alpha}_B$, that appear in Eqs. (1), (3), (4), and either (2) or (5). Thus, the second derivatives requiring development are

$$\frac{d^2}{dt^2}\left[(\mathbf{r}^{O\bar{B}} - \mathbf{r}^{O\bar{A}}) \cdot \mathbf{e}_A = 0\right] \tag{8}$$

$$\frac{d^2}{dt^2}(\mathbf{e}_B \cdot \mathbf{e}_A = 0) \tag{9}$$

It is convenient to form the required derivatives by differentiating each vector with respect to time in an inertial reference frame.

Now, the position vector $\mathbf{r}^{O\bar{A}}$ can be written as $\mathbf{r}^{OA^*} + \mathbf{r}^{A^*\bar{A}}$, where $\mathbf{r}^{A^*\bar{A}}$ is a vector fixed in A. The time derivative in an inertial reference frame of $\mathbf{r}^{OA^*}$ is $\mathbf{v}_A$, the velocity of A^* in an inertial reference frame. The time derivatives in an inertial reference frame of $\mathbf{r}^{A^*\bar{A}}$ and $\mathbf{e}_A$ are $\boldsymbol{\omega}_A \times \mathbf{r}^{A^*\bar{A}}$ and $\boldsymbol{\omega}_A \times \mathbf{e}_A$, respectively. The time derivatives of $\mathbf{r}^{O\bar{B}}$ and $\mathbf{e}_B$ can be treated similarly. Hence, the result of differentiating Eq. (6) once is

$$\left(\mathbf{v}_B + \boldsymbol{\omega}_B \times \mathbf{r}^{B^*\bar{B}} - \mathbf{v}_A - \boldsymbol{\omega}_A \times \mathbf{r}^{A^*\bar{A}}\right) \cdot \mathbf{e}_A + \left(\mathbf{r}^{O\bar{B}} - \mathbf{r}^{O\bar{A}}\right) \cdot (\boldsymbol{\omega}_A \times \mathbf{e}_A) = 0 \tag{10}$$

The second differentiation yields

$$
\begin{aligned}
\left(\mathbf{a}_B + \boldsymbol{\alpha}_B \times \mathbf{r}^{B^*\bar{B}} + \boldsymbol{\omega}_B \times \boldsymbol{\omega}_B \times \mathbf{r}^{B^*\bar{B}} - \mathbf{a}_A - \boldsymbol{\alpha}_A \times \mathbf{r}^{A^*\bar{A}} - \boldsymbol{\omega}_A \times \boldsymbol{\omega}_A \times \mathbf{r}^{A^*\bar{A}}\right) \cdot \mathbf{e}_A & \\
+ 2\left(\mathbf{v}_B + \boldsymbol{\omega}_B \times \mathbf{r}^{B^*\bar{B}} - \mathbf{v}_A - \boldsymbol{\omega}_A \times \mathbf{r}^{A^*\bar{A}}\right) \cdot (\boldsymbol{\omega}_A \times \mathbf{e}_A) & \\
+ \left(\mathbf{r}^{O\bar{B}} - \mathbf{r}^{O\bar{A}}\right) \cdot (\boldsymbol{\alpha}_A \times \mathbf{e}_A + \boldsymbol{\omega}_A \times \boldsymbol{\omega}_A \times \mathbf{e}_A) &= 0
\end{aligned}
\tag{11}
$$

An alternative form of Eq. (11) will prove useful in Sec. 2.3. It is obtained by making use of relationships involving position vectors,

$$
\mathbf{r}^{O\bar{B}} - \mathbf{r}^{O\bar{A}} = \mathbf{r}^{\overline{AB}}
\tag{12}
$$

$$
\mathbf{r}^{A^*\bar{A}} + \mathbf{r}^{\overline{AB}} = \mathbf{r}^{A^*\bar{B}}
\tag{13}
$$

and identities for scalar triple products,

$$
\mathbf{a} \cdot \mathbf{b} \times \mathbf{c} = \mathbf{a} \times \mathbf{b} \cdot \mathbf{c} = -\mathbf{b} \times \mathbf{a} \cdot \mathbf{c} = -\mathbf{b} \cdot \mathbf{a} \times \mathbf{c}
\tag{14}
$$

to write

$$
\left(\mathbf{r}^{O\bar{B}} - \mathbf{r}^{O\bar{A}}\right) \cdot (\boldsymbol{\alpha}_A \times \mathbf{e}_A) = \mathbf{r}^{\overline{AB}} \cdot (\boldsymbol{\alpha}_A \times \mathbf{e}_A) = -\boldsymbol{\alpha}_A \times \mathbf{r}^{\overline{AB}} \cdot \mathbf{e}_A
\tag{15}
$$

and

$$
\begin{aligned}
-\left(\boldsymbol{\alpha}_A \times \mathbf{r}^{A^*\bar{A}}\right) \cdot \mathbf{e}_A + \left(\mathbf{r}^{O\bar{B}} - \mathbf{r}^{O\bar{A}}\right) \cdot (\boldsymbol{\alpha}_A \times \mathbf{e}_A) & \\
= -\left(\boldsymbol{\alpha}_A \times \mathbf{r}^{A^*\bar{A}}\right) \cdot \mathbf{e}_A - \boldsymbol{\alpha}_A \times \mathbf{r}^{\overline{AB}} \cdot \mathbf{e}_A & \\
= -\boldsymbol{\alpha}_A \times \left(\mathbf{r}^{A^*\bar{A}} + \mathbf{r}^{\overline{AB}}\right) \cdot \mathbf{e}_A & \\
= -\boldsymbol{\alpha}_A \times \mathbf{r}^{A^*\bar{B}} \cdot \mathbf{e}_A &
\end{aligned}
\tag{16}
$$

Hence, Eq. (11) can also be expressed as

$$
\begin{aligned}
\left(\mathbf{a}_B + \boldsymbol{\alpha}_B \times \mathbf{r}^{B^*\bar{B}} + \boldsymbol{\omega}_B \times \boldsymbol{\omega}_B \times \mathbf{r}^{B^*\bar{B}} - \mathbf{a}_A - \boldsymbol{\alpha}_A \times \mathbf{r}^{A^*\bar{B}} - \boldsymbol{\omega}_A \times \boldsymbol{\omega}_A \times \mathbf{r}^{A^*\bar{A}}\right) \cdot \mathbf{e}_A & \\
+ 2\left(\mathbf{v}_B + \boldsymbol{\omega}_B \times \mathbf{r}^{B^*\bar{B}} - \mathbf{v}_A - \boldsymbol{\omega}_A \times \mathbf{r}^{A^*\bar{A}}\right) \cdot (\boldsymbol{\omega}_A \times \mathbf{e}_A) & \\
+ \mathbf{r}^{\bar{A}\bar{B}} \cdot (\boldsymbol{\omega}_A \times \boldsymbol{\omega}_A \times \mathbf{e}_A) &= 0
\end{aligned}
\tag{17}
$$

As for the rotational constraint, differentiating the terms in Eq. (7) once with respect to time yields

$$
(\boldsymbol{\omega}_B \times \mathbf{e}_B) \cdot \mathbf{e}_A + \mathbf{e}_B \cdot (\boldsymbol{\omega}_A \times \mathbf{e}_A) = 0
\tag{18}
$$

In view of identities for scalar triple products, the two terms in the left-hand member can be written as

$$
(\boldsymbol{\omega}_B \times \mathbf{e}_B) \cdot \mathbf{e}_A = \boldsymbol{\omega}_B \cdot \mathbf{e}_B \times \mathbf{e}_A
\tag{19}
$$

and

$$\mathbf{e}_B \cdot (\boldsymbol{\omega}_A \times \mathbf{e}_A) = -\boldsymbol{\omega}_A \cdot \mathbf{e}_B \times \mathbf{e}_A \tag{20}$$

Hence, Eq. (18) can be restated as

$$(\boldsymbol{\omega}_B - \boldsymbol{\omega}_A) \cdot (\mathbf{e}_B \times \mathbf{e}_A) = 0 \tag{21}$$

Differentiating once more gives

$$(\boldsymbol{\alpha}_B - \boldsymbol{\alpha}_A) \cdot (\mathbf{e}_B \times \mathbf{e}_A) + (\boldsymbol{\omega}_B - \boldsymbol{\omega}_A) \cdot [(\boldsymbol{\omega}_B \times \mathbf{e}_B) \times \mathbf{e}_A + \mathbf{e}_B \times (\boldsymbol{\omega}_A \times \mathbf{e}_A)] = 0 \tag{22}$$

When relative translation is permitted in a certain direction, an equation having the form of Eq. (11) is not applicable in that direction. Likewise, when relative rotation is allowed, a relationship having the form of Eq. (22) is not applicable. Instead, the required equations can be obtained using the condition that the constraint force or torque is zero in those directions (with the assumption that the surfaces of the joint are perfectly smooth) in which free translation or rotation is permitted. Thus, for a joint that permits translation in a certain direction parallel to the vector $\mathbf{e}$,

$$\mathbf{F}^{(\text{CON})} \cdot \mathbf{e} = 0 \tag{23}$$

Similarly, when a joint permits relative rotation about an axis parallel to the vector $\mathbf{e}$,

$$\mathbf{T}^{(\text{CON})} \cdot \mathbf{e} = 0 \tag{24}$$

As may be noted in Sec. 2.2, the Lagrange multiplier method does not require the use of equations having the form of (23) and (24).

In summary, equations having the form of (11) and (22)–(24) provide, in combination, a total of six remaining equations.

The 18 scalar equations formed from Eqs. (1), (3), (4), (11), (22)–(24), and either (2) or (5), are linear in 18 unknowns. Three variables represent each of the two mass center accelerations, each of the two rigid body angular accelerations, the constraint force, and the constraint torque, for a total of 18 unknowns. These equations can be expressed in matrix form as $Ax = b$ (where the column matrix x contains the 18 unknown parameters) and solved using standard matrix inversion techniques. A variation of this formulation was presented in Refs. 25 and 26 and applied to the case of two bodies connected by a fixed joint, as well as the problem of separation of the Hyper-X vehicle from the Pegasus booster. Both of these cases are included in this report and discussed in Secs. 3.1.1 and 4.2, respectively.

2.2 Method II: Lagrange Multiplier Method

As mentioned in connection with Eqs. (1)–(5), dynamical equations governing the unconstrained motion of bodies A and B can be expressed in vector form as

$$\mathbf{F}_A^{(\text{EXT})} = m_A \, \mathbf{a}_A \tag{25}$$

$$\mathbf{T}_A^{(\text{EXT})} = \mathbf{I}_A \cdot \boldsymbol{\alpha}_A + \boldsymbol{\omega}_A \times \mathbf{I}_A \cdot \boldsymbol{\omega}_A \tag{26}$$

$$\mathbf{F}_B^{(\text{EXT})} = m_B\, \mathbf{a}_B \tag{27}$$

$$\mathbf{T}_B^{(\text{EXT})} = \mathbf{I}_B \cdot \boldsymbol{\alpha}_B + \boldsymbol{\omega}_B \times \mathbf{I}_B \cdot \boldsymbol{\omega}_B \tag{28}$$

In general, the collection of dynamical differential equations governing unconstrained motion of A, B, and other rigid bodies can be written in matrix form as

$$M\dot{u} = f \tag{29}$$

where M is a square generalized mass matrix, $\dot{u}$ is a column matrix containing generalized accelerations, and f is a column matrix containing generalized forces, nonlinear terms arising from gyroscopic torque, etc. The object of the CFE method is to modify Eqs. (29) such that they become applicable when rigid bodies are connected by joints. The modification is carried out using a well-known approach involving Lagrange multipliers, sometimes referred to as undetermined multipliers,

$$M\dot{u} = f + \alpha^T \lambda \tag{30}$$

where λ is a column matrix containing the multipliers. Linearly independent equations describing the constraints imposed by the joints are written in matrix form as

$$\alpha\dot{u} + \gamma = 0 \tag{31}$$

where γ is a column matrix, and the right-hand member is a column matrix whose elements are all zero. The matrix α^T appearing in Eqs. (30) is the transpose of the coefficient matrix α in Eqs. (31). (Bold font and a subscript are used to distinguish angular acceleration, $\boldsymbol{\alpha}_A$ for example, from the coefficient matrix α.) The product $\alpha^T \lambda$ is a column matrix containing generalized constraint forces. Equations (30) can be solved for $\dot{u}$,

$$\dot{u} = M^{-1}(f + \alpha^T \lambda) \tag{32}$$

and substitution from Eqs. (32) into (31) yields

$$\alpha M^{-1}(f + \alpha^T \lambda) + \gamma = 0 \tag{33}$$

or

$$\alpha M^{-1}\alpha^T \lambda = -(\gamma + \alpha M^{-1} f)$$

Hence,

$$\lambda = -(\alpha M^{-1}\alpha^T)^{-1}(\gamma + \alpha M^{-1} f) \tag{34}$$

The number of multipliers in the matrix λ is exactly equal to the number of constraint equations (31).

2.3   Constraint Equations in Matrix Form

Constraint equations given in vector form in Sec. 2.1 can be rewritten in matrix form as stated in Eqs. (31). Examples are now given using the acceleration-level relationships for a translational constraint, Eq. (11), and a rotational constraint, Eq. (22). A system of two bodies performing unconstrained motion in an inertial reference frame possesses 12 degrees of freedom; thus, for two constraints, α is a 2×12 matrix, $\dot{u}$ is a 12×1 column matrix, and γ is a 2×1 column matrix.

Let $\hat{\mathbf{n}}_r$ ($r = 1,2,3$) be a set of right-handed, mutually orthogonal unit vectors fixed in an inertial reference frame, and let unit vectors $\hat{\mathbf{a}}_r$ and $\hat{\mathbf{b}}_r$ ($r = 1,2,3$) be two similar sets fixed in A and in B, respectively. The velocity $\mathbf{v}_A$ of the mass center of A in an inertial reference frame can be written in terms of $\hat{\mathbf{n}}_1, \hat{\mathbf{n}}_2,$ and $\hat{\mathbf{n}}_3$,

$$\mathbf{v}_A = u_1\hat{\mathbf{n}}_1 + u_2\hat{\mathbf{n}}_2 + u_3\hat{\mathbf{n}}_3 \tag{35}$$

The angular velocity $\boldsymbol{\omega}_A$ of A in an inertial reference frame can be expressed in terms of $\hat{\mathbf{a}}_1, \hat{\mathbf{a}}_2,$ and $\hat{\mathbf{a}}_3$,

$$\boldsymbol{\omega}_A = u_4\hat{\mathbf{a}}_1 + u_5\hat{\mathbf{a}}_2 + u_6\hat{\mathbf{a}}_3 \tag{36}$$

The acceleration $\mathbf{a}_A$ of the mass center of A in an inertial reference frame is then given by

$$\mathbf{a}_A = \dot{u}_1\hat{\mathbf{n}}_1 + \dot{u}_2\hat{\mathbf{n}}_2 + \dot{u}_3\hat{\mathbf{n}}_3 \tag{37}$$

The angular acceleration $\boldsymbol{\alpha}_A$ of A in an inertial reference frame is

$$\boldsymbol{\alpha}_A = \left(\frac{d\boldsymbol{\omega}_A}{dt}\right)_A + \boldsymbol{\omega}_A \times \boldsymbol{\omega}_A = \left(\frac{d\boldsymbol{\omega}_A}{dt}\right)_A + \mathbf{0} = \dot{u}_4\hat{\mathbf{a}}_1 + \dot{u}_5\hat{\mathbf{a}}_2 + \dot{u}_6\hat{\mathbf{a}}_3 \tag{38}$$

where $(d/dt)_A$ represents differentiation with respect to time in reference frame A. Corresponding quantities associated with B are written similarly,

$$\mathbf{v}_B = u_7\hat{\mathbf{n}}_1 + u_8\hat{\mathbf{n}}_2 + u_9\hat{\mathbf{n}}_3 \qquad \boldsymbol{\omega}_B = u_{10}\hat{\mathbf{b}}_1 + u_{11}\hat{\mathbf{b}}_2 + u_{12}\hat{\mathbf{b}}_3 \tag{39}$$

$$\mathbf{a}_B = \dot{u}_7\hat{\mathbf{n}}_1 + \dot{u}_8\hat{\mathbf{n}}_2 + \dot{u}_9\hat{\mathbf{n}}_3 \qquad \boldsymbol{\alpha}_B = \dot{u}_{10}\hat{\mathbf{b}}_1 + \dot{u}_{11}\hat{\mathbf{b}}_2 + \dot{u}_{12}\hat{\mathbf{b}}_3 \tag{40}$$

A constraint on translation is chosen as the first constraint in the present example. Upon substitution from Eqs. (35)–(40) into (17), one can inspect the result to identify the coefficient $\alpha_{1,r}$ of $\dot{u}_r$ for $r = 1, \dots, 12$ to form the first row of the matrix α.

$$\alpha_{1,1} = -\hat{\mathbf{n}}_1 \cdot \mathbf{e}_A \qquad \alpha_{1,2} = -\hat{\mathbf{n}}_2 \cdot \mathbf{e}_A \qquad \alpha_{1,3} = -\hat{\mathbf{n}}_3 \cdot \mathbf{e}_A \tag{41}$$

$$\alpha_{1,4} = -\hat{\mathbf{a}}_1 \times \mathbf{r}^{A^*\bar{B}} \cdot \mathbf{e}_A \qquad \alpha_{1,5} = -\hat{\mathbf{a}}_2 \times \mathbf{r}^{A^*\bar{B}} \cdot \mathbf{e}_A \qquad \alpha_{1,6} = -\hat{\mathbf{a}}_3 \times \mathbf{r}^{A^*\bar{B}} \cdot \mathbf{e}_A \tag{42}$$

$$\alpha_{1,7} = \hat{\mathbf{n}}_1 \cdot \mathbf{e}_A \qquad \alpha_{1,8} = \hat{\mathbf{n}}_2 \cdot \mathbf{e}_A \qquad \alpha_{1,9} = \hat{\mathbf{n}}_3 \cdot \mathbf{e}_A \tag{43}$$

$$\alpha_{1,10} = \hat{\mathbf{b}}_1 \times \mathbf{r}^{B^*\bar{B}} \cdot \mathbf{e}_A \qquad \alpha_{1,11} = \hat{\mathbf{b}}_2 \times \mathbf{r}^{B^*\bar{B}} \cdot \mathbf{e}_A \qquad \alpha_{1,12} = \hat{\mathbf{b}}_3 \times \mathbf{r}^{B^*\bar{B}} \cdot \mathbf{e}_A \tag{44}$$

The first element γ_1 of the matrix γ consists of all terms in Eq. (17) that do not involve $\dot{u}_1, \dots, \dot{u}_{12}$.

$$\begin{aligned}
\gamma_1 = \left(\boldsymbol{\omega}_B \times \boldsymbol{\omega}_B \times \mathbf{r}^{B^*\bar{B}} - \boldsymbol{\omega}_A \times \boldsymbol{\omega}_A \times \mathbf{r}^{A^*\bar{A}}\right) \cdot \mathbf{e}_A \\
+ 2\left(\mathbf{v}_B + \boldsymbol{\omega}_B \times \mathbf{r}^{B^*\bar{B}} - \mathbf{v}_A - \boldsymbol{\omega}_A \times \mathbf{r}^{A^*\bar{A}}\right) \cdot (\boldsymbol{\omega}_A \times \mathbf{e}_A) \\
+ \mathbf{r}^{\overline{AB}} \cdot (\boldsymbol{\omega}_A \times \boldsymbol{\omega}_A \times \mathbf{e}_A)
\end{aligned} \tag{45}$$

In the current example a constraint on rotation is chosen as the second constraint, and substitution from Eqs. (35)–(40) into (22) yields a result that is inspected to identify the coefficient $\alpha_{2,r}$ of $\dot{u}_r$ for $r = 1, \dots, 12$ to form the second row of the matrix α.

$$\alpha_{2,1} = 0 \qquad \alpha_{2,2} = 0 \qquad \alpha_{2,3} = 0 \tag{46}$$

$$\alpha_{2,4} = -\hat{\mathbf{a}}_1 \cdot \mathbf{e}_B \times \mathbf{e}_A \qquad \alpha_{2,5} = -\hat{\mathbf{a}}_2 \cdot \mathbf{e}_B \times \mathbf{e}_A \qquad \alpha_{2,6} = -\hat{\mathbf{a}}_3 \cdot \mathbf{e}_B \times \mathbf{e}_A \tag{47}$$

$$\alpha_{2,7} = 0 \qquad \alpha_{2,8} = 0 \qquad \alpha_{2,9} = 0 \tag{48}$$

$$\alpha_{2,10} = \hat{\mathbf{b}}_1 \cdot \mathbf{e}_B \times \mathbf{e}_A \qquad \alpha_{2,11} = \hat{\mathbf{b}}_2 \cdot \mathbf{e}_B \times \mathbf{e}_A \qquad \alpha_{2,12} = \hat{\mathbf{b}}_3 \cdot \mathbf{e}_B \times \mathbf{e}_A \tag{49}$$

The second element γ_2 of the matrix γ consists of all terms in Eq. (22) that do not involve $\dot{u}_1, \dots, \dot{u}_{12}$.

$$\gamma_2 = (\boldsymbol{\omega}_B - \boldsymbol{\omega}_A) \cdot [(\boldsymbol{\omega}_B \times \mathbf{e}_B) \times \mathbf{e}_A + \mathbf{e}_B \times (\boldsymbol{\omega}_A \times \mathbf{e}_A)] \tag{50}$$

2.4   Baumgarte Constraint Stabilization Method

The matrices M, f, α, and γ are used together with Eqs. (34) to determine values of the multipliers needed to enforce the constraints at any instant of time. With the column matrix $\alpha^T \lambda$ containing the generalized constraint forces in hand, constrained motion can be simulated by performing numerical integration of Eqs. (30) and an appropriate set of kinematical differential equations. However, the numerical solution is sensitive to computational errors and initial joint misalignment errors. The accumulation of the numerical errors may lead to a significant joint displacement or misalignment over time, an artifact referred to as constraint drift. In order to control constraint drift, the CFE algorithm employs a technique known as Baumgarte stabilization (Ref. 27), which is applicable to methods I and II.

The constraint equations (31) can be expressed as

$$\alpha \dot{u} + \gamma = \ddot{g} = 0 \tag{51}$$

where 0 is a column matrix whose elements are all zero, and where g is a column matrix containing the left-hand members of (non-differentiated) configuration constraint relationships obtained from Eqs. (6) and (7). The stabilization technique is implemented by augmenting Eqs. (51) with terms involving the once-differentiated and non-differentiated forms of g:

$$\ddot{g} + 2\eta \dot{g} + \eta^2 g = 0 \tag{52}$$

Thus, the new constraint relations in Eqs. (52) make use of all three forms of the constraint equations to produce behavior of damped, second-order systems with a damping ratio of 1. The stiffness, which determines frequency, is represented by η, a scalar constant whose value is selected by the analyst to control the constraint drift. Reference 27 suggests values of η ranging from 0 to 10. Substitution from Eqs. (51) into (52) yields

$$\alpha \dot{u} + \gamma + 2\eta \dot{g} + \eta^2 g = 0 \tag{53}$$

In other words, the Baumgarte method consists of replacing Eqs. (31) with relationships expressed as

$$\alpha \dot{u} + \gamma' = 0 \tag{54}$$

where

$$\gamma' = \gamma + 2\eta \dot{g} + \eta^2 g \tag{55}$$

As in Sec. 2.3, a translational constraint and a rotational constraint can be used as examples to demonstrate how to form 2×1 column matrices g, $\dot{g}$, and $\ddot{g}$. In the case of a translational constraint, refer to Eq. (6) to write the position-level constraint as

$$g_1(t) = \left(\mathbf{r}^{O\bar{B}} - \mathbf{r}^{O\bar{A}}\right) \cdot \mathbf{e}_A = 0 \tag{56}$$

Refer to Eq. (10) to express the corresponding velocity-level constraint as

$$\dot{g}_1(t) = \left(\mathbf{v}_B + \boldsymbol{\omega}_B \times \mathbf{r}^{B^*\bar{B}} - \mathbf{v}_A - \boldsymbol{\omega}_A \times \mathbf{r}^{A^*\bar{A}}\right) \cdot \mathbf{e}_A + \left(\mathbf{r}^{O\bar{B}} - \mathbf{r}^{O\bar{A}}\right) \cdot \left(\boldsymbol{\omega}_A \times \mathbf{e}_A\right) = 0 \tag{57}$$

Finally, the acceleration-level constraint is obtained from Eq. (11),

$$\ddot{g}_1(t) = \left(\mathbf{a}_B + \boldsymbol{\alpha}_B \times \mathbf{r}^{B^*\bar{B}} + \boldsymbol{\omega}_B \times \boldsymbol{\omega}_B \times \mathbf{r}^{B^*\bar{B}} - \mathbf{a}_A - \boldsymbol{\alpha}_A \times \mathbf{r}^{A^*\bar{A}} - \boldsymbol{\omega}_A \times \boldsymbol{\omega}_A \times \mathbf{r}^{A^*\bar{A}}\right) \cdot \mathbf{e}_A$$
$$+ 2\left(\mathbf{v}_B + \boldsymbol{\omega}_B \times \mathbf{r}^{B^*\bar{B}} - \mathbf{v}_A - \boldsymbol{\omega}_A \times \mathbf{r}^{A^*\bar{A}}\right) \cdot \left(\boldsymbol{\omega}_A \times \mathbf{e}_A\right)$$
$$+ \left(\mathbf{r}^{O\bar{B}} - \mathbf{r}^{O\bar{A}}\right) \cdot \left(\boldsymbol{\alpha}_A \times \mathbf{e}_A + \boldsymbol{\omega}_A \times \boldsymbol{\omega}_A \times \mathbf{e}_A\right) = 0 \tag{58}$$

Similarly, the rotational constraint at the position, velocity, and acceleration levels are obtained from Eqs. (7), (21), and (22), respectively.

$$g_2(t) = \mathbf{e}_B \cdot \mathbf{e}_A = 0 \tag{59}$$

$$\dot{g}_2(t) = \left(\boldsymbol{\omega}_B - \boldsymbol{\omega}_A\right) \cdot \left(\mathbf{e}_B \times \mathbf{e}_A\right) = 0 \tag{60}$$

$$\ddot{g}_2(t) = \left(\boldsymbol{\alpha}_B - \boldsymbol{\alpha}_A\right) \cdot \left(\mathbf{e}_B \times \mathbf{e}_A\right) + \left(\boldsymbol{\omega}_B - \boldsymbol{\omega}_A\right) \cdot \left[\left(\boldsymbol{\omega}_B \times \mathbf{e}_B\right) \times \mathbf{e}_A + \mathbf{e}_B \times \left(\boldsymbol{\omega}_A \times \mathbf{e}_A\right)\right] = 0 \tag{61}$$

2.5   Planar Motion of Two Bodies Constrained by Slider Joint

Use of the relationships presented in the preceding sections is illustrated with an example involving planar motion of two rigid bodies connected by a slider joint. Let $\hat{n}_r$ (r = 1,2,3) be a set of right-handed, mutually orthogonal unit vectors fixed in an inertial reference frame such that $\hat{n}_1$ and $\hat{n}_2$ lie in the plane of motion, as shown in Fig. 2, and $\hat{n}_3$ is perpendicular to the plane. Let unit vectors $\hat{a}_r$ and $\hat{b}_r$ (r = 1,2,3) be two similar sets fixed in A and in B, respectively, with $\hat{a}_3$ and $\hat{b}_3$ each parallel to a central principal axis of inertia of the body in which it is fixed.

Motion of A is regarded as unconstrained when the mass center A^* can translate in the plane, and the body can rotate about an axis parallel to $\hat{\mathbf{n}}_3$. Likewise, B is unconstrained when it can move completely independently of A. Thus, the unconstrained system possesses six degrees of freedom in an inertial reference frame, and six generalized coordinates $q_1, \dots, q_6$ are required to specify the configuration of the system. These coordinates are defined operationally by writing

$$\mathbf{r}^{OA^*} \triangleq q_1\hat{\mathbf{n}}_1 + q_2\hat{\mathbf{n}}_2 \qquad \hat{\mathbf{a}}_1 \cdot \hat{\mathbf{n}}_1 \triangleq \cos\, q_3 \tag{62}$$

$$\mathbf{r}^{OB^*} \triangleq q_4\hat{\mathbf{n}}_1 + q_5\hat{\mathbf{n}}_2 \qquad \hat{\mathbf{b}}_1 \cdot \hat{\mathbf{n}}_1 \triangleq \cos\, q_6 \tag{63}$$

where, $\mathbf{r}^{OA^*}$ and $\mathbf{r}^{OB^*}$ denote the position vectors to A^* and B^*, respectively, from a point O fixed in an inertial reference frame. Translational coordinates q_1, q_2, q_4, and q_5 are indicated in Fig. 2, as are angles q_3 and q_6. It will prove useful in what follows to refer to direction cosine matrices that indicate how unit vectors $\hat{\mathbf{a}}_r$ and $\hat{\mathbf{b}}_r$, respectively, are related to $\hat{\mathbf{n}}_r$ (r = 1,2,3).
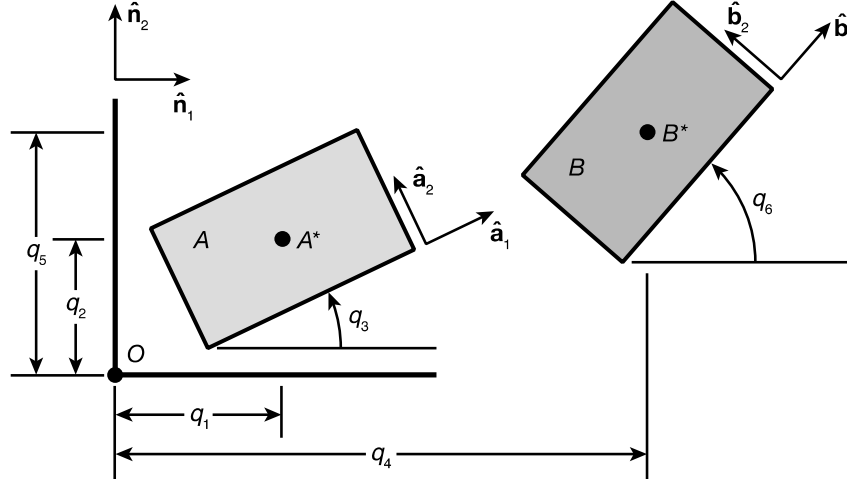

**Figure 2.   Unconstrained planar motion of two bodies
A and *B* in inertial reference system.**

Six motion variables $u_1, \dots, u_6$ can be defined with the kinematical differential equations

$$u_r \triangleq \dot{q}_r \qquad (r = 1, \dots, 6) \tag{64}$$

and subsequently used to write

$$\mathbf{v}_A = u_1\hat{\mathbf{n}}_1 + u_2\hat{\mathbf{n}}_2 \qquad \boldsymbol{\omega}_A = u_3\hat{\mathbf{a}}_3 = u_3\hat{\mathbf{n}}_3 \tag{65}$$

$$\mathbf{a}_A = \dot{u}_1\hat{\mathbf{n}}_1 + \dot{u}_2\hat{\mathbf{n}}_2 \qquad \boldsymbol{\alpha}_A = \dot{u}_3\hat{\mathbf{a}}_3 = \dot{u}_3\hat{\mathbf{n}}_3 \tag{66}$$

$$\mathbf{v}_B = u_4\hat{\mathbf{n}}_1 + u_5\hat{\mathbf{n}}_2 \qquad \boldsymbol{\omega}_B = u_6\hat{\mathbf{b}}_3 = u_6\hat{\mathbf{n}}_3 \tag{67}$$

$$\mathbf{a}_B = \dot{u}_4\hat{\mathbf{n}}_1 + \dot{u}_5\hat{\mathbf{n}}_2 \qquad \boldsymbol{\alpha}_B = \dot{u}_6\hat{\mathbf{b}}_3 = \dot{u}_6\hat{\mathbf{n}}_3 \tag{68}$$

The external forces $\mathbf{F}_A^{(\text{EXT})}$ and $\mathbf{F}_B^{(\text{EXT})}$, as well as the external torques $\mathbf{T}_A^{(\text{EXT})}$ and $\mathbf{T}_B^{(\text{EXT})}$, can be expressed as

$$\mathbf{F}_A^{(EXT)} = \sigma_1\hat{\mathbf{n}}_1 + \sigma_2\hat{\mathbf{n}}_2 \qquad \mathbf{T}_A^{(\text{EXT})} = \sigma_3\hat{\mathbf{a}}_3 = \sigma_3\hat{\mathbf{n}}_3 \tag{69}$$

$$\mathbf{F}_B^{(\text{EXT})} = \sigma_4\hat{\mathbf{n}}_1 + \sigma_5\hat{\mathbf{n}}_2 \qquad \mathbf{T}_B^{(\text{EXT})} = \sigma_6\hat{\mathbf{b}}_3 = \sigma_6\hat{\mathbf{n}}_3 \tag{70}$$

This brings one into position to use Eqs. (25) and (26) for A, together with Eqs. (27) and (28) for B, to identify the matrices M, $\dot{u}$, and f appearing in Eqs. (29),

$$M = \begin{bmatrix} m_A & 0 & 0 & 0 & 0 & 0 \\ 0 & m_A & 0 & 0 & 0 & 0 \\ 0 & 0 & K_A & 0 & 0 & 0 \\ 0 & 0 & 0 & m_B & 0 & 0 \\ 0 & 0 & 0 & 0 & m_B & 0 \\ 0 & 0 & 0 & 0 & 0 & K_B \end{bmatrix} \qquad \dot{u} = \begin{Bmatrix} \dot{u}_1 \\ \dot{u}_2 \\ \dot{u}_3 \\ \dot{u}_4 \\ \dot{u}_5 \\ \dot{u}_6 \end{Bmatrix} \qquad f = \begin{Bmatrix} \sigma_1 \\ \sigma_2 \\ \sigma_3 \\ \sigma_4 \\ \sigma_5 \\ \sigma_6 \end{Bmatrix} \tag{71}$$

and then to express the dynamical equations of unconstrained motion represented by Eqs. (29), as

$$\begin{bmatrix} m_A & 0 & 0 & 0 & 0 & 0 \\ 0 & m_A & 0 & 0 & 0 & 0 \\ 0 & 0 & K_A & 0 & 0 & 0 \\ 0 & 0 & 0 & m_B & 0 & 0 \\ 0 & 0 & 0 & 0 & m_B & 0 \\ 0 & 0 & 0 & 0 & 0 & K_B \end{bmatrix} \begin{Bmatrix} \dot{u}_1 \\ \dot{u}_2 \\ \dot{u}_3 \\ \dot{u}_4 \\ \dot{u}_5 \\ \dot{u}_6 \end{Bmatrix} = \begin{Bmatrix} \sigma_1 \\ \sigma_2 \\ \sigma_3 \\ \sigma_4 \\ \sigma_5 \\ \sigma_6 \end{Bmatrix} \tag{72}$$

where K_A is the central principal moment of inertia of A for an axis parallel to $\hat{\mathbf{a}}_3$, and K_B is the central principal moment of inertia of B for an axis parallel to $\hat{\mathbf{b}}_3$.

We now regard body B as attached to body A with a slider joint that permits relative translation in the direction of $\hat{\mathbf{a}}_1$, but prevents relative translation in the direction of $\hat{\mathbf{a}}_2$, and prohibits relative rotation about $\hat{\mathbf{a}}_3 = \hat{\mathbf{b}}_3$. In this case, the constrained system possesses four degrees of freedom in an inertial reference frame. Points $\bar{A}$ and $\bar{B}$ are chosen as material points of A and B, respectively, that lie on the axis of the sliding joint as shown in Fig. 3. In the interest of simplicity they are chosen such that

$$\mathbf{r}^{A^*\bar{A}} = p_A\hat{\mathbf{a}}_2 \qquad \mathbf{r}^{B^*\bar{B}} = -p_B\hat{\mathbf{b}}_2 \tag{73}$$

where p_A and p_B are positive constants. It is worth keeping in mind that $\mathbf{r}^{B^*\bar{B}} = \mathbf{r}^{B^*\bar{A}}$ because $\bar{\bar{A}}$ is the point of A that is instantaneously coincident with $\bar{B}$.
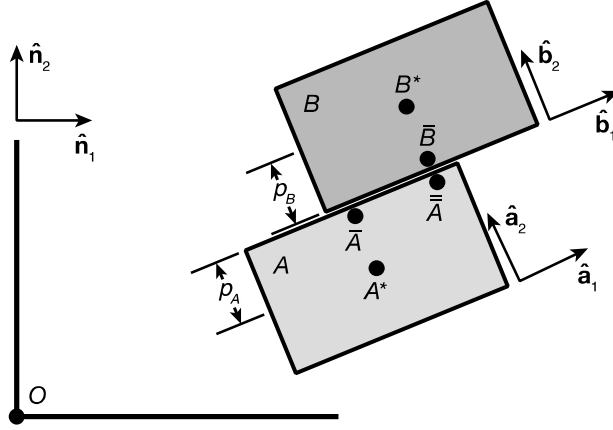

**Figure 3. Constrained planar motion of bodies
A and *B* in inertial reference system.**

A translational constraint equation is obtained by letting $\hat{\mathbf{a}}_2$ play the role of $\mathbf{e}_A$ in Eq. (6).

$$g_1 = g_1(t) = \left(\mathbf{r}^{O\bar{B}} - \mathbf{r}^{O\bar{A}}\right) \cdot \hat{\mathbf{a}}_2 = 0 \tag{74}$$

The position vectors from O to $\bar{A}$ and to $\bar{B}$ can be expressed as

$$\mathbf{r}^{O\bar{A}} = \mathbf{r}^{OA^*} + \mathbf{r}^{A^*\bar{A}} = q_1\hat{\mathbf{n}}_1 + q_2\hat{\mathbf{n}}_2 + p_A\hat{\mathbf{a}}_2 \tag{75}$$

$$\mathbf{r}^{O\bar{B}} = \mathbf{r}^{OB^*} + \mathbf{r}^{B^*\bar{B}} = q_4\hat{\mathbf{n}}_1 + q_5\hat{\mathbf{n}}_2 - p_B\hat{\mathbf{b}}_2 \tag{76}$$

Hence, Eq. (74) can be restated as

$$g_1 = (q_4 - q_1)(\hat{\mathbf{n}}_1 \cdot \hat{\mathbf{a}}_2) + (q_5 - q_2)(\hat{\mathbf{n}}_2 \cdot \hat{\mathbf{a}}_2) - p_A - p_B(\hat{\mathbf{b}}_2 \cdot \hat{\mathbf{a}}_2) = 0 \tag{77}$$

Table 1. Direction Cosine Matrices.

	$\hat{\mathbf{a}}_1$	$\hat{\mathbf{a}}_2$	$\hat{\mathbf{a}}_3$
$\hat{\mathbf{n}}_1$	$\cos q_3$	$-\sin q_3$	0
$\hat{\mathbf{n}}_2$	$\sin q_3$	$\cos q_3$	0
$\hat{\mathbf{n}}_3$	0	0	1

	$\hat{\mathbf{b}}_1$	$\hat{\mathbf{b}}_2$	$\hat{\mathbf{b}}_3$
$\hat{\mathbf{n}}_1$	$\cos q_6$	$-\sin q_6$	0
$\hat{\mathbf{n}}_2$	$\sin q_6$	$\cos q_6$	0
$\hat{\mathbf{n}}_3$	0	0	1

After referring to Table 1 to obtain the dot products

$$\hat{\mathbf{n}}_1 \cdot \hat{\mathbf{a}}_2 = -\sin q_3 \quad \hat{\mathbf{n}}_2 \cdot \hat{\mathbf{a}}_2 = \cos q_3 \quad \hat{\mathbf{b}}_2 \cdot \hat{\mathbf{a}}_2 = \cos(q_3 - q_6) \tag{78}$$

one can write

$$g_1 = -(q_4 - q_1)\sin q_3 + (q_5 - q_2)\cos q_3 - p_A - p_B \cos(q_3 - q_6) = 0 \tag{79}$$

The derivatives $\dot{g}_1$ and $\ddot{g}_1$ can be obtained either by differentiating Eq. (79) successively with respect to time, or by appealing to Eqs. (57) and (58), respectively. In either case, one obtains

$$\dot{g}_1 = [u_5 - u_2 - (q_4 - q_1)u_3]\cos q_3 - [u_4 - u_1 + (q_5 - q_2)u_3]\sin q_3$$
$$+ p_B(u_3 - u_6)\sin(q_3 - q_6) = 0 \tag{80}$$

and

$$\ddot{g}_1 = [\dot{u}_5 - \dot{u}_2 - 2(u_4 - u_1)u_3 - (q_4 - q_1)\dot{u}_3 - (q_5 - q_2)u_3{}^2]\cos q_3$$
$$- [\dot{u}_4 - \dot{u}_1 + 2(u_5 - u_2)u_3 + (q_5 - q_2)\dot{u}_3 - (q_4 - q_1)u_3{}^2]\sin q_3$$
$$+ p_B[(\dot{u}_3 - \dot{u}_6)\sin(q_3 - q_6) + (u_3 - u_6)^2\cos(q_3 - q_6)] = 0 \tag{81}$$

A rotational constraint equation is obtained from Eq. (7) by letting $\hat{\mathbf{b}}_2$ and $\hat{\mathbf{a}}_1$ play the parts of $\mathbf{e}_B$ and $\mathbf{e}_A$, respectively.

$$g_2 = g_2(t) = \hat{\mathbf{b}}_2 \cdot \hat{\mathbf{a}}_1 = \sin(q_3 - q_6) = 0 \tag{82}$$

The derivatives $\dot{g}_2$ and $\ddot{g}_2$ can be obtained by employing Eqs. (60) and (61) respectively. However, a significant amount of labor can be saved by simply differentiating Eq. (82) successively with respect to time to produce

$$\dot{g}_2 = (u_3 - u_6)\cos(q_3 - q_6) = 0 \tag{83}$$

and

$$\ddot{g}_2 = (\dot{u}_3 - \dot{u}_6)\cos(q_3 - q_6) - (u_3 - u_6)^2\sin(q_3 - q_6) = 0 \tag{84}$$

The reason for retaining $sin(q_3 \text{-} q_6)$ in Eq. (84) is that, due to constraint drift, Eq. (82) may not be satisfied identically. The error in $sin(q_3 - q_6)$ is controlled by the Baumgarte method, as indicated in Eqs. (52), (53), and (55). Inspection of Eqs. (81) and (84) for the coefficients of $\dot{u}_1, \ldots, \dot{u}_6$ allows one to identify the elements of the matrix α in Eqs. (54). For convenience, the transpose of α is recorded as

$$\alpha^T = \begin{bmatrix} \sin q_3 & 0 \\ -\cos q_3 & 0 \\ -(q_5 - q_2)\sin q_3 - (q_4 - q_1)\cos q_3 + p_B\sin(q_3 - q_6) & \cos(q_3 - q_6) \\ -\sin q_3 & 0 \\ \cos q_3 & 0 \\ -p_B\sin(q_3 - q_6) & -\cos(q_3 - q_6) \end{bmatrix} \tag{85}$$

The 2×1 matrix γ' in Eqs. (55) is constructed with the terms in Eqs. (81) and (84) that do not involve $\dot{u}_1, \ldots, \dot{u}_6$ and with Eqs. (79), (80), (82), and (83).

$$\gamma_1' = -2u_3[(u_4 - u_1)\cos q_3 + (u_5 - u_2)\sin q_3]$$

$$+ u_3{}^2[(q_4 - q_1)\sin q_3 - (q_5 - q_2)\cos q_3] + p_B(u_3 - u_6)^2\cos(q_3 - q_6)$$

$$+ 2\eta\{[u_5 - u_2 - (q_4 - q_1)u_3]\cos q_3 - [u_4 - u_1 + (q_5 - q_2)u_3]\sin q_3 + p_B(u_3 - u_6)\sin(q_3 - q_6)\}$$

$$+ \eta^2[(q_5 - q_2)\cos q_3 - (q_4 - q_1)\sin q_3 - p_A - p_B\cos(q_3 - q_6)] \tag{86}$$

$$\gamma_2' = -(u_3 - u_6)^2\sin(q_3 - q_6) + 2\eta(u_3 - u_6)\cos(q_3 - q_6) + \eta^2\sin(q_3 - q_6) \tag{87}$$

In this example, two independent equations (74) and (82) describe the constraint imposed by the slider joint. Hence, precisely two unknown multipliers $\lambda_1(t)$ and $\lambda_2(t)$ are all that are necessary to characterize the set of internal forces associated with the joint. The two multipliers in the matrix λ are determined at any instant of time by using Eqs. (34) and the matrices M, f, α, and γ'. Subsequently, the generalized constraint forces are formed as

$$\alpha^T\lambda = \begin{Bmatrix} \sin q_3\,\lambda_1 \\ -\cos q_3\,\lambda_1 \\ [-(q_5 - q_2)\sin q_3 - (q_4 - q_1)\cos q_3 + p_B\sin(q_3 - q_6)]\lambda_1 + \cos(q_3 - q_6)\lambda_2 \\ -\sin q_3\,\lambda_1 \\ \cos q_3\,\lambda_1 \\ -p_B\sin(q_3 - q_6)\lambda_1 - \cos(q_3 - q_6)\lambda_2 \end{Bmatrix} \tag{88}$$

These generalized constraint forces are added to the right-hand member of Eqs. (72), as required by Eqs. (30), to form dynamical equations governing constrained motion of A and B. The dynamical equations, together with the kinematical differential equations (64) and initial values of q_r and u_r, can be integrated numerically to obtain time histories of the generalized coordinates q_r and motion variables u_r $(r = 1, \ldots, 6)$. The accuracy of the numerical solution can be measured by the extent to which the translational and rotational constraints are unsatisfied; that is, by how much $g_1(t)$ and $g_2(t)$ differ from zero.

The rotational constraint equation (82) is satisfied when $q_6 = q_3$; as long as the constraint is satisfied, $\sin(q_3 - q_6)$ can be replaced with 0, and $\cos(q_3 - q_6)$ can be replaced with 1 in Eqs. (88).

As discussed in Refs: 21, 28 and 29, the constraint force $\mathbf{F}^{(\text{CON})}$ applied to B at $\overline{B}$ can be determined by inspecting Eq. (10) and is given by

$$\mathbf{F}^{(\text{CON})} = \lambda_1\mathbf{e}_A = \lambda_1\hat{\mathbf{a}}_2 \tag{89}$$

Similarly, the constraint torque $\mathbf{T}^{(\text{CON})}$ applied to B is identified by inspecting Eq. (21),

$$\mathbf{T}^{(\text{CON})} = \lambda_2(\mathbf{e}_B \times \mathbf{e}_A) = \lambda_2(\mathbf{b}_2 \times \mathbf{a}_1) = -\lambda_2\mathbf{b}_3 \tag{90}$$

These vector quantities can be used in Eqs. (1)–(5).

Section 3. Test Cases

3.1 CFE Test Cases

A series of test cases was selected to validate the CFE methodology as listed in table 2. These cases include simulation models involving two rigid bodies connected by various types of simple joints. For test case 1, the geometrical shape of the two rigid bodies is defined as discussed below. However, for test cases 2–6, the geometrical shape is arbitrary and only schematic representations are shown for convenience. It is possible that depending on the geometrical shape selected for the two bodies having the same mass properties and subject to the same external force/moment as selected here, the two bodies may collide during the selected duration of simulation. Since the focus of this report is on the estimation of joint constraint loads and how they compare with ADAMS® for test/validation of CFE methodology, collision between two bodies, if any, are ignored.

Table 2. CFE Test Cases.

Case #	Name of the Joint	Description
1	Fixed	Two boxes fixed to each other
2	Spherical	Two boxes connected by a spherical joint
3	Revolute	Two boxes connected by a revolute joint
4	Translational	A box sliding along a fixed rail that is rectangular in cross section
5	Cylindrical	A box sliding along a fixed rod that is circular in cross section
6	Universal	Two boxes connected by a universal joint
7	Planar	A thin disk sliding along a table top

3.1.1 Test Case 1: Fixed Joint

This test case involves two rectangular rigid bodies, denoted as bodies A and B with dimensions as shown, connected by a fixed joint (fig. 4). The fixed joint is a mathematical concept but serves as a rigorous test case for the CFE methodology because one knows that the joint displacement (linear and angular) must be insignificantly small (ideally zero) when the two bodies are rigidly connected, and there is no relative motion. The mass centers A^*, B^* and S^* are respectively the centroids of body A, body B and the combined body (prior to release).
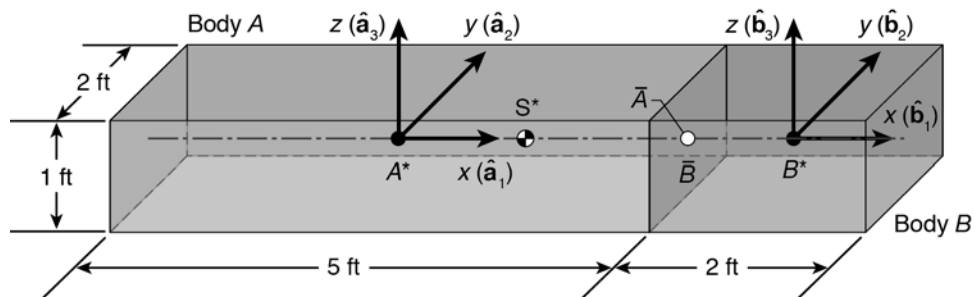

Figure 4.   Test Case 1, two rigid bodies, *A* and *B*, connected by a fixed joint.

Table 3. Mass Properties for Test Case 1.

	Body A	Body B
m	1 slug	4/10 slug
I_{xx}	5/12 slug-ft²	1/6 slug-ft²
I_{yy}	26/12 slug-ft²	1/6 slug-ft²
I_{zz}	29/12 slug-ft²	4/15 slug-ft²

Table 3 shows the mass properties for each body. The fixed joint constrains the point $\bar{A}$ fixed in A to remain coincident with the point $\bar{B}$ fixed in B. The three translational constraint equations have the form of Eq. (7) and can be written as

$$\left(\mathbf{r}^{O\bar{B}} - \mathbf{r}^{O\bar{A}}\right) \cdot \hat{\mathbf{e}}_A = 0 \tag{91}$$

where the role of $\mathbf{e}_A$ in Eq. (7) is played in turn by $\hat{\mathbf{a}}_1$, $\hat{\mathbf{a}}_2$, and $\hat{\mathbf{a}}_3$, members of a set of three right-handed, mutually orthogonal unit vectors fixed in A at its mass center A^* as shown in fig. 4. Let $\hat{\mathbf{b}}_1$, $\hat{\mathbf{b}}_2$, and $\hat{\mathbf{b}}_3$ be a similar set of unit vectors fixed in B at its mass center B^* such that $\hat{\mathbf{b}}_r$ points in the same direction as $\hat{\mathbf{a}}_r$ ($r = 1, 2, 3$) when A and B are attached to each other. The fixed joint constrains unit vectors fixed in A to remain perpendicular to certain unit vectors fixed in B resulting in the following three constraint equations in the form of Eq. (8):

$$\hat{\mathbf{b}}_2 \cdot \hat{\mathbf{a}}_1 = 0 \tag{92}$$

$$\hat{\mathbf{b}}_3 \cdot \hat{\mathbf{a}}_1 = 0 \tag{93}$$

$$\hat{\mathbf{b}}_2 \cdot \hat{\mathbf{a}}_3 = 0 \tag{94}$$

Thus, all six constraint equations (91)–(94) characterize the fixed joint, which is the maximum number of constraint equations that can be specified for a joint. These constraint equations need to be differentiated twice to construct the matrix $\alpha^T \lambda$ that contains the generalized constraint forces as illustrated earlier for the sliding joint.

3.1.1.1   Numerical Simulation

The bodies A and B are assumed to be rigidly connected to each other for first 10 sec and then "released" instantaneously. Throughout the duration of this simulation, all external forces or moments including gravity were assumed equal to zero. Because there are no external forces or moments, integrals involving linear and angular momentum must remain constant. Since the linear momentum of the combined body prior to separation is zero, after separation, the mass centers of A and B must travel in straight lines with constant velocities such that the net linear momentum is zero and the system mass center remains at rest.

This problem was set up such that the inertial reference frame coincides with the combined body frame at $t = 10$ sec just prior to the joint release, the linear velocity of the combined body is zero, and the angular velocity components of the combined body were selected as (0, 2.0, 0.5) rad/sec or (0, 114.5454, 28.6363) deg/sec. Then, working backwards, the initial ($t = 0$) angular velocity, $\omega = 63.02\hat{\mathbf{n}}_1 - 82.32\hat{\mathbf{n}}_2 + 80.25\hat{\mathbf{n}}_3$ deg/sec in the body frame was deduced. With these

derived initial conditions, the simulation can be done as usual with forward integration in time releasing the joint at 10 sec and terminating the simulation at 20 sec.

To verify and validate POST2/CFE simulation results, a simulation was also created with AUTOLEV (ref. 22) an interactive program designed specifically for the kinematic and dynamic analysis of mechanical systems. For this test case, AUTOLEV was used to create a computer program to simulate the motions of A and B and determine the constraint forces required to hold them together for the first 10 seconds. The AUTOLEV results were generated using a variable step integrator with an absolute error limit of 1×10^{-8} and a relative error limit of 1×10^{-7}. The POST2/CFE method employed a fixed step integrator with a step size of 0.0001 sec. The CFE routine also used a Baumgarte (ref. 27) constraint stabilization factor $\eta = 5.0$.

Time histories for the inertial x, y, and z components of linear velocity of the mass centers of body A and B are shown for 20 sec in Figs. 5 and 6. Prior to release, even though the combined body has zero linear velocity, bodies A and B have nonzero linear velocity components because their mass centers A^* and B^* are offset from the combined mass center S^*. However, the combined sum of each of the three components of linear momentum should be zero. This fact can be checked using mass properties from table 2 and velocity component data presented in fig. 5 and 6. The magnitudes of each of the three linear velocity components for body A and B oscillate during the first 10 sec because their body axes angular velocity components vary as shown in fig. 7 and 8. After release, the linear velocity components for each body remain constant because each body is now spinning about its own mass center. Note that x component of linear velocity for both body A and B is zero at $t = 10$ sec because the inertial frame was set to coincide with body frame at this point and the center of gravities of both body A and B are located along X axis.
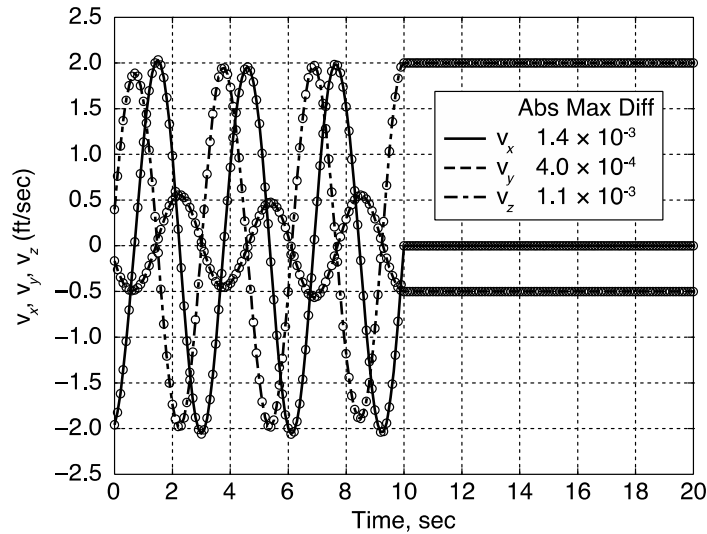
Figure 5. Test Case 1, Body *A*: Inertial velocity components of mass center. POST2/CFE as circles, AUTOLEV as lines.
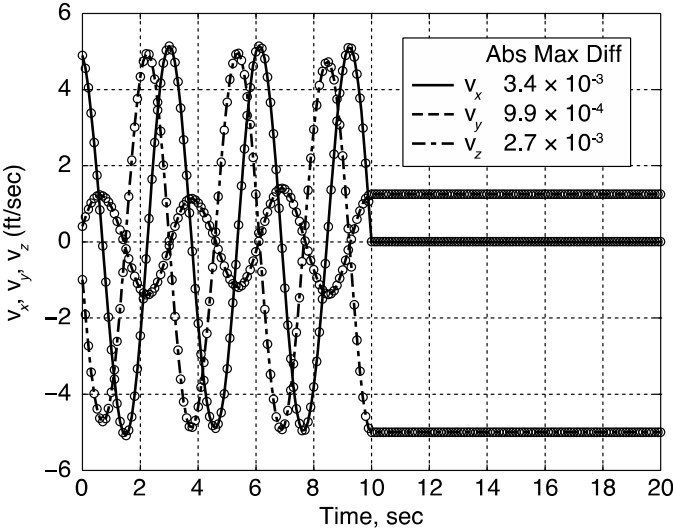
**Figure 6.   Test Case 1, Body *B*: Inertial velocity components of mass center.**
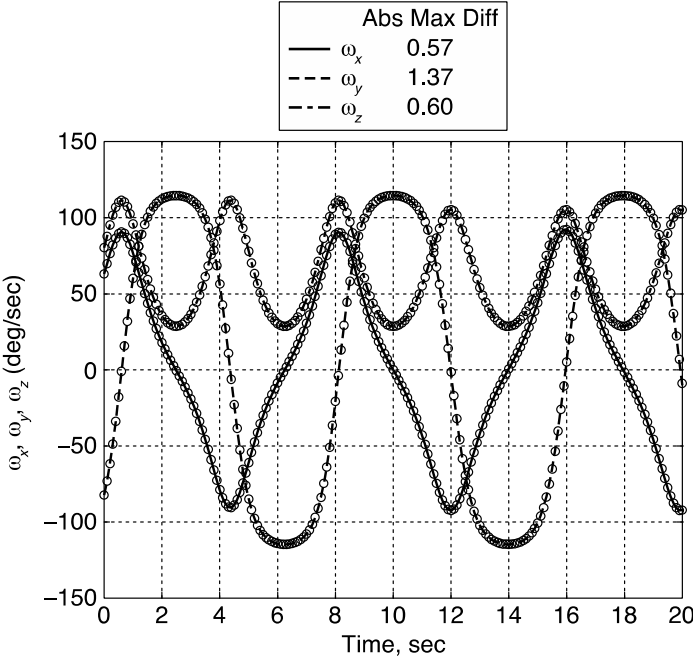
Figure 7.   Test Case 1, Body *A*: Body axes angular velocity components. POST2/CFE as circles, AUTOLEV as lines.
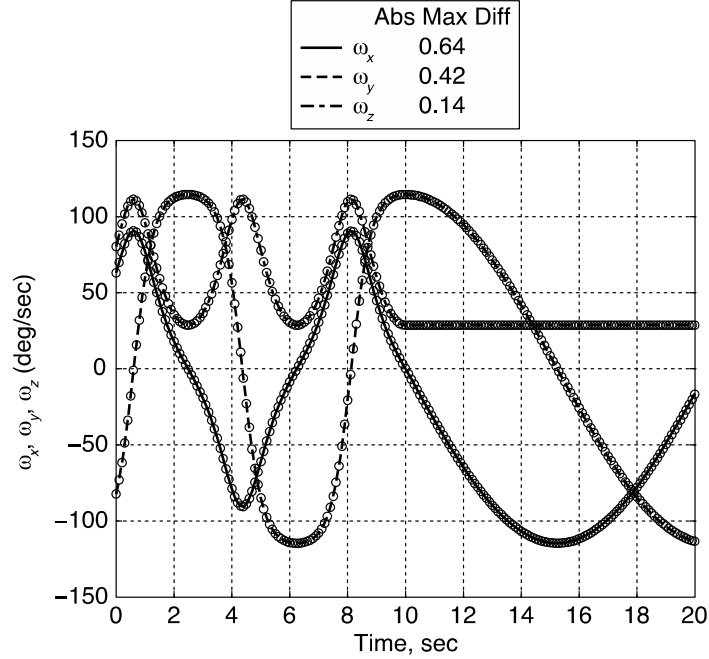
**Figure 8. Test Case 1, Body *B*: Body axes angular velocity
components. POST2/CFE as circles, AUTOLEV as lines.**

For $t = 0$ to 10 sec, when the bodies are connected, the angular velocity of each body is equal to that of the combined body. After release, the angular velocities vary such that total angular momentum of body A and B remains constant and equal to that of the combined body. The change in the angular velocity components of body B are more noticeable than those for body A because B is smaller in size compared to body A. Further, for body B, the moments of inertia about x and y body axes were selected to be equal so that

$$I_{zz}\dot{\omega}_z = (I_{xx} - I_{yy})\omega_x\omega_x = 0 \tag{95}$$

As a result, ω_z remains constant after release.

Figures 9 and 10 show the main results of the CFE method, which are the constraint forces and torques (moments). As said previously, these constraint forces/torques are applied as additional external loads for each body A and B within POST2. The results of this exercise show that the constraint forces/torques determined by CFE agree well with the AUTOLEV results.

The relative joint displacement between the two bodies when they are supposed to stay connected is a basic metric to assess the accuracy of the POST2/CFE methodology. This parameter is computed as the position vector from $\bar{A}$ to $\bar{B}$ and should be ideally zero while the joint constraint is imposed for the first 10 sec. Hence, any deviation from zero is a measure of accuracy of the CFE algorithm. In the CFE algorithm the constraints are expressed at the acceleration level. However, as with all algorithms of this type, the constraints at the velocity and position levels are subject to numerical integration errors. Such errors depend on the step size in a fixed-step integration scheme or the error limits in a variable-step approach. Baumgarte stabilization (ref. 27) helps to control these errors from growing arbitrarily large during a simulation.

The choice of step size and Baumgarte factor (η) for this problem was a reasonable balance between CPU time and error buildup. Figure 11 shows the joint translational displacement as a func-

tion of time for the 10 sec period when the bodies are supposed to stay connected. The quantities Δx, Δy and Δz are the x, y and z components of joint translational displacement in the local body frame and are defined as follows:

$$\Delta x = \left(\mathbf{r}^{O\bar{A}} - \mathbf{r}^{O\bar{B}}\right) \cdot \hat{\mathbf{a}}_1, \; \Delta y = \left(\mathbf{r}^{O\bar{A}} - \mathbf{r}^{O\bar{B}}\right) \cdot \hat{\mathbf{a}}_2, \; \Delta z = \left(\mathbf{r}^{O\bar{A}} - \mathbf{r}^{O\bar{B}}\right) \cdot \hat{\mathbf{a}}_3 \tag{96}$$

In the interest of clarity, only the POST2/CFE results are shown. The magnitude of this displacement distance is below 0.01 percent of the combined body length.
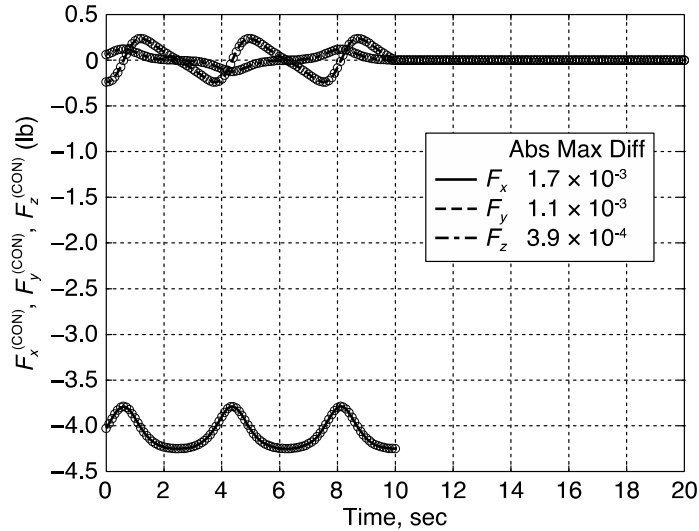
Figure 9. Test Case 1: Comparison of constraint forces required to hold bodies together. Joint release occurs at t = 10 sec. POST2/CFE as circles, AUTOLEV as lines.
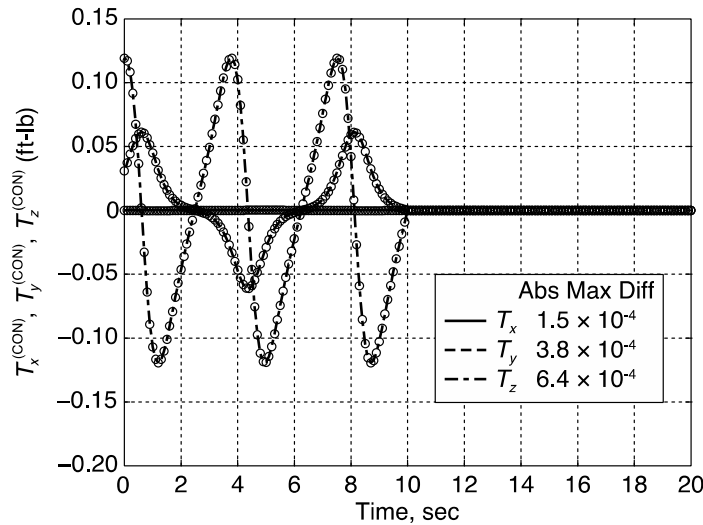
Figure 10. Test Case 1: Comparison of constraint torques. POST2/CFE as circles, AUTOLEV as lines.
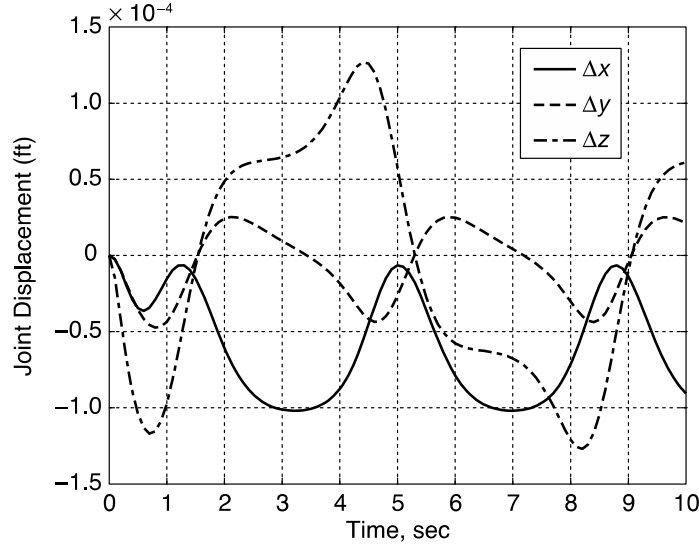
**Figure 11. Test Case 1: Joint displacement
in *x*, *y*, and *z* directions.**

3.1.2 **Test Case 2: *Spherical* Joint**

This test case consists of two boxes connected by a spherical joint as shown in fig. 12. A spherical, or ball-in-socket, joint connects two bodies such that they can rotate arbitrarily about any of the three axes at the joint, but cannot have any relative translation at the joint. The reference inertial axes system is located at the joint and is lined up with body axes systems of both Box 1 and Box 2 at $t = 0$. Table 4 presents the mass properties and the center of mass locations.

The spherical joint constrains all three translational DOF between the two boxes but allows arbitrary rotation at the joint. The following equations define this constraint:

$$\left(\mathbf{r}^{O\bar{B}} - \mathbf{r}^{O\bar{A}}\right) \cdot \hat{\mathbf{a}}_1 = 0 \tag{97}$$

$$\left(\mathbf{r}^{O\bar{B}} - \mathbf{r}^{O\bar{A}}\right) \cdot \hat{\mathbf{a}}_2 = 0 \tag{98}$$

$$\left(\mathbf{r}^{O\bar{B}} - \mathbf{r}^{O\bar{A}}\right) \cdot \hat{\mathbf{a}}_3 = 0 \tag{99}$$

where $\mathbf{r}^{O\bar{A}}$ and $\mathbf{r}^{O\bar{B}}$ are the vectors to joint locations from mass centers of Box 1 and Box 2, $\hat{\mathbf{a}}_1$, $\hat{\mathbf{a}}_2$ and $\hat{\mathbf{a}}_3$ are the unit vectors along x, y and z axes of Box 1. Similarly, $\hat{\mathbf{b}}_1$, $\hat{\mathbf{b}}_2$ and $\hat{\mathbf{b}}_3$ are the unit vectors of Box 2. This problem is setup such that the inertial frame is located at the joint and coincides with the body frame(s) at $t = 0$.

A constant external force with body axes components $5000 * (5,5,1)/\sqrt{51}$ lb was applied to Box 1 at (–2.0, 0, 0.5) ft in Box 1 body axes system. Figures 13–19 show ADAMS® and POST2/CFE simulation results for 10 seconds when the bodies stay connected. Note that for this test case, the spherical joint was not released at all. ADAMS® used its built-in Runge-Kutta-Fehlberg 45 (RKF45) single step integrator with adaptive step size and an error tolerance of 1.0x10^{-11}. POST2 used the single step fourth order Runge-Kutta method with a fixed step size of 0.001s. The other integration options available in POST 2 were also tried but did not show any significant impact on the numerical results. The differences were very small and negligible. Hence, for all the test cases

presented in this report, the fixed step Runge-Kutta integration method was used. The absolute values of maximum differences between POST2 CFE and ADAMS® predictions are small and negligible as indicated in fig. 14. The CFE Baumgarte factor was set to 10.0 to reduce joint constraint errors. The Euler angles presented in fig. 15 represent the orientation of Box 1 and Box 2 with respect to inertial reference frame.
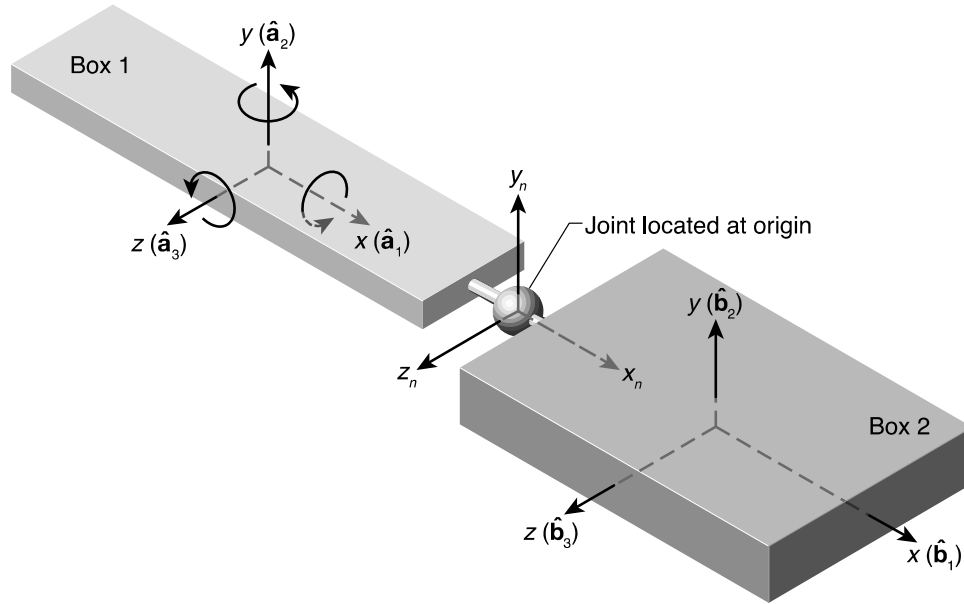

Figure 12.   Test Case 2: Spherical.

Table 4. Mass Properties for Test Case 2.

	Box 1	Box 2
m	622 slugs	622 slugs
I_{xx}	220.2916667 slug ft^2	881.166667 slug ft^2
I_{yy}	3524.666667 slug ft^2	2695.33333 slug ft^2
I_{zz}	3330.291667 slug ft^2	1917.83333 slug ft^2
Center of mass location in inertial system at $t = 0$	{−4.854, −0.096, 0} ft	{3.851, −0.096, 0} ft

(a) Box 1.

(b) Box 2.

Figure 13. Comparison of mass center inertial displacements between ADAMS® and POST2/CFE for the spherical joint.
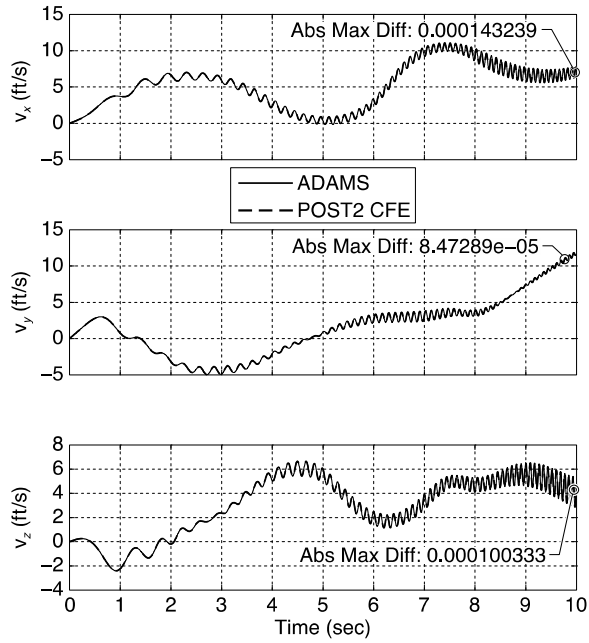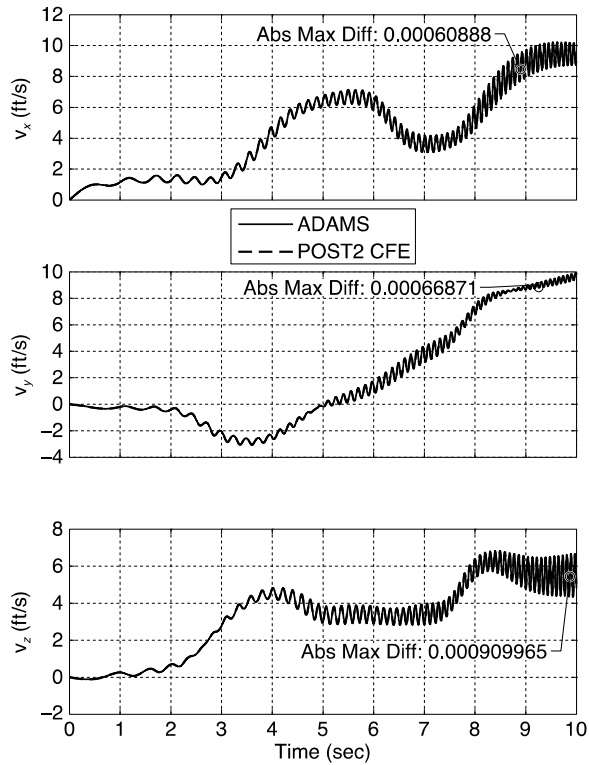
(a) Box 1.

(b) Box 2.

Figure 14. Inertial velocity component comparison between ADAMS® and POST2/CFE for the spherical joint.
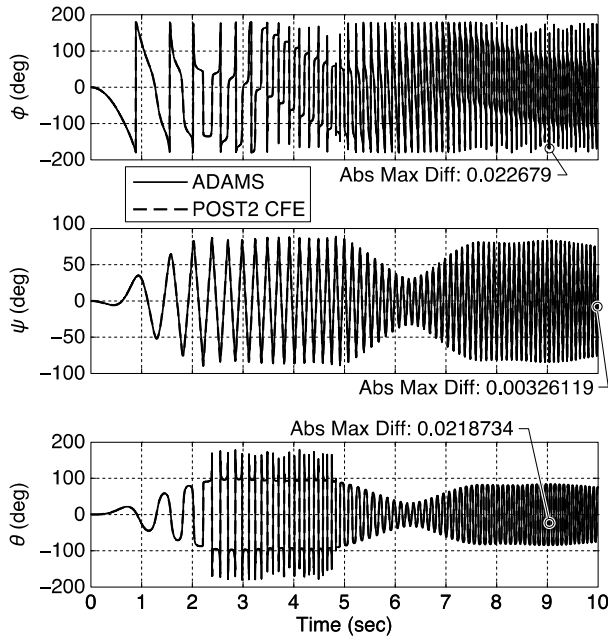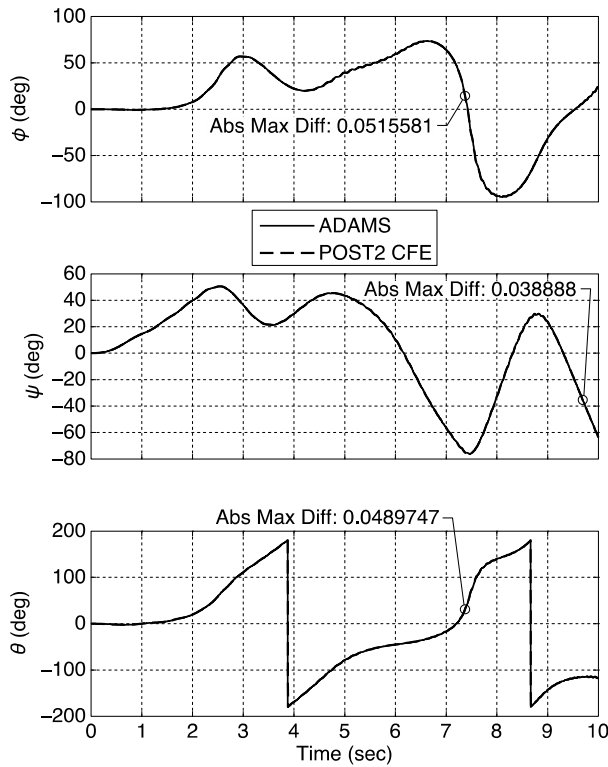
(a) Box 1.

(b) Box 2.

Figure 15.   Test Case 2: Euler angle (1-3-2 sequence) comparison between ADAMS® and POST2/CFE for the spherical joint.
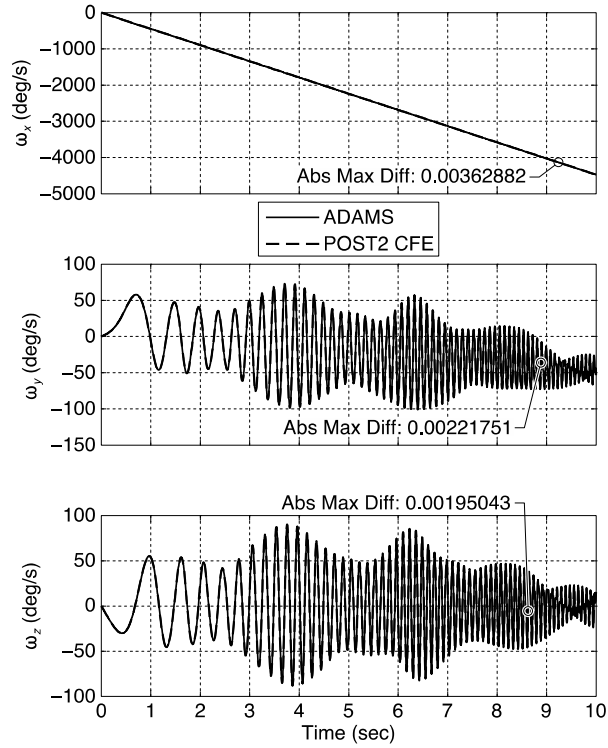
(a) Box 1.
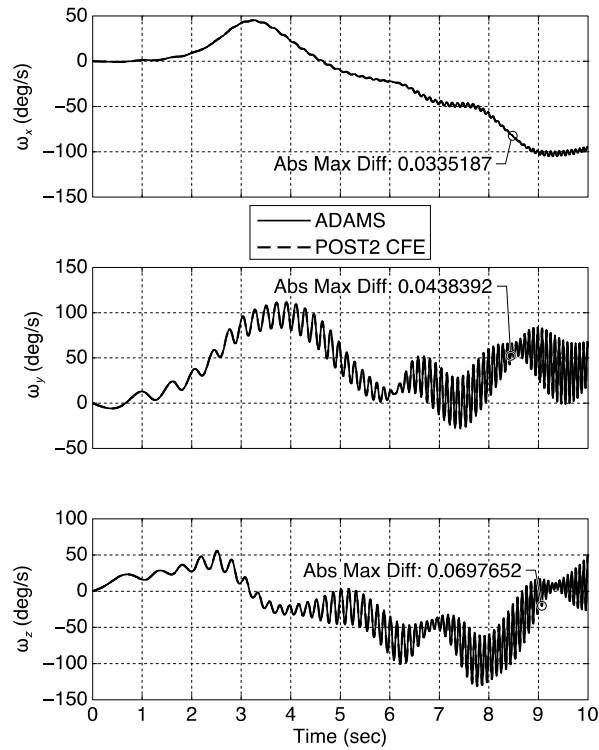
(b) Box 2.

Figure 16.   Body frame angular velocity comparison between
ADAMS[®] and POST2/CFE for the spherical joint.
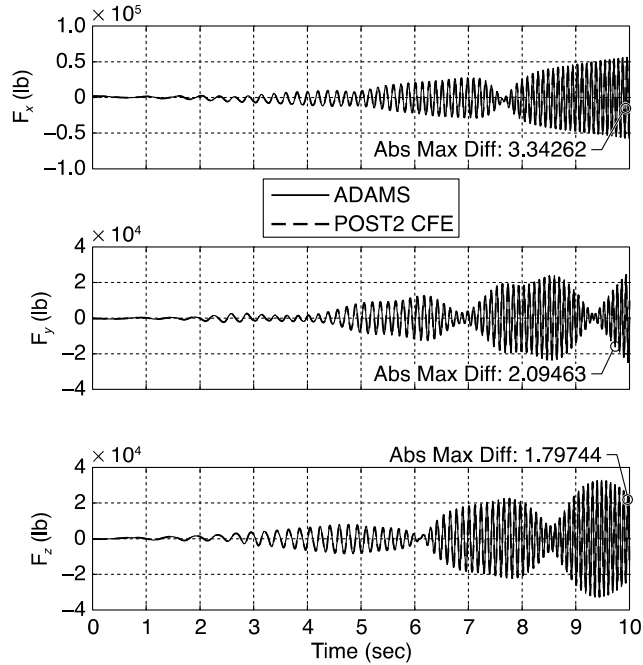
Figure 17. Test Case 2: Box 2 body frame constraint force (at the joint) comparison between ADAMS® and POST2/CFE for the spherical joint.
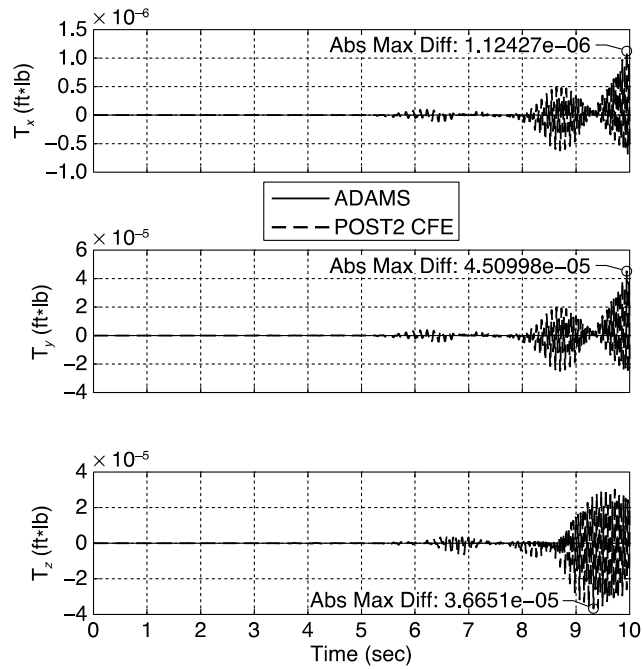
Figure 18. Box 2 body frame constraint torque (at the joint) comparison between ADAMS® and POST2/CFE for the spherical joint.
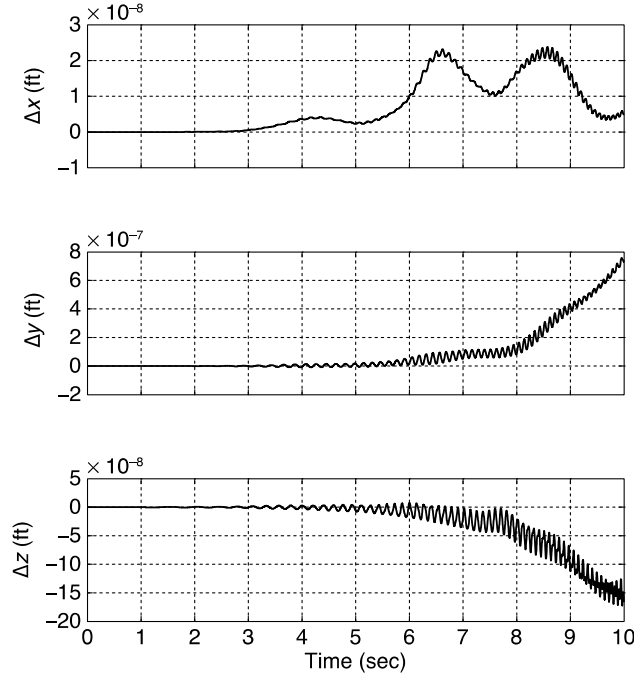
**Figure 19. Relative joint separation between the connection points
of Box 1 and 2, represented in the body frame of Box 1.**

3.1.3   Test Case 3: Revolute Joint

This test case consists of two boxes connected by a revolute joint (fig. 20). A revolute, or pin, joint acts like a hinge on a door that prevents the door from separating from the wall but allows it to rotate only about a single hinge axis. The reference inertial axes system is located at the joint and is lined up with body axes systems of both Box 1 and Box 2 at $t = 0$. Table 5 presents the mass properties and the center of mass locations.

The revolute joint constrains all three translational and two rotational DOF between the two boxes allowing only relative rotations about the z body axis of Box 1. The following equations define this constraint:

$$\left(\mathbf{r}^{O\bar{B}} - \mathbf{r}^{O\bar{A}}\right) \cdot \hat{\mathbf{a}}_1 = 0 \tag{100}$$

$$\left(\mathbf{r}^{O\bar{B}} - \mathbf{r}^{O\bar{A}}\right) \cdot \hat{\mathbf{a}}_2 = 0 \tag{101}$$

$$\left(\mathbf{r}^{O\bar{B}} - \mathbf{r}^{O\bar{A}}\right) \cdot \hat{\mathbf{a}}_2 = 0 \tag{102}$$

$$\hat{\mathbf{b}}_3 \cdot \hat{\mathbf{a}}_1 = 0 \tag{103}$$

$$\hat{\mathbf{b}}_3 \cdot \hat{\mathbf{a}}_2 = 0 \tag{104}$$

A constant external force with body axes components $5000 * (5, 5, 1)/\sqrt{51}$ lb was applied to Box 1 at (–2.0, 0, 0.5 ft) in Box 1 body axes system. Figures 20–27 show the comparison of ADAMS® and POST2/CFE simulation results. ADAMS® used its built-in RKF45 single step integrator with

adaptive step size using an error tolerance of 5.0×10^{-11}. POST2 used the single step fourth order Runge Kutta method with a fixed step size of 0.001s. The CFE Baumgarte factor was set to 10.0 to reduce joint constraint errors. Simulation results are presented in figs 21–28. The relative joint errors (fig. 28) are, $\Delta\phi = 90 - \mathrm{acos}\,(\hat{\mathbf{b}}_3 \cdot \hat{\mathbf{a}}_1)$, and, $\Delta\theta = 90 - \mathrm{acos}\,(\hat{\mathbf{b}}_3 \cdot \hat{\mathbf{a}}_2)$ respectively. It is observed that POST2/CFE results compare well with those generated using ADAMS®.
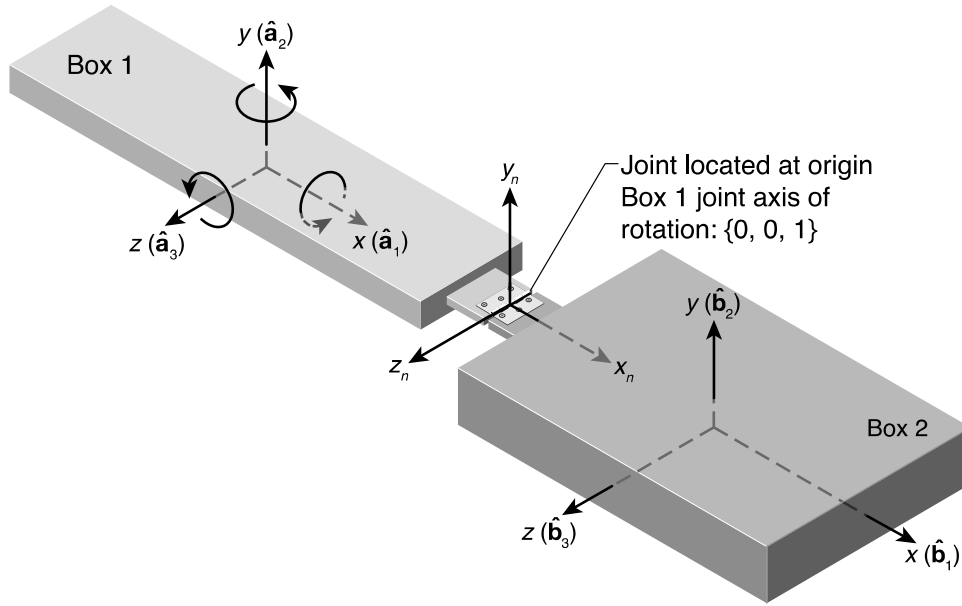
Figure 20. Test Case 3: Revolute joint.

Table 5. Properties for Test Case 3.

	Box 1	**Box 2**
m	622 slugs	622 slugs
I_{xx}	220.2916667 slug ft^2	881.166667 slug ft^2
I_{yy}	3524.666667 slug ft^2	2695.33333 slug ft^2
I_{zz}	3330.291667 slug ft^2	1917.83333 slug ft^2
Center of mass location in inertial system at $t = 0$	{−4.854, −0.096, 0} ft	{3.851, −0.096, 0} ft

(a) Box 1.

(b) Box 2.

Figure 21. Inertial position comparison between ADAMS® and POST2/CFE for the revolute joint.
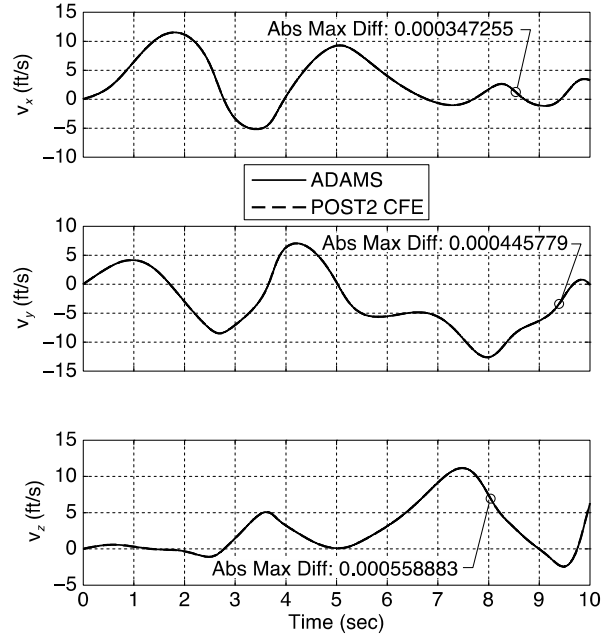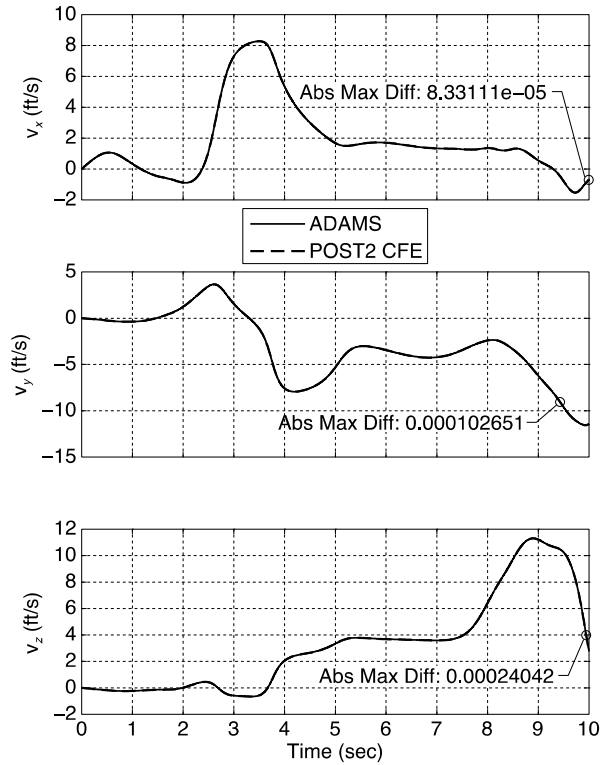
(a) Box 1.

(b) Box 2.

Figure 22. Inertial velocity comparison between ADAMS® and POST2/CFE for the revolute joint.
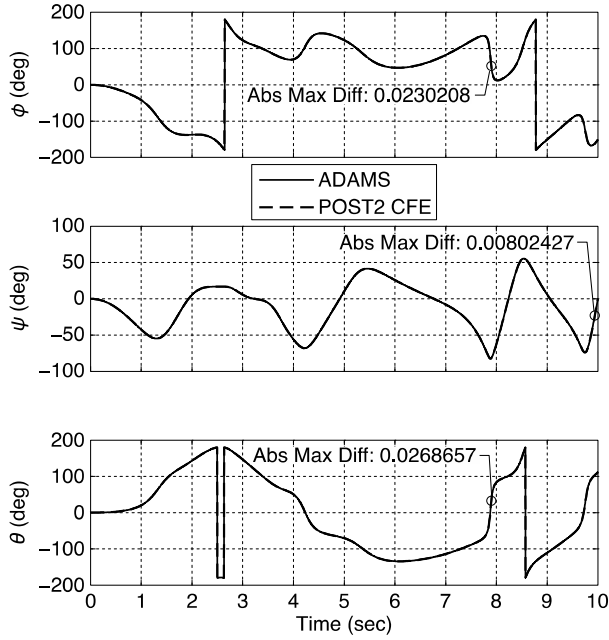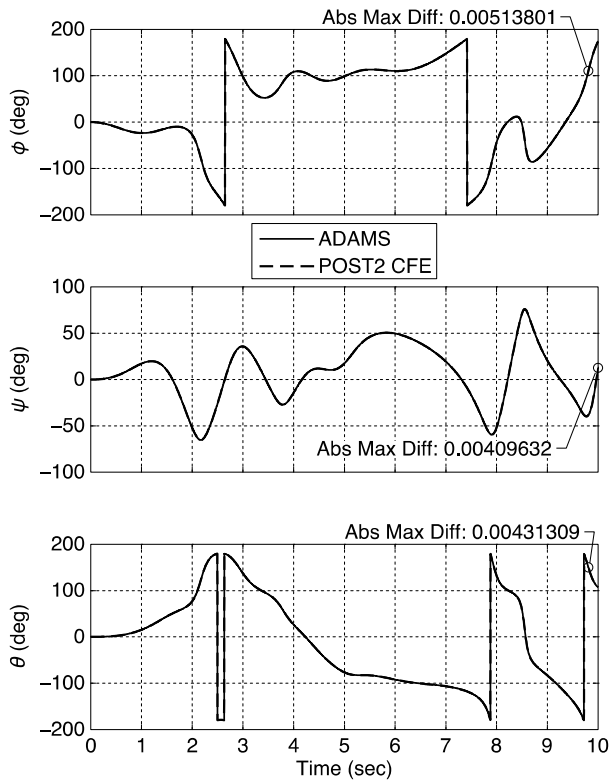
(a) Box 1.

(b) Box 2.

Figure 23.   Box 1 Euler angle (1-3-2 sequence) comparison between ADAMS® and POST2/CFE.
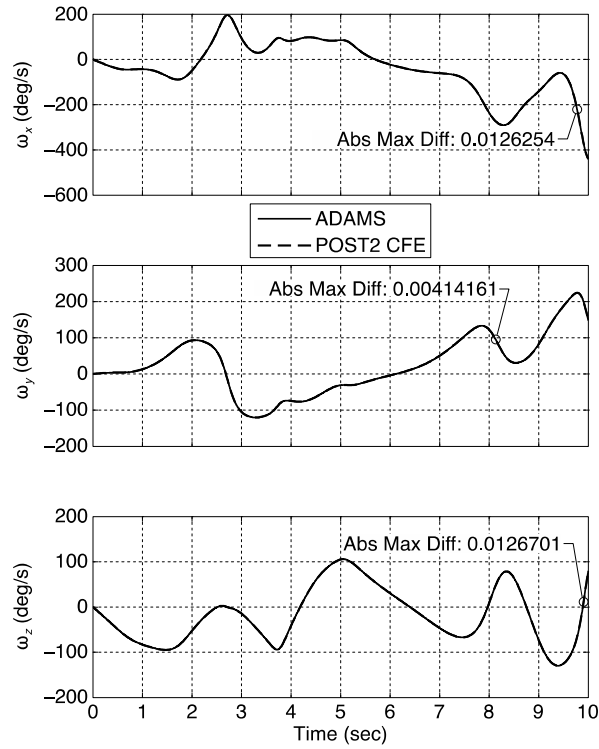
(a) Box 1.
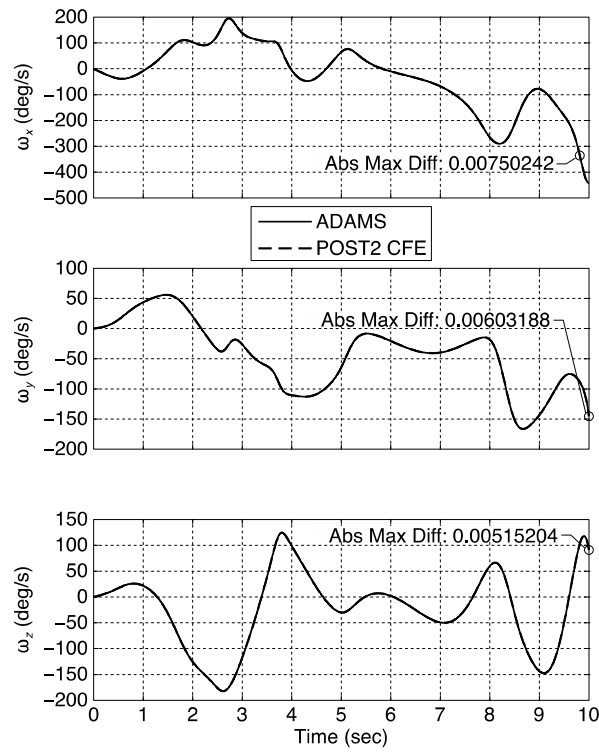
(b) Box 2.

Figure 24.   Inertial angular velocity comparison between ADAMS® and POST2/CFE for the revolute joint.
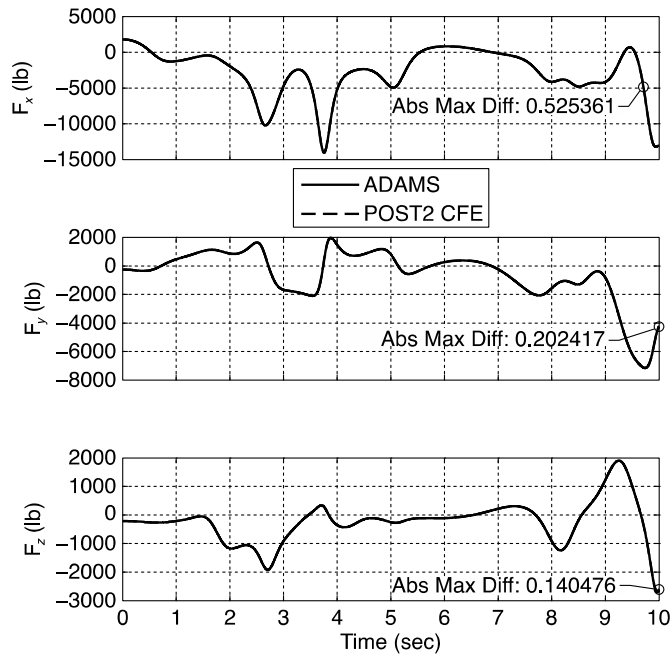
**Figure 25.   Box 1 body frame constraint force
(at the joint) comparison between ADAMS® and
POST2/CFE for the revolute joint.**
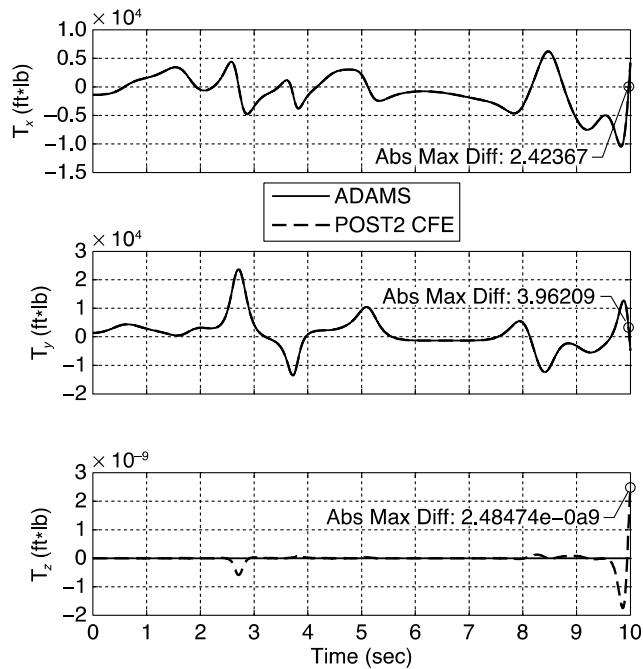
**Figure 26.   Box 2 body frame constraint torque
(at the joint) comparison between ADAMS® and
POST2/CFE for the revolute joint.**
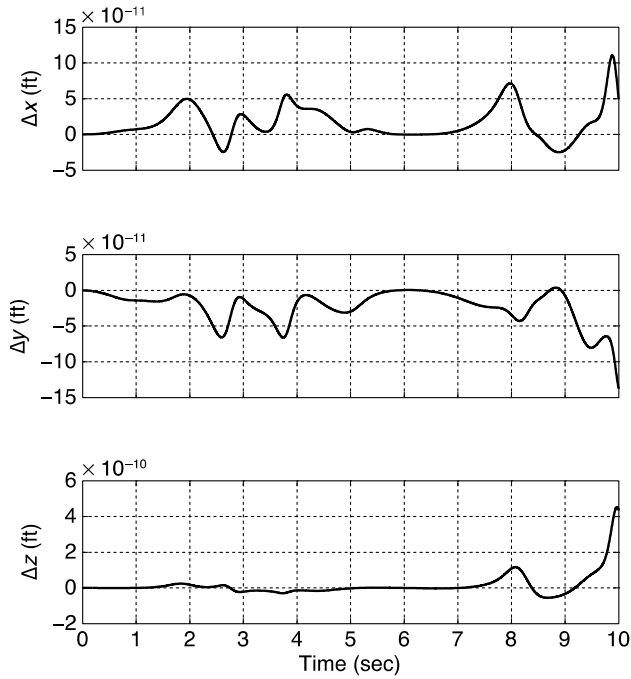
**Figure 27. Relative joint separation between
Box 1 and 2 for the revolute joint.**
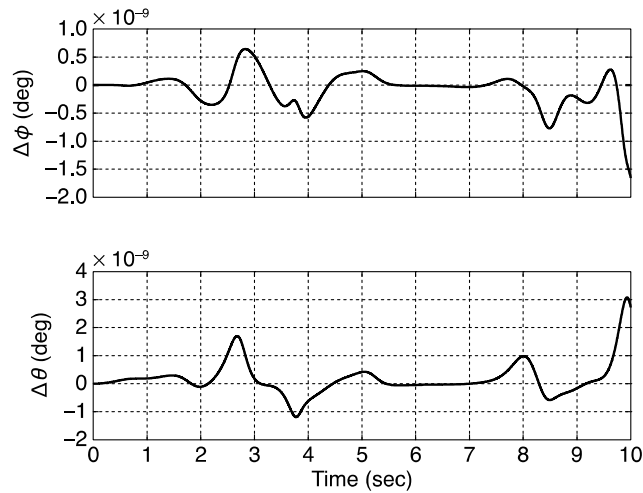
**Figure 28. Relative joint orientation error between
Box 1 and 2 for the revolute joint.**

3.1.4   Test Case 4: Translational Joint

This test case consists of a brick constrained to slide along a rail using a translational joint (fig. 29). A translational, or a onedimensional slider, joint can be thought of as an object sliding along a straight rail that has a rectangular cross section. The rectangular cross section prevents the object from rotating in any direction relative to the rail, while permitting relative sliding along the rail.

The reference inertial axes system is located at the joint and is lined up with body axes systems of both Box 1 and Box 2 at t = 0. Table 6 presents the mass properties and the center of mass locations.

The translational joint constrains all three rotational and two translational DOF between the two bodies allowing only relative translations along the z-axis of the rail. The following equations define this constraint:

$$\left(\mathbf{r}^{O\bar{B}} - \mathbf{r}^{O\bar{A}}\right) \cdot \hat{\mathbf{a}}_1 = 0 \tag{105}$$

$$\left(\mathbf{r}^{O\bar{B}} - \mathbf{r}^{O\bar{A}}\right) \cdot \hat{\mathbf{a}}_2 = 0 \tag{106}$$

$$\hat{\mathbf{b}}_3 \cdot \hat{\mathbf{a}}_1 = 0 \tag{107}$$

$$\hat{\mathbf{b}}_3 \cdot \hat{\mathbf{a}}_2 = 0 \tag{108}$$

$$\hat{\mathbf{b}}_1 \cdot \hat{\mathbf{a}}_2 = 0 \tag{109}$$

A constant external force with body axes component (5000, 40000, −746) lb was applied to the brick at (−0.6, 0, −1.33334) ft in body axes system. The brick translates along the rail, which is fixed inertially. The centerline of the rail, which is also the z-axis of the rail, coincides with the z inertial axis. Figures 30–37 show the comparison between ADAMS® and POST2/CFE results. The relative joint errors (fig. 37) are, $\Delta\phi = 90 - \mathrm{acos}(\hat{\mathbf{b}}_3 \cdot \hat{\mathbf{a}}_1)$, $\Delta\theta = 90 - \mathrm{acos}(\hat{\mathbf{b}}_3 \cdot \hat{\mathbf{a}}_2)$, and $\Delta\psi = 90 - \mathrm{acos}(\hat{\mathbf{b}}_1 \cdot \hat{\mathbf{a}}_2)$ respectively. ADAMS® used its built-in RKF45 single step integrator with adaptive step size and an error tolerance of 1.0e–11. POST2 used the single step fourth order Runge Kutta method with a fixed step size of 0.001s. The CFE Baumgarte factor was set to 10.0 to reduce joint constraint errors.
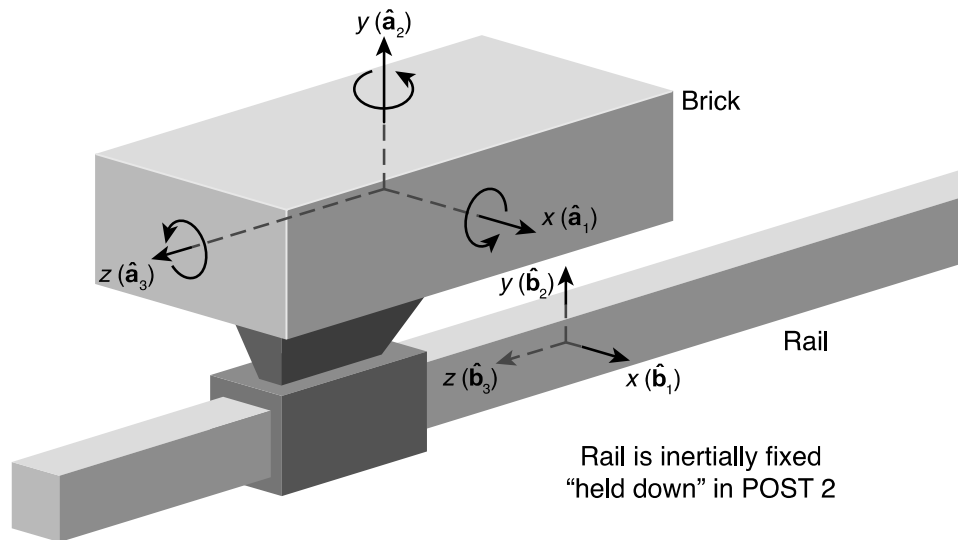
Figure 29.   Test Case 4: Translational joint.

Table 6. Mass Properties for Test Case 4.

| m	622 slugs
I_{xx}	220.3124 slug ft^2
I_{yy}	359.1252 slug ft^2
I_{zz}	64.8124 slug ft^2
Center of mass location in inertial system at $t = 0$	{0, 1.583333, –0.666667} ft
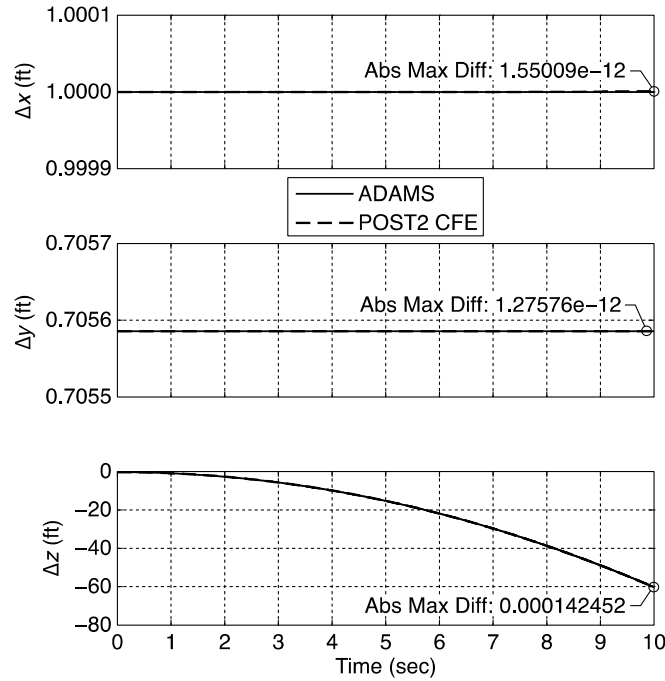
Figure 30. **Inertial position comparison between ADAMS® and POST2/CFE for the translational joint.**
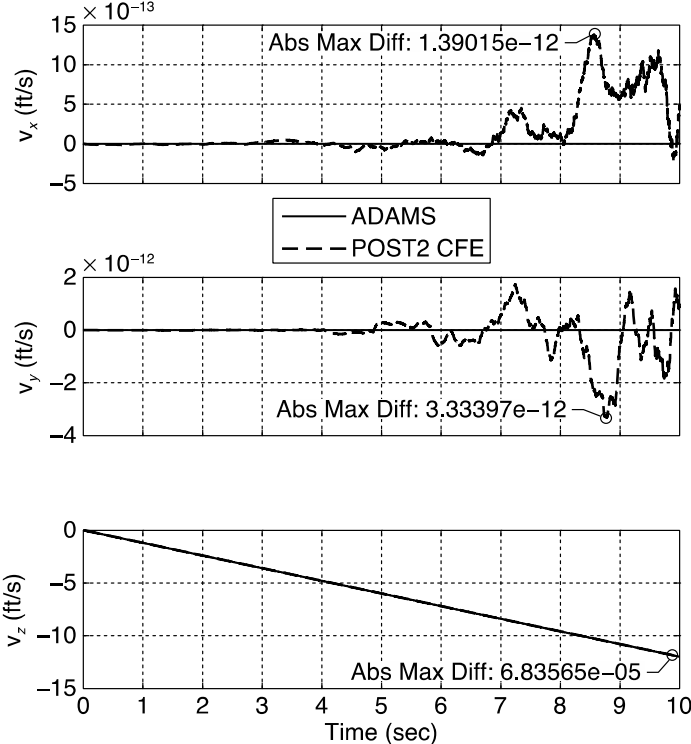
**Figure 31. Inertial velocity comparison between ADAMS® and POST2/CFE for the translational joint.**
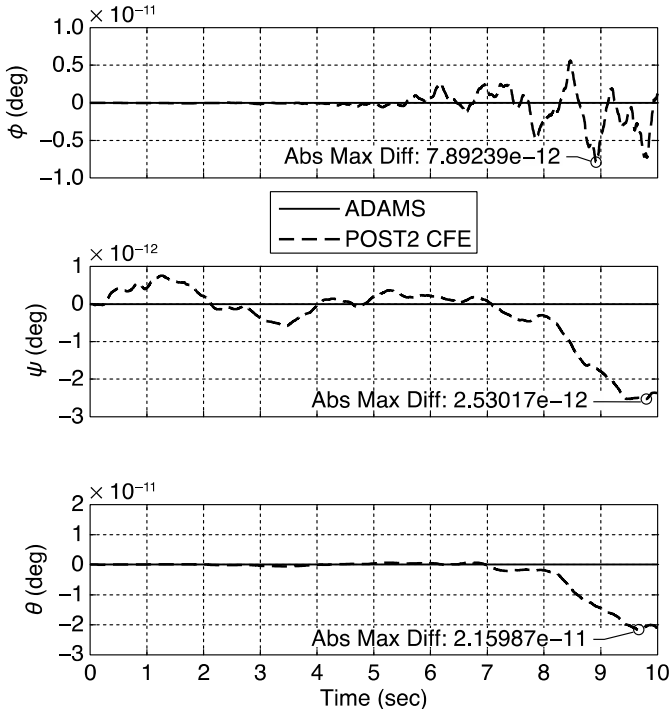
Figure 32. Euler angle (1-3-2 sequence) comparison between ADAMS® and POST2/CFE for the translational joint.
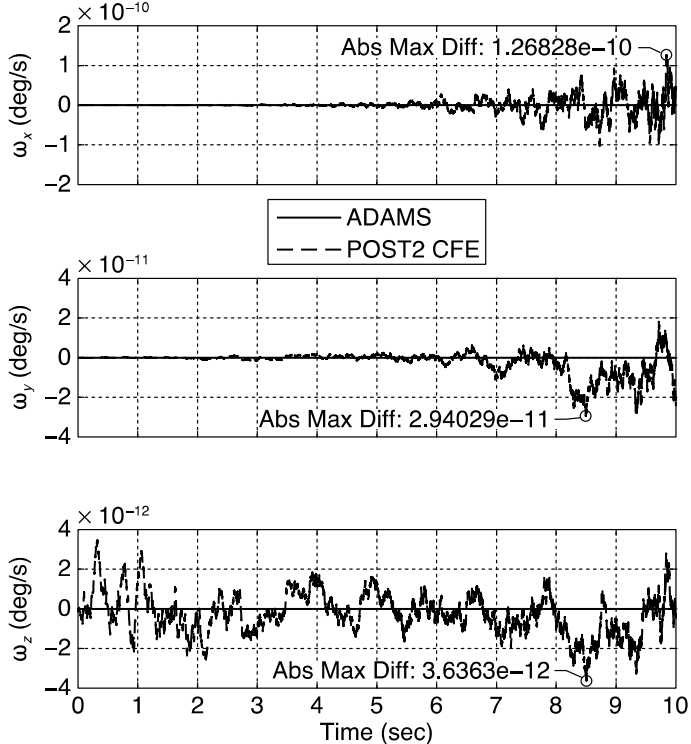
Figure 33. Brick body axis angular velocity comparison between ADAMS® and POST2/CFE for the translational joint.
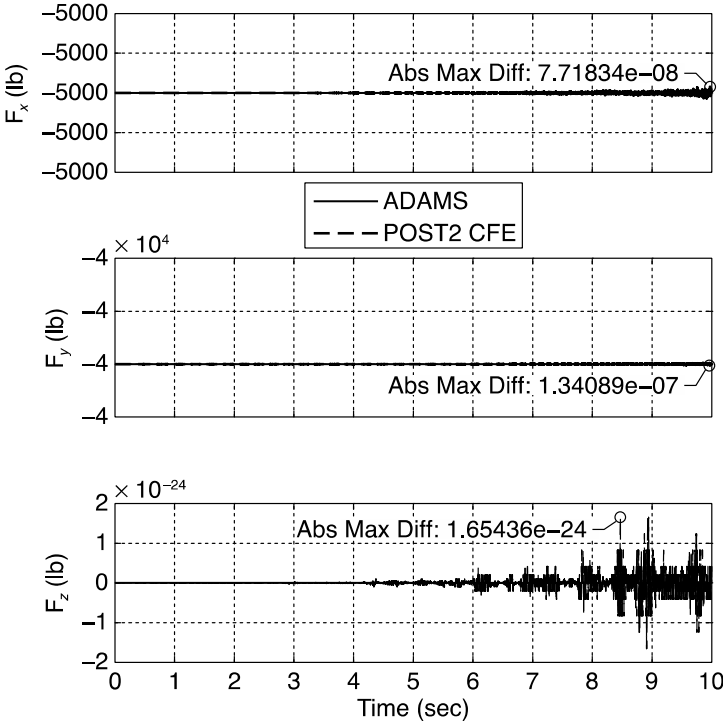
Figure 34. Constraint force (at the joint) comparison between ADAMS® and POST2/CFE for the translational joint.
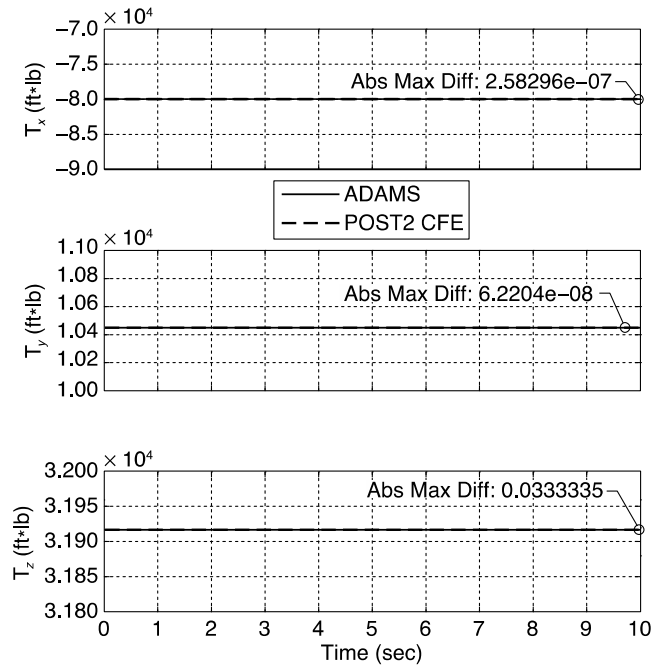
Figure 35. Constraint torque (at the joint) comparison between ADAMS® and POST2/CFE for the translational joint.
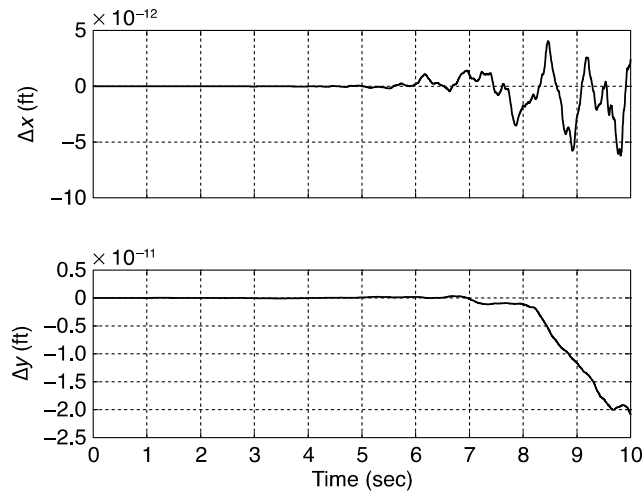
Figure 36. Relative *x* and *y* separation distances between the rail and the brick.
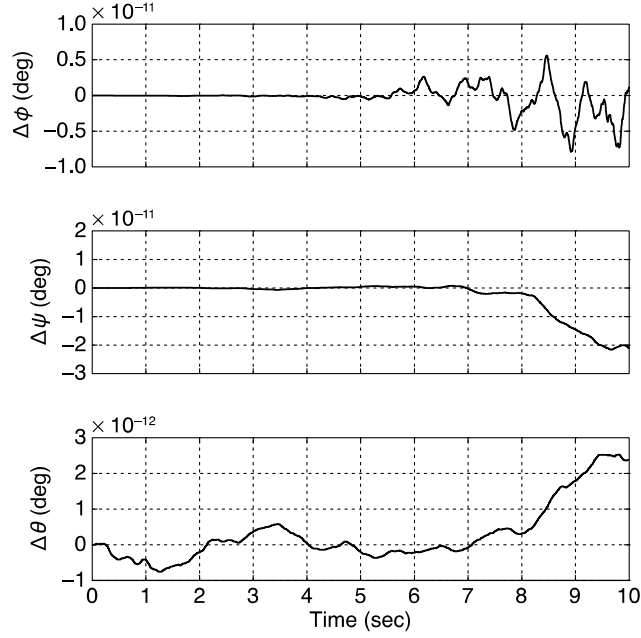
Figure 37. Relative joint orientation error between the joint connections of the rail and brick.

3.1.5   Test Case 5: Cylindrical Joint

This test case consists of a brick constrained to slide along a circular rail or rod using a cylindrical joint (fig. 38). A cylindrical joint is very similar to a translational joint, except that the rail's cross section is circular instead of rectangular. It permits sliding along the rail as in the case of a translational joint, but additionally, it permits relative rotation about the rail axis. The reference inertial axes system is located at the joint and is lined up with body axes systems of the Brick at $t = 0$. Table 7 presents the mass properties and the center of mass locations.

The joint constrains two rotational and two translational DOF between the two bodies allowing only relative translations and rotations along and about the z_b axis of the rod. The following equations define this constraint:

$$\left(\mathbf{r}^{O\bar{B}} - \mathbf{r}^{O\bar{A}}\right) \cdot \hat{\mathbf{a}}_1 = 0 \tag{110}$$

$$\left(\mathbf{r}^{O\bar{B}} - \mathbf{r}^{O\bar{A}}\right) \cdot \hat{\mathbf{a}}_2 = 0 \tag{111}$$

$$\hat{\mathbf{b}}_3 \cdot \hat{\mathbf{a}}_1 = 0 \tag{112}$$

$$\hat{\mathbf{b}}_3 \cdot \hat{\mathbf{a}}_2 = 0 \tag{113}$$

A constant external force with body axes component (0, 40000, –746) lb was applied to the brick at (–0.6, 0.5833, –1.33337) ft in body axes system. The brick translates along the rail, which is fixed inertially. The centerline of the rail, which is also the z-axis of the rail, coincides with the z inertial axis. Figures 39–46 show the comparison between ADAMS® and POST2/CFE results. The relative joint errors (fig. 46) are, $\Delta\phi = 90 - \mathrm{acos}\left(\hat{\mathbf{b}}_3 \cdot \hat{\mathbf{a}}_1\right)$, and, $\Delta\theta = 90 - \mathrm{acos}\left(\hat{\mathbf{b}}_3 \cdot \hat{\mathbf{a}}_2\right)$ respectively. ADAMS®

used its built-in (RKF45 single step integrator with adaptive step size using an error tolerance of 1.0e-11. POST2 used the single step fourth order Runge Kutta method with a fixed step size of 0.001s. The CFE Baumgarte factor was set to 10.0 to reduce joint constraint errors.
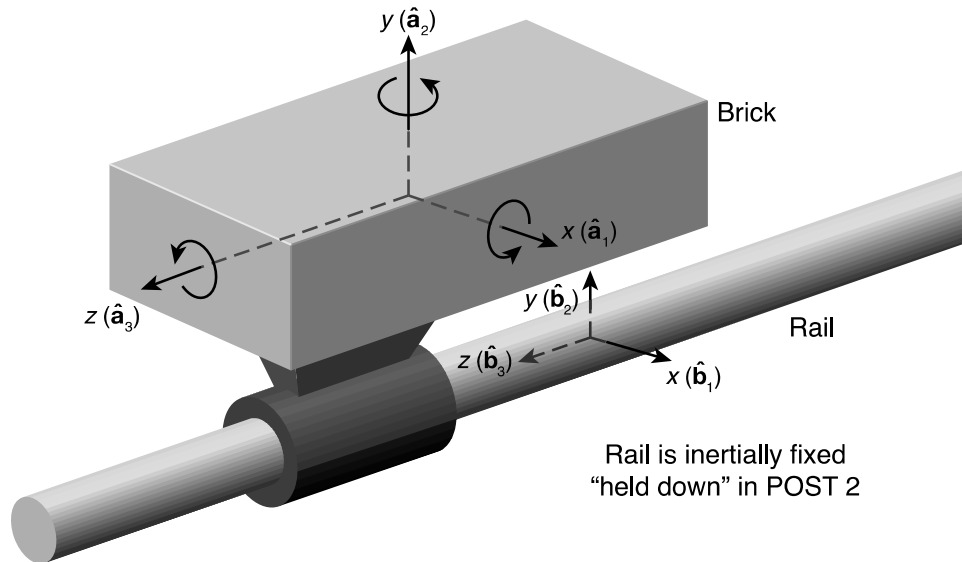

Figure 38.   Test Case 5: Cylindrical joint test case.

Table 7. Mass Properties for Test Case 5.

m	622 slugs
I_{xx}	220.3124 slug ft^2
I_{yy}	359.1252 slug ft^2
I_{zz}	64.8124 slug ft^2
Center of mass location in inertial system at $t = 0$	{0, 1.583333, −0.666667} ft

Figure 39. Inertial position comparison between ADAMS® and POST2/CFE for the cylindrical joint.
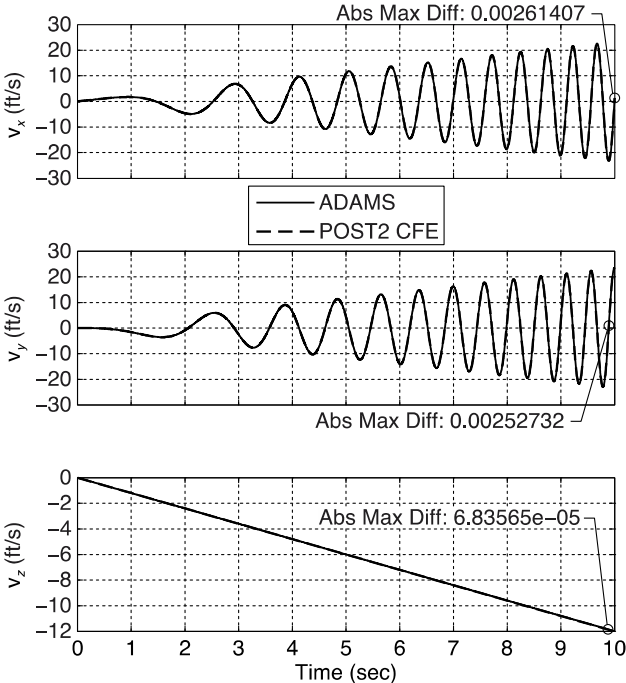
Figure 40. Inertial velocity comparison between ADAMS® and POST2/CFE for the cylindrical joint.
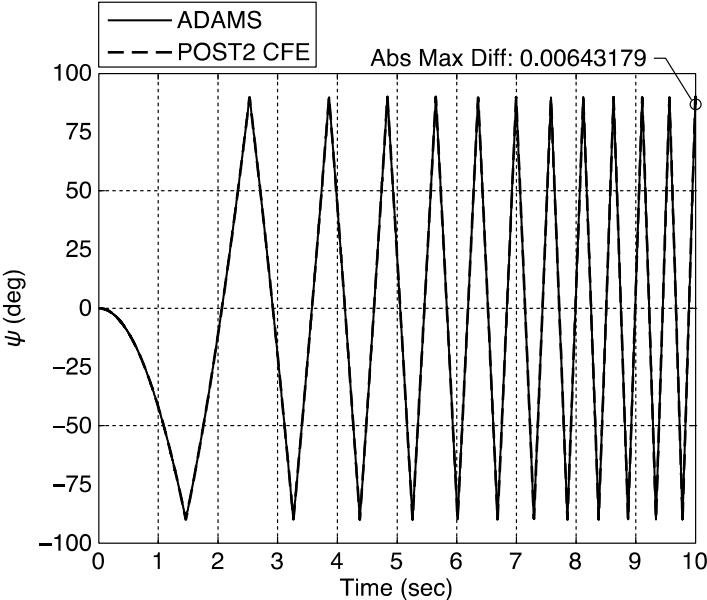
Figure 41.   Euler angle. ψ **(rotation about z axis) comparison between ADAMS® and POST2/CFE for the cylindrical joint.**
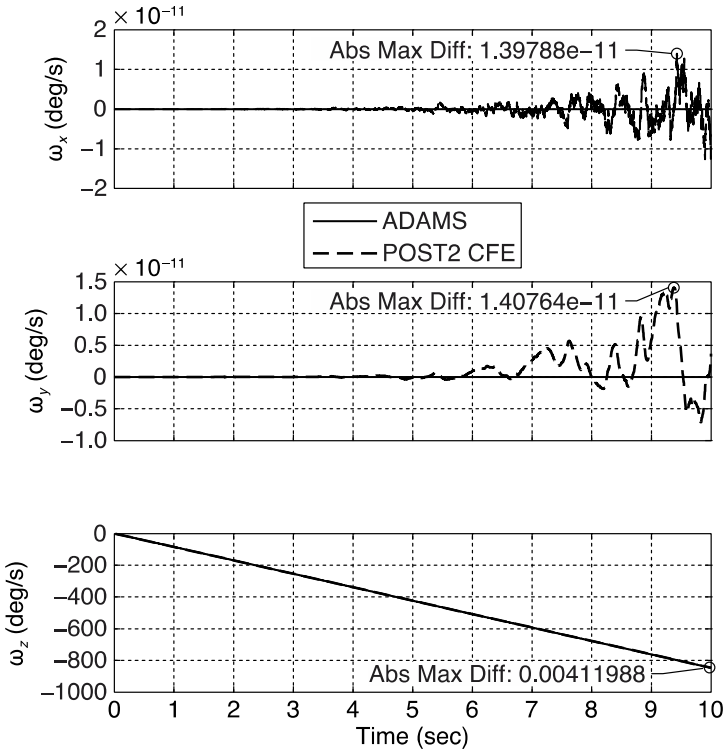
**Figure 42.   Brick inertial angular velocity comparison between ADAMS® and POST2/CFE for the cylindrical joint.**
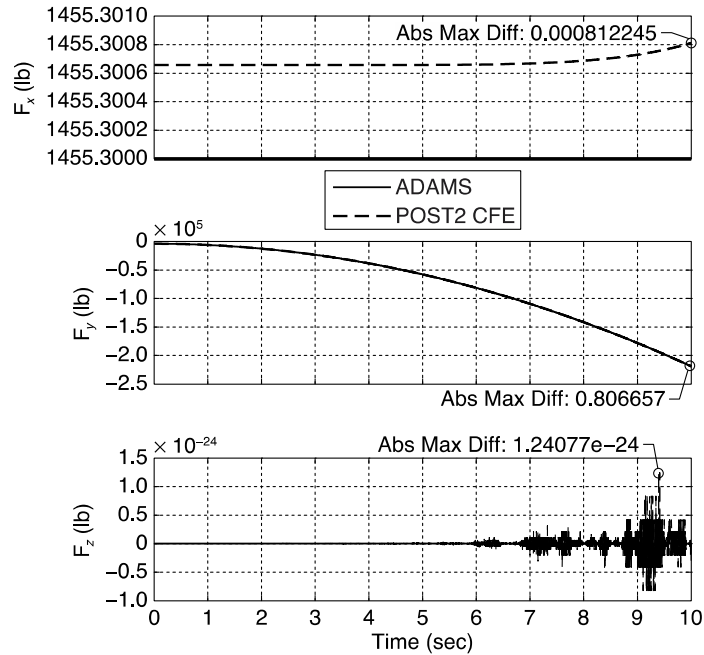
Figure 43. Brick body axis constraint force (at the joint) comparison between ADAMS® and POST2/CFE for the cylindrical joint.
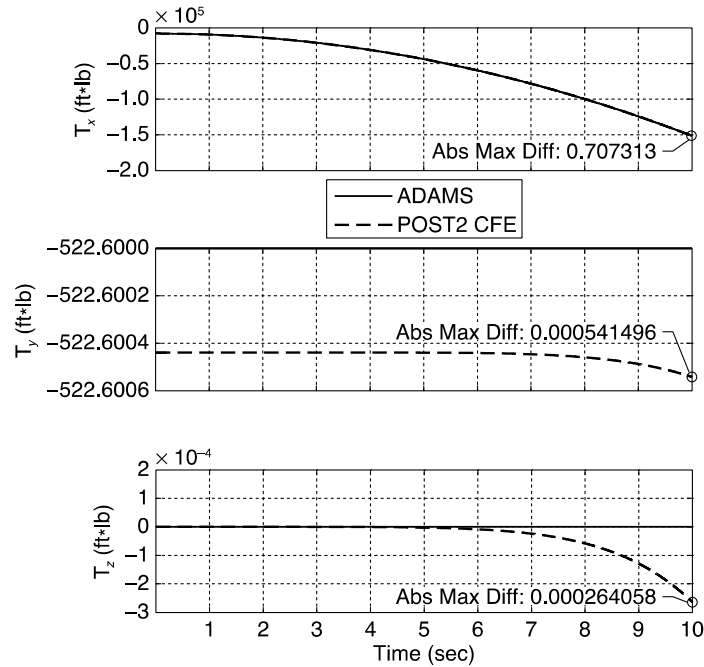

Figure 44. Brick body axis constraint torque (at the joint) comparison between ADAMS® and POST2/CFE for the cylindrical joint.
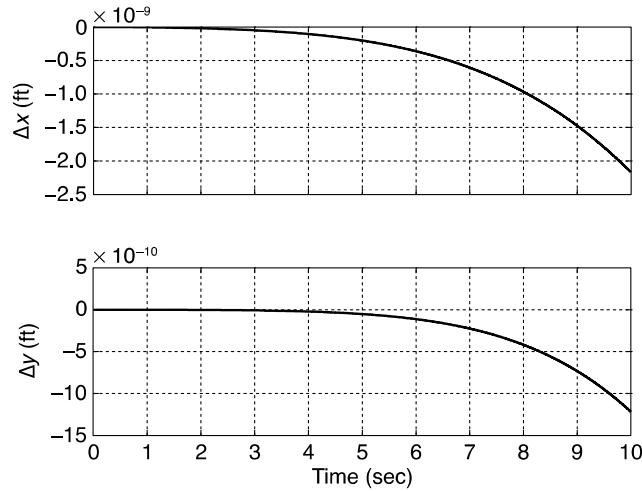
**Figure 45.   Relative x and y axis separation
between the rod and the brick.**
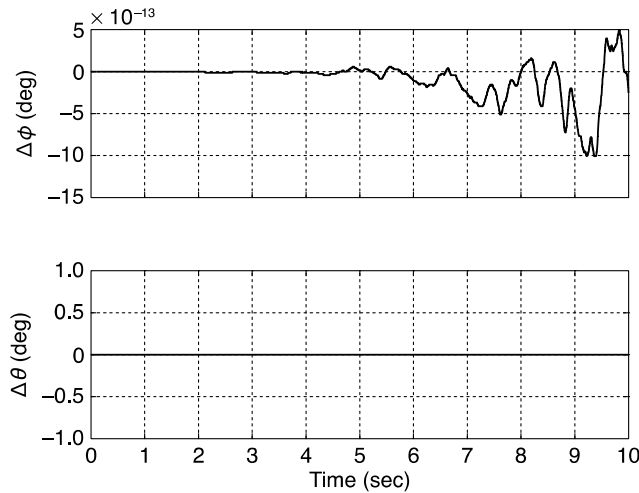
**Figure 46.   Relative joint orientation error between
the joint connections of the rod and brick.**

3.1.6   Test Case 6: Universal Joint

This test case consists of two boxes connected by a universal joint (fig. 47). A universal joint is a connection between two bodies that allows relative rotation about two axes at the joint location. One rotation axis is fixed in the primary rigid body, and the other is fixed in the secondary body. These two axes are supposed to remain perpendicular to each other at all times. The reference inertial axes system is located at the joint and is lined up with body axes systems of both Box 1 and Box 2 at $t = 0$. Table 8 presents the mass properties and the center of mass locations.

The joint constrains all three translational and one rotational DOF between the two boxes. Rotations are permitted about the y axis of Box 1 and about the z axis of Box 2 as illustrated in the figure. Therefore one must require that these two axes of rotation remain perpendicular at all times. The following equations define this constraint:

$$\left(\mathbf{r}^{O\bar{B}} - \mathbf{r}^{O\bar{A}}\right) \cdot \hat{\mathbf{a}}_1 = 0 \tag{114}$$

$$\left(\mathbf{r}^{O\bar{B}} - \mathbf{r}^{O\bar{A}}\right) \cdot \hat{\mathbf{a}}_2 = 0 \tag{115}$$

$$\left(\mathbf{r}^{O\bar{B}} - \mathbf{r}^{O\bar{A}}\right) \cdot \hat{\mathbf{a}}_3 = 0 \tag{116}$$

$$\hat{\mathbf{a}}_2 \cdot \hat{\mathbf{b}}_3 = 0 \tag{117}$$

A constant external force with body axes components $5000 * (5,5,1)/\sqrt{51}$ was applied to Box 1 at $(-2.0, 0, 0.5)$ ft in body axes system. Figures 48–55 show the output results between ADAMS® and POST2/CFE. Note that the relative joint orientation error shown in Figure 55 is the deviation from the required 90 deg angle constraint between the unit vectors $\hat{\mathbf{a}}_2$ and $\hat{\mathbf{b}}_3$. ADAMS® used its built-in RKF45 single step integrator with adaptive step size using an error tolerance of 1.0e-11. POST2 used the single step fourth order Runge Kutta method with a fixed step size of 0.001s. The CFE Baumgarte factor was set to 10.0 to reduce joint constraint errors.
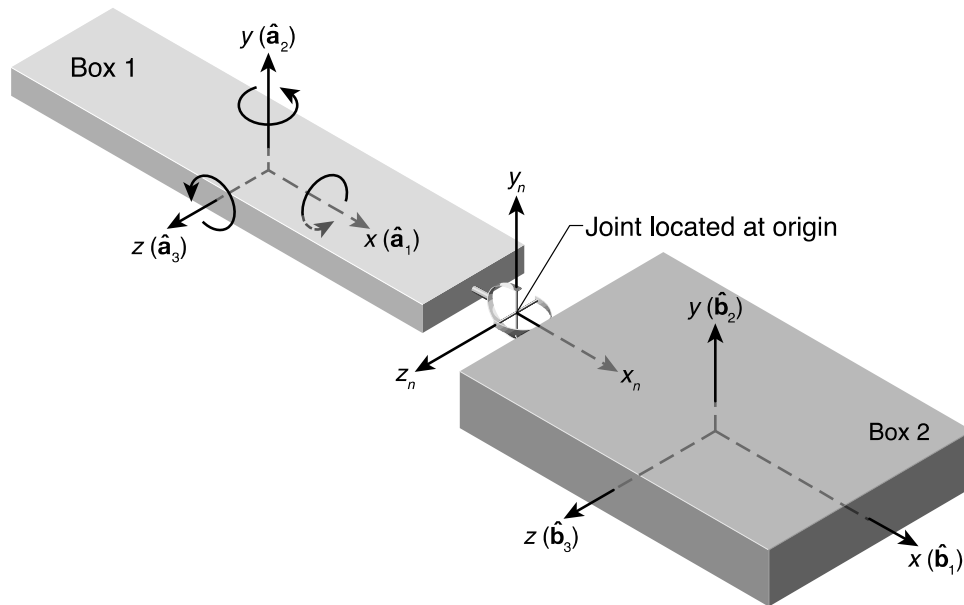

Figure 47. Test Case 6: Universal joint.

Table 8. Mass Properties for Test Case 6.

|	**Box 1**	**Box 2**
m	622 slugs	622 slugs
I_{xx}	220.2916667 slug ft^2	881.166667 slug ft^2
I_{yy}	3524.666667 slug ft^2	2695.33333 slug ft^2
I_{zz}	3330.291667 slug ft^2	1917.83333 slug ft^2
Center of mass location in inertial system at $t = 0$	{−4.854, −0.096, 0} ft	{3.851, −0.096, 0} ft

(a) Box 1.

(b) Box 2.

Figure 48. Inertial position comparison between ADAMS® and POST2/CFE for the universal joint.
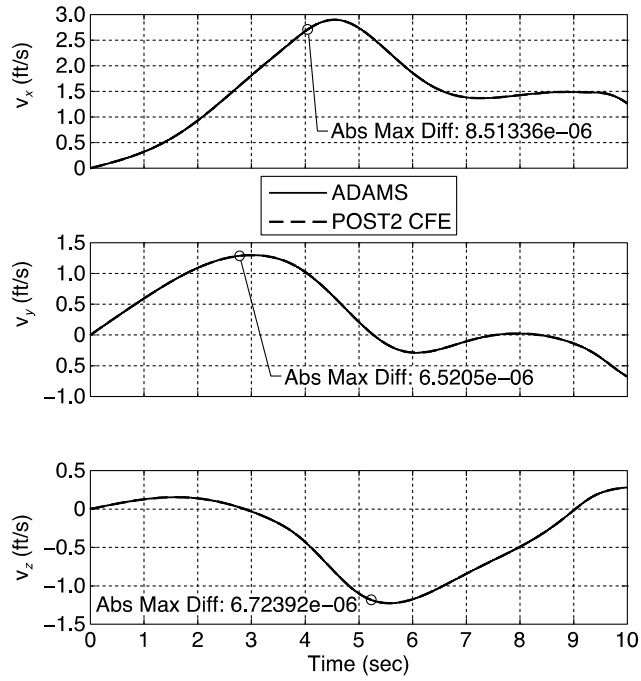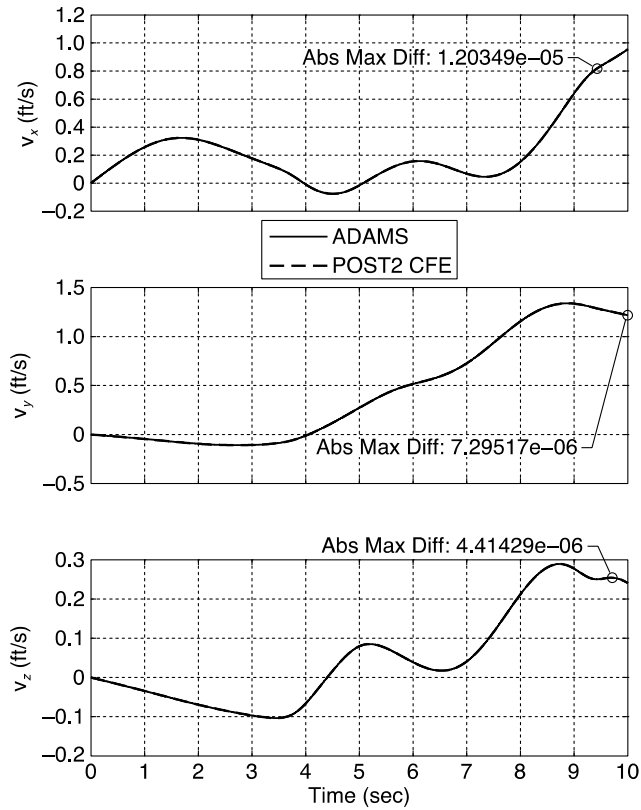
(a) Box 1.

(b) Box 2.

Figure 49. Inertial velocity comparison between ADAMS® and POST2/CFE for the universal joint.
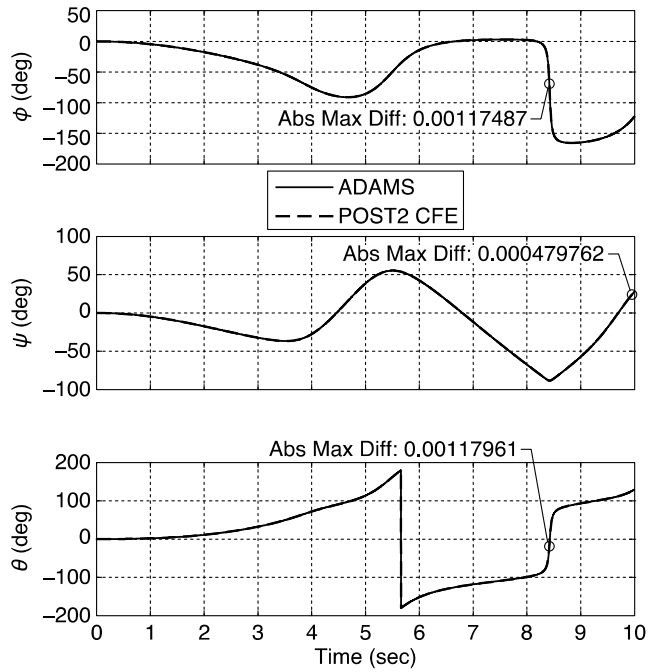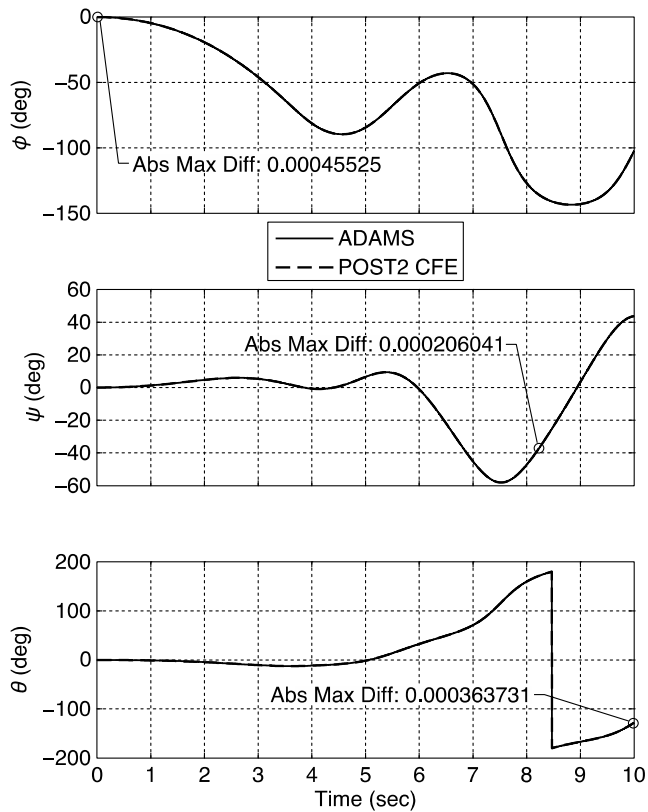
(a) Box 1.

(b) Box 2.

Figure 50.   Euler angle (1-3-2 sequence) comparison between ADAMS® and POST2/CFE for the universal joint.
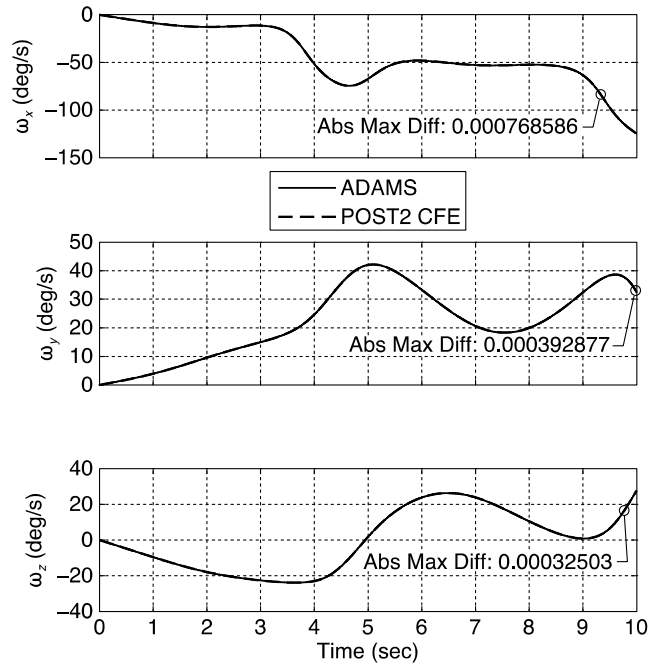
(a) Box 1.
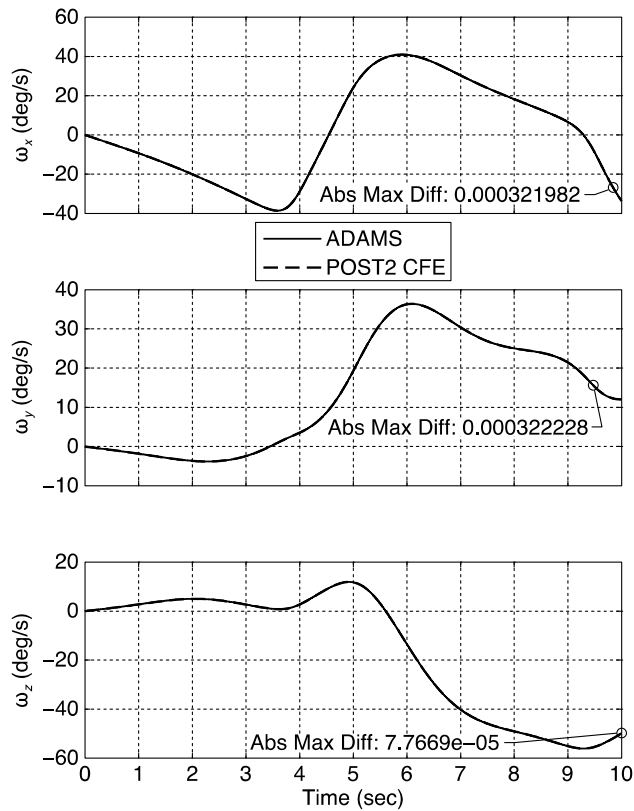
(b) Box 2.

Figure 51.   Body axis angular velocity comparison between ADAMS® and POST2/CFE for the universal joint.
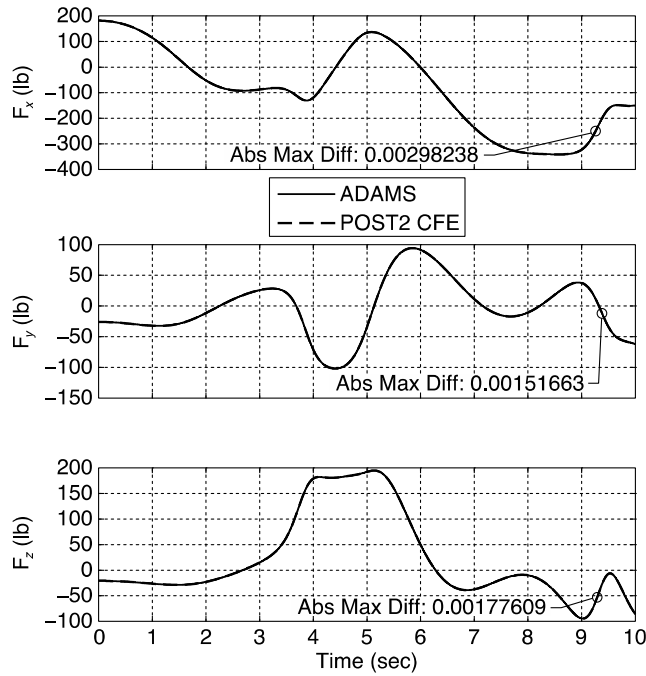
Figure 52. Constraint force (at the joint) comparison between ADAMS® and POST2/CFE for the universal joint.
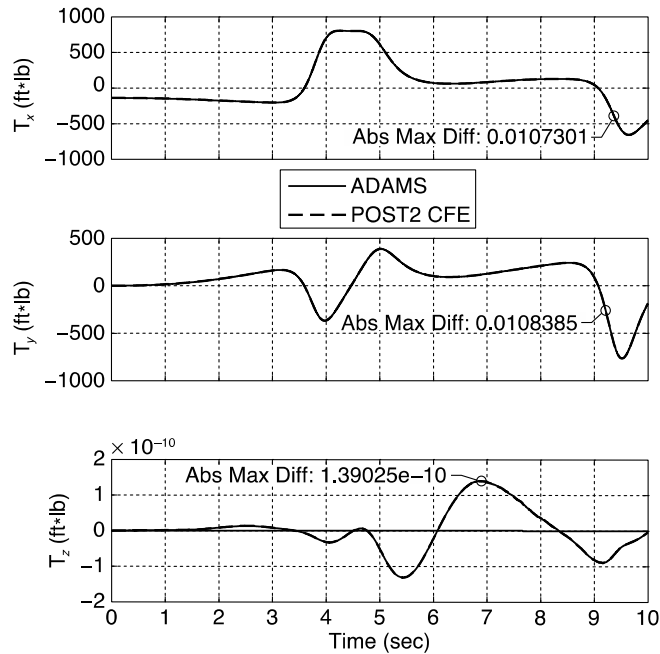

Figure 53. Constraint torque (at the joint) comparison between ADAMS® and POST2/CFE for the universal joint.
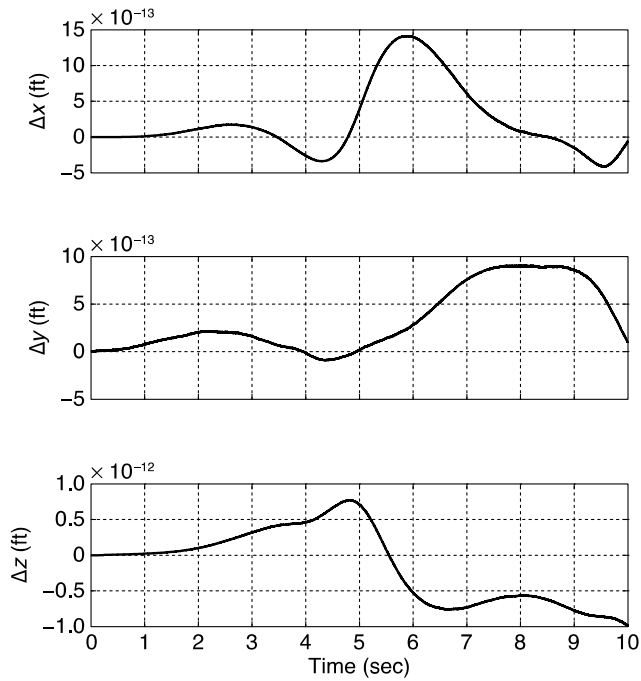
Figure 54. Relative joint separation between the connection points of Box 1 and 2 for universal joint.
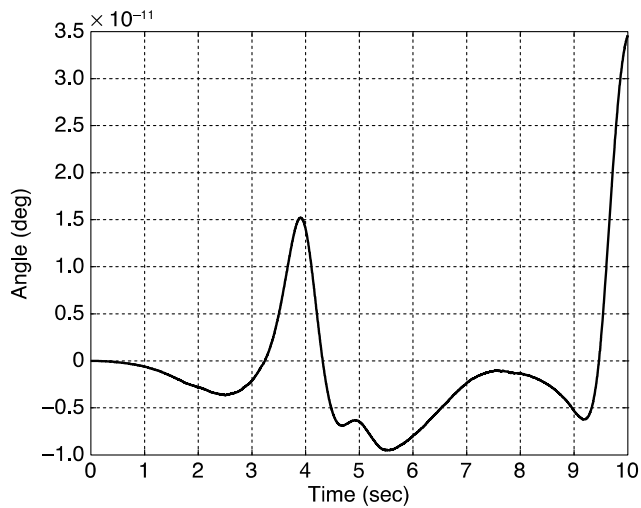

Figure 55. Relative joint orientation error between the joint connections of Box 1 and 2 for universal joint.

3.1.7   Test Case 7: Planar Joint

This test case consists of an upright cylinder constrained to slide along a table surface using a planar joint (fig. 56). A planar, or two-dimensional slider, joint can be thought of as a hockey puck spinning and sliding along a flat sheet of ice, where the puck cannot be pried from the ice. That is, this joint allows relative translation along a plane, and relative rotation about the axis perpendicular to that plane. The reference inertial axes system is located at the joint and is lined up with body axes systems of both Box 1 and Box 2 at $t = 0$. The mass properties and the center of mass locations are presented in table 9.

The joint constrains one translational and two rotational DOF between the cylinder and table by restricting relative translation along and permitting relative rotation about the table's (and cylinder's) y axis. The following equations define this constraint:

$$\left(\mathbf{r}^{O\bar{B}} - \mathbf{r}^{O\bar{A}} \right) \cdot \hat{\mathbf{a}}_2 = 0 \tag{118}$$

$$\hat{\mathbf{b}}_2 \cdot \hat{\mathbf{a}}_1 = 0 \tag{119}$$

$$\hat{\mathbf{b}}_2 \cdot \hat{\mathbf{a}}_3 = 0 \tag{120}$$

A constant external force with body axes components (–10, 2000, –6.0) lb was applied to the cylinder at (0.3, –0.08333, –0.5) ft in body axes system. Additionally, the table is inertially fixed so that it cannot move. Figures 57–64 show the comparison of ADAMS® and POST2/CFE results. The relative joint errors (fig. 64) about x and y axes are, $\Delta\phi = 90 - \text{acos} \ (\hat{\mathbf{b}}_2 \cdot \hat{\mathbf{a}}_1)$, and, $\Delta\psi = 90 - \text{acos}$ $(\hat{\mathbf{b}}_2 \cdot \hat{\mathbf{a}}_3)$ respectively. ADAMS® used its built-in RKF45 single step integrator with adaptive step size using an error tolerance of 1.0e–11. POST2 used the single step fourth order Runge-Kutta method with a fixed step size of 0.001s. The CFE Baumgarte factor was set to 10.0 to reduce joint constraint errors.
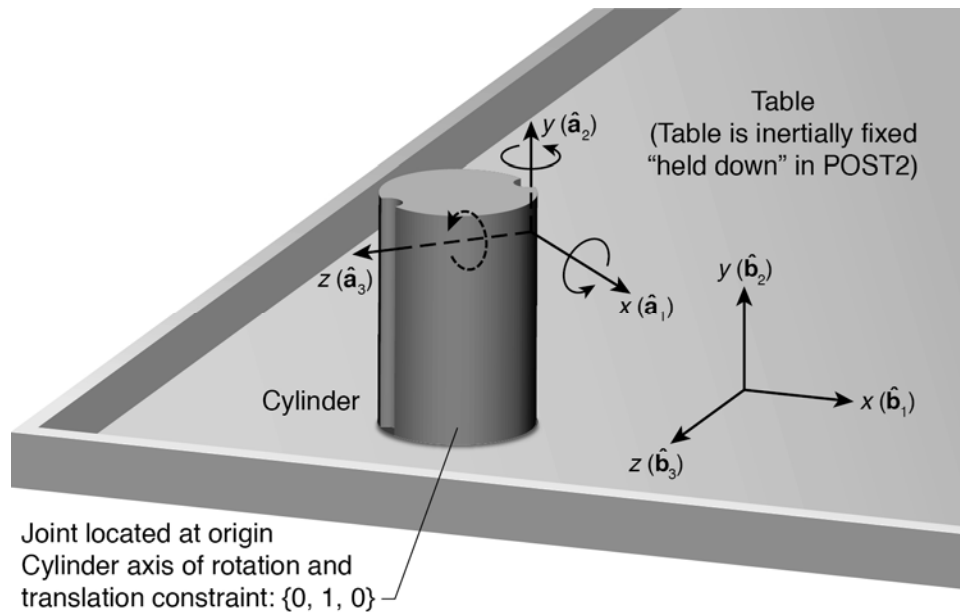

Figure 56.   Test Case 7: Planar joint test case.

Table 9. Mass Properties for Test Case 7.

| m	5 slug
I_{xx}	1.771 slug ft^2
I_{yy}	2.083 slug ft^2
I_{zz}	0.521 slug ft^2
cg	{0, 1.5833333, 0}ft
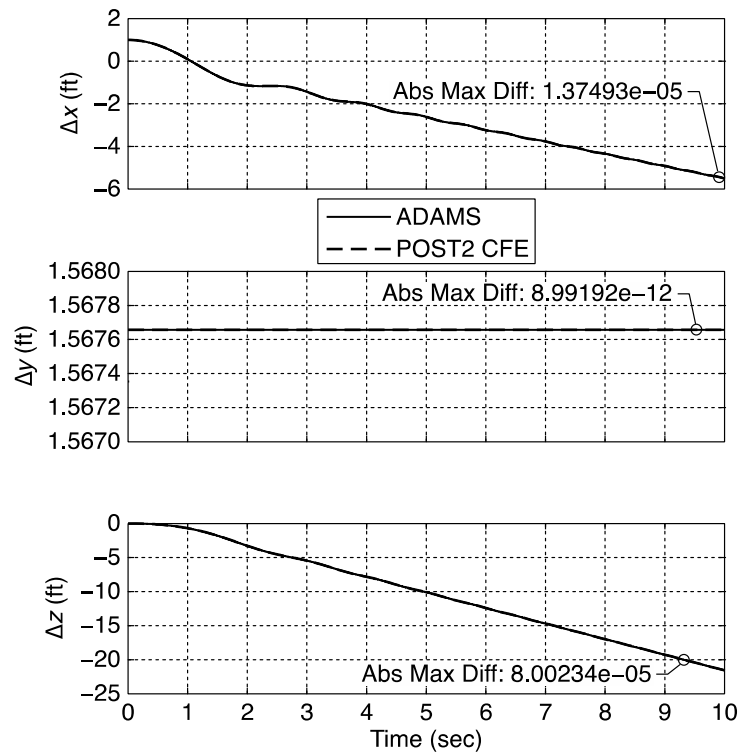
Figure 57. Cylinder inertial position comparison between ADAMS® and POST2/CFE for the planar joint.
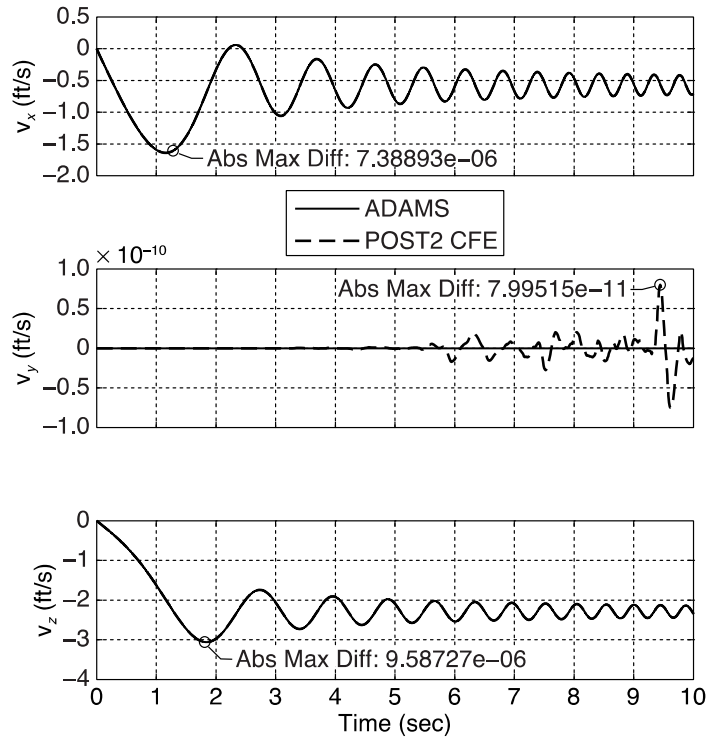
Figure 58. Cylinder inertial velocity comparison between ADAMS® and POST2/CFE for the planar joint.
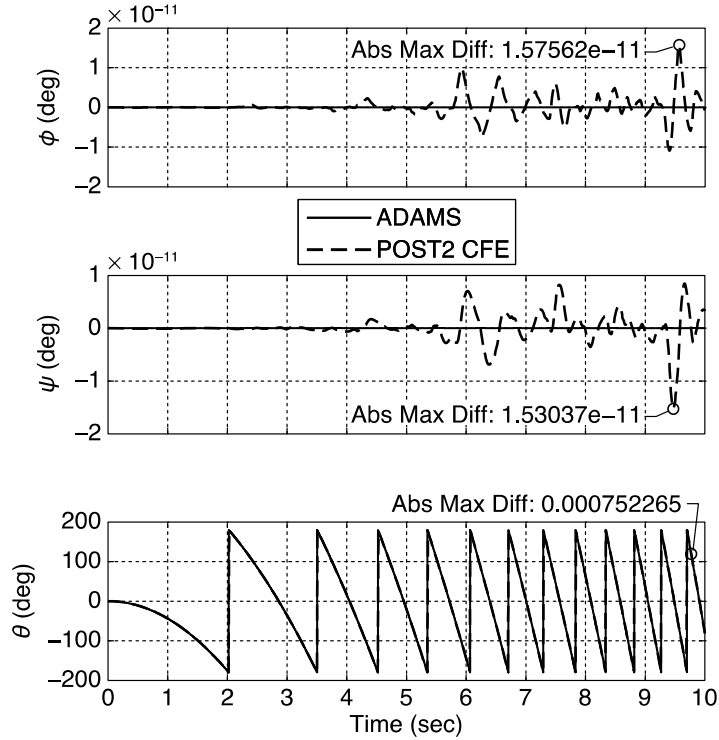

Figure 59. Euler angle (1-3-2 sequence) comparison between ADAMS® and POST2/CFE for the planar joint.
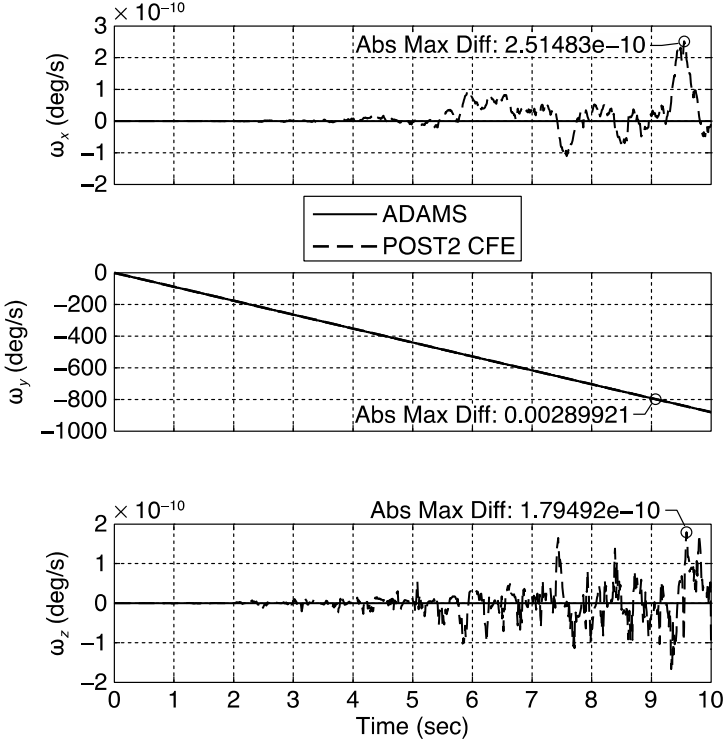
Figure 60. Cylinder body axis angular velocity comparison between ADAMS® and POST2/CFE for the planar joint.
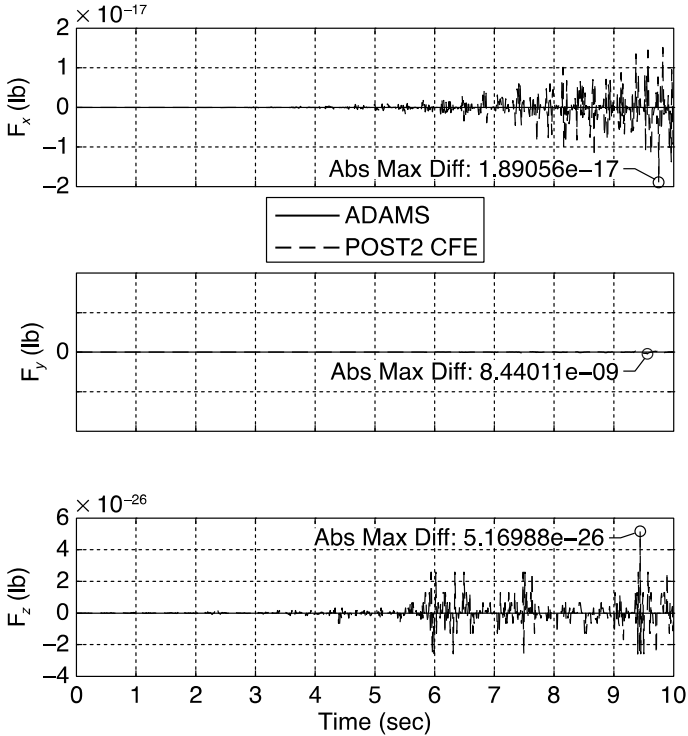

Figure 61. Constraint force (at the joint) comparison between ADAMS® and POST2/CFE for the planar joint.
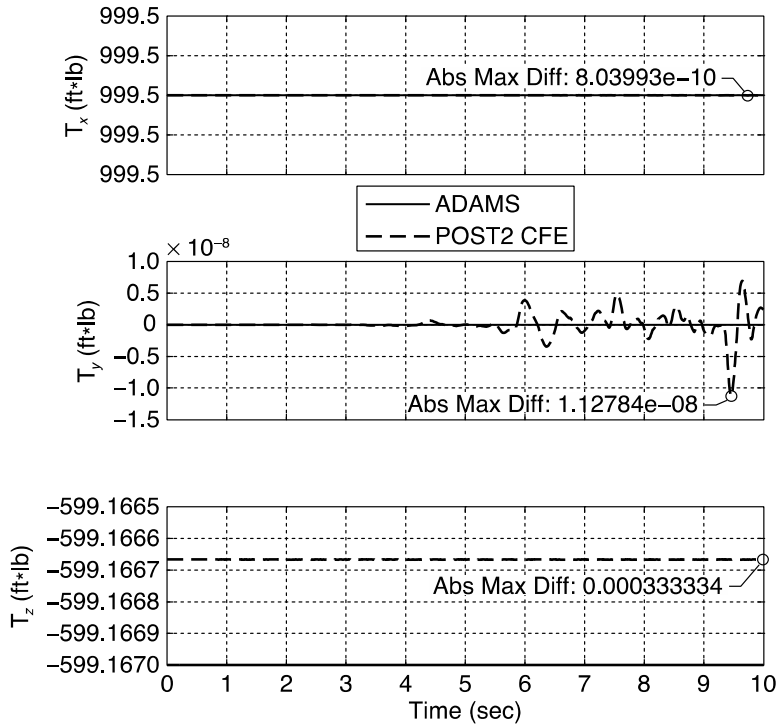
Figure 62. Constraint torque (at the joint) comparison between ADAMS® and POST2/CFE for the planar joint.
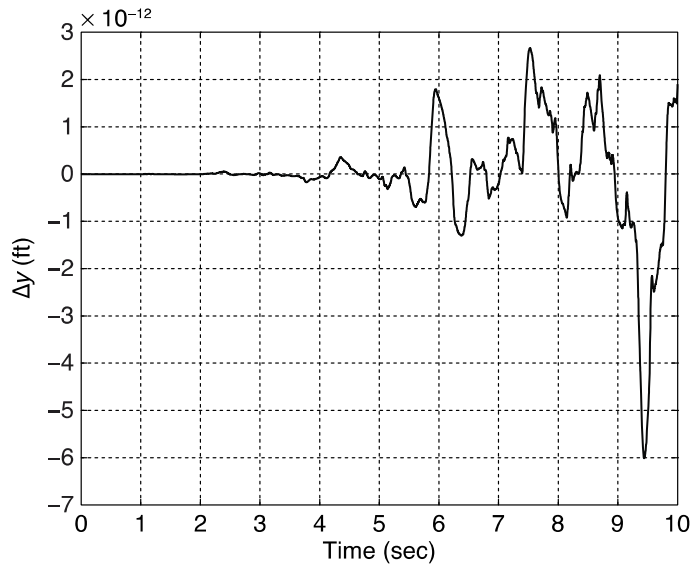

Figure 63. Relative joint separation between the cylinder and table connection points, represented in inertial frame components.
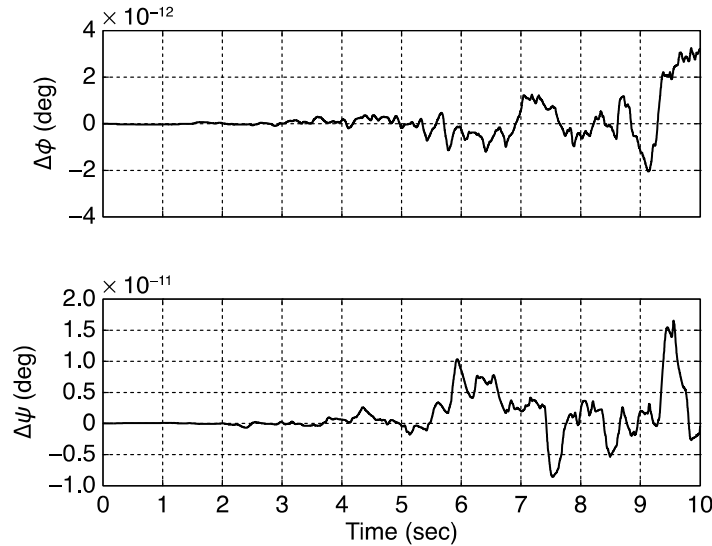
**Figure 64.   Relative joint orientation error between
the joint connections of the table and cylinder.**

3.2   Concept of Generalized Joint

The simple joints discussed above for various test cases need special coding for each case, which requires considerable effort for a new user. To facilitate easier implementation of the CFE method, all required coding was developed and integrated into the generalized joint, which permits the user to simulate any of the specific joint types described previously. The generalized joint facilitates the user to make appropriate selections as needed without needing the user to write specific CFE code and link it to POST2 for each joint type.

To test the generalized joint software, following subsets of the above test cases were rerun using the generalized joint. For each case, the respective predefined joints were replaced with equivalent generalized joints to replicate the simulation results. The generalized joint performed as expected and matched the original results closely and in many cases, identically. Small differences that were observed are attributed to orientation differences in joint coordinate systems set up in the algorithm. In particular, the orientations are automatically assigned for the predefined joints by the CFE algorithm, whereas they are user defined for the generalized joint. Thus, the exact system of equations may have been different between the two solutions, even though the same constraints are ultimately being applied. The POST2/CFE user guide (ref. 30) presents a complete description of the construct and implementation of the generalized joint.

3.2.1 Generalized Spherical Joint

The results for the generalized spherical joint were identical to the predefined spherical joint type as shown in figs 65–71. Here, only results for Box 1 are presented.
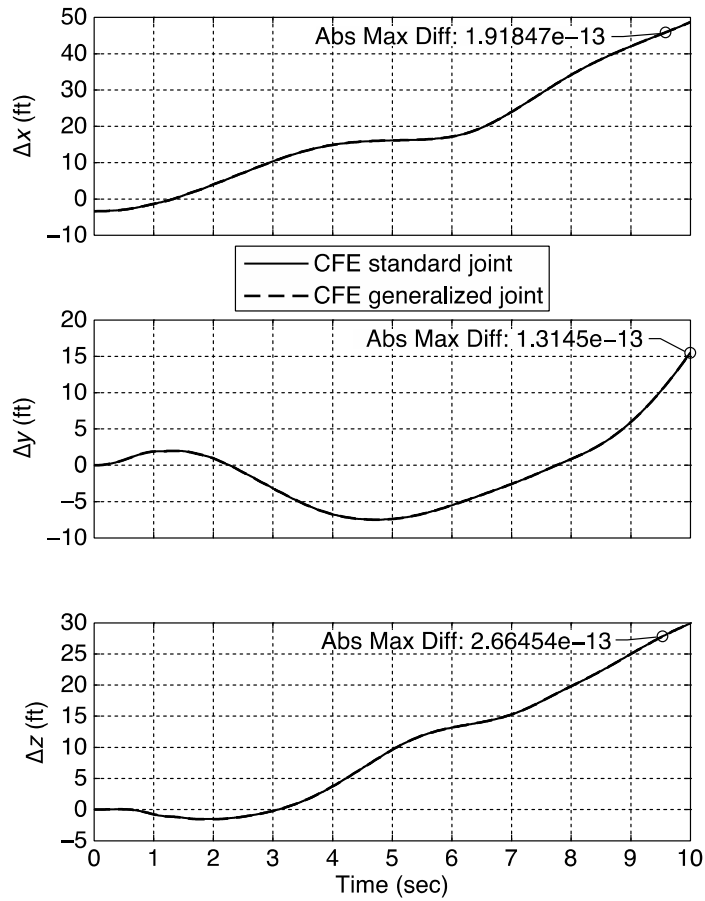

Figure 65. Box 1 inertial position comparison between POST2/CFE standard spherical joint and generalized joint.
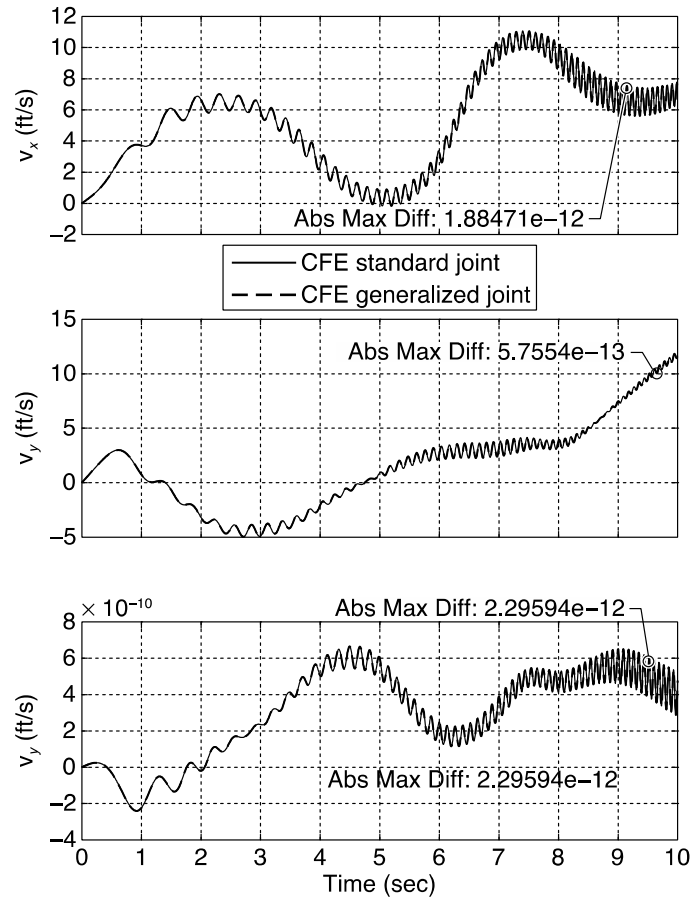
Figure 66. Box 1 inertial velocity comparison between POST2/CFE standard spherical joint and generalized joint.
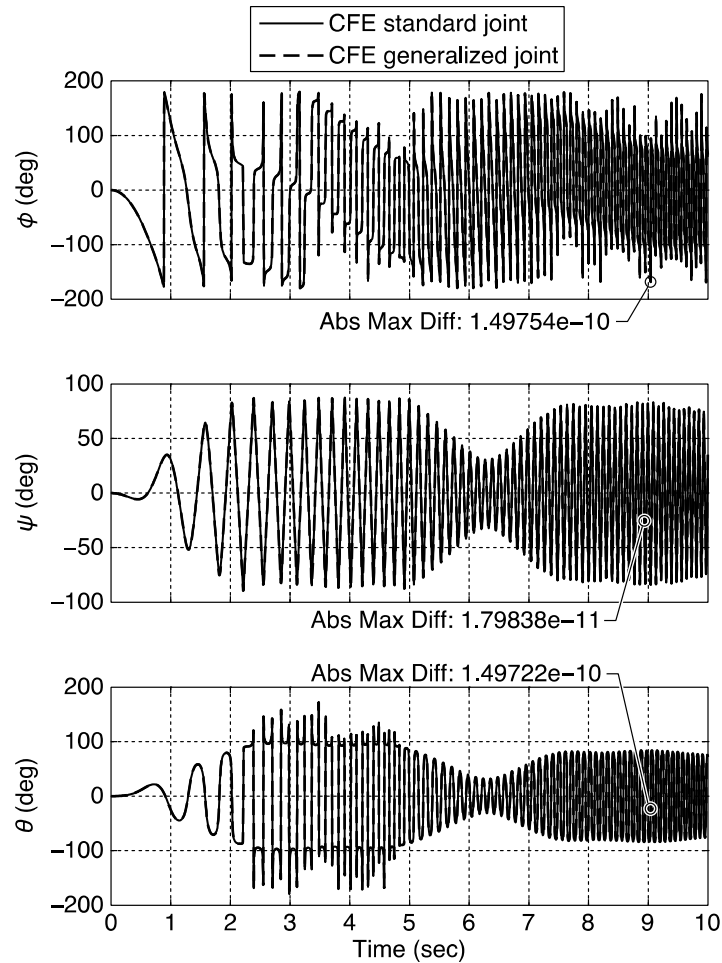
Figure 67.   Box 1 Euler angle (1-3-2 sequence) comparison between POST2/CFE standard spherical joint and generalized joint.
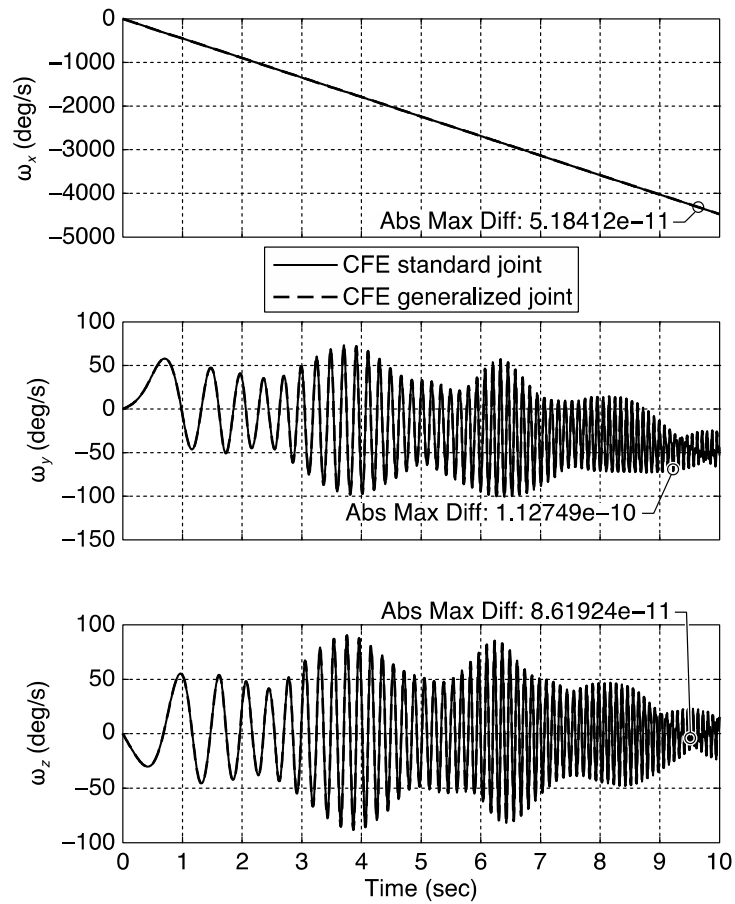
Figure 68. Box 1 body axis angular velocity comparison between POST2/CFE standard spherical joint and generalized joint.
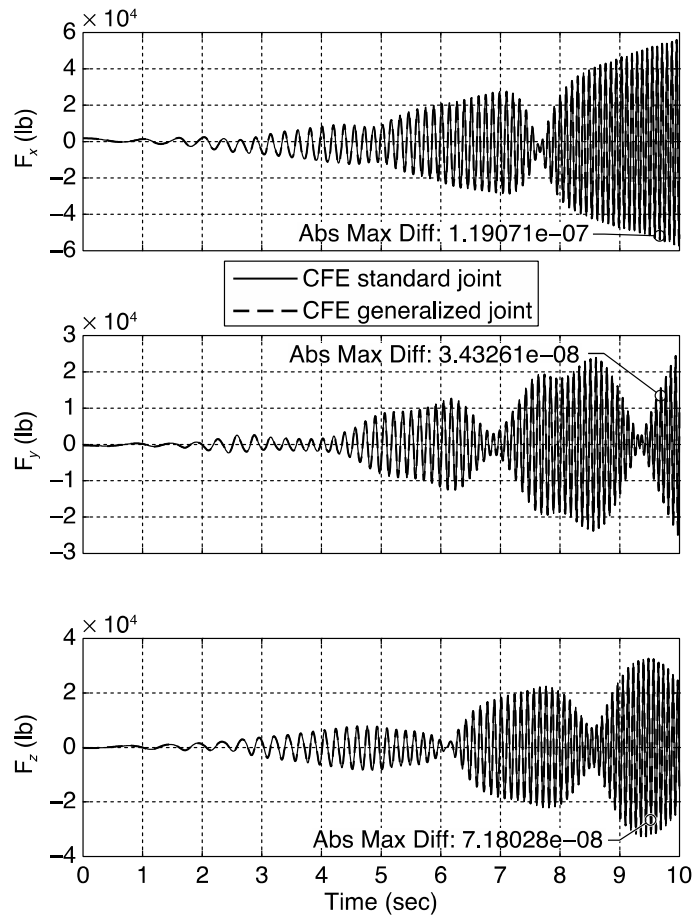
Figure 69. Constraint force comparison between POST2/CFE standard spherical joint and generalized joint.
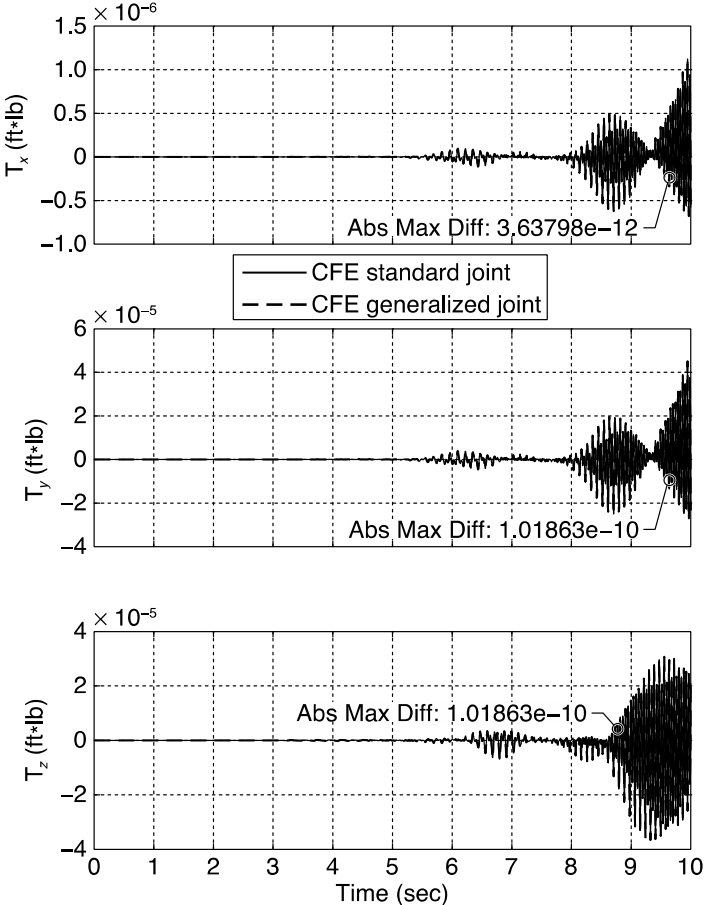
Figure 70. Constraint torque comparison between POST2/CFE standard spherical joint and generalized joint.

3.2.2   Generalized Universal Joint

The results for the generalized universal joint were nearly identical to the predefined universal joint type. Figure 71 shows that the notable difference is in the first two translational constraint violations. This is because the *x* and *y* axes of the translational joint coordinate system were flipped between the two simulations. Again this is because of orientation differences between the pre-defined universal joint and the way it was defined in the generalized joint version. Figures 72–79 present the results for Box 1. Note that, as said earlier, the relative joint orientation error shown in Figure 79 is the deviation from the required 90 deg angle constraint between the unit vectors $\hat{\mathbf{a}}_2$ and $\hat{\mathbf{b}}_3$ (Figure 47). For simplicity, results for Box 2 are not present.
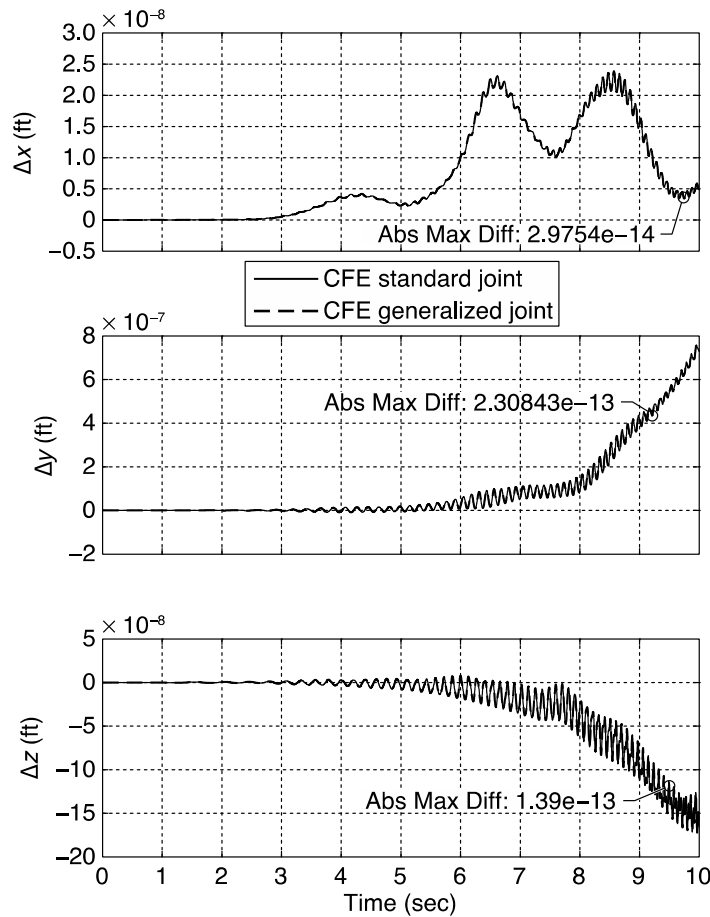
Figure 71. Comparison of relative joint separation between the connection points of Box 1 and 2, represented in the body frame of Box 1 for POST2/CFE standard universal joint and generalized joint.
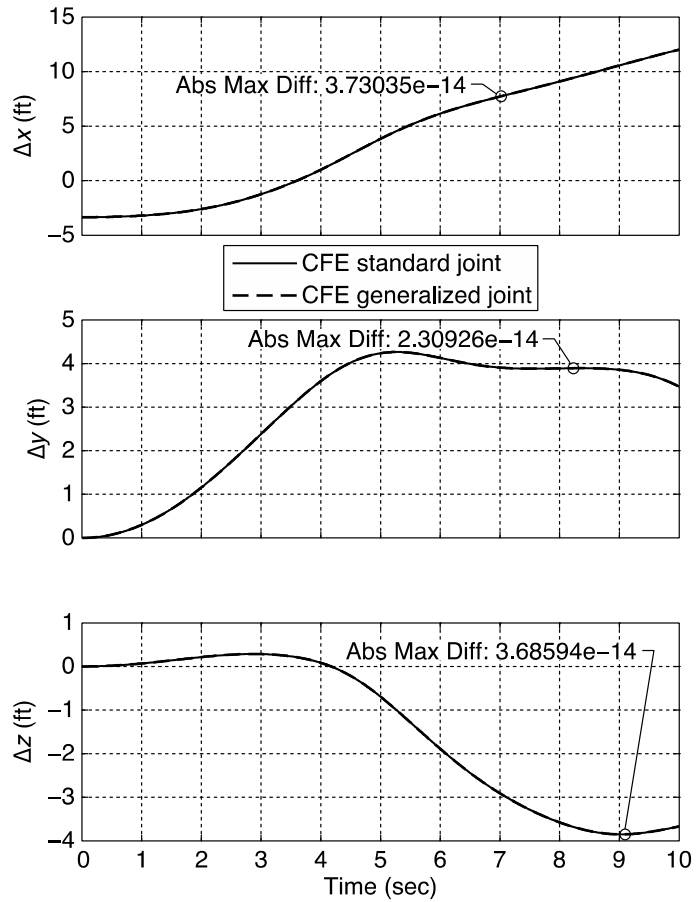
Figure 72. Box 1 inertial position comparison between POST2/CFE standard universal joint and generalized joint.
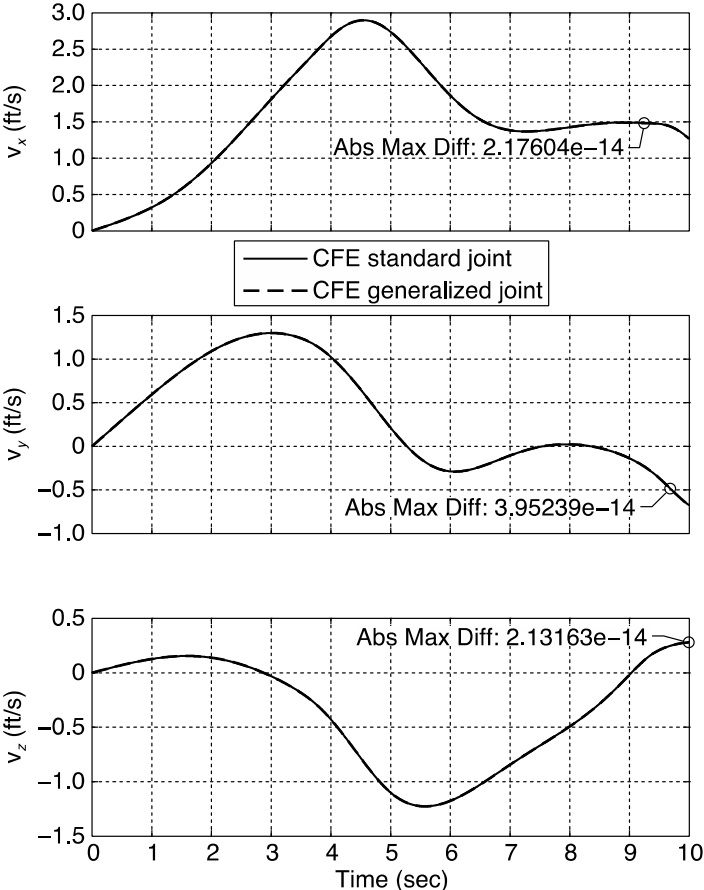
Figure 73. Box 1 inertial velocity comparison between POST2/CFE standard universal joint and generalized joint
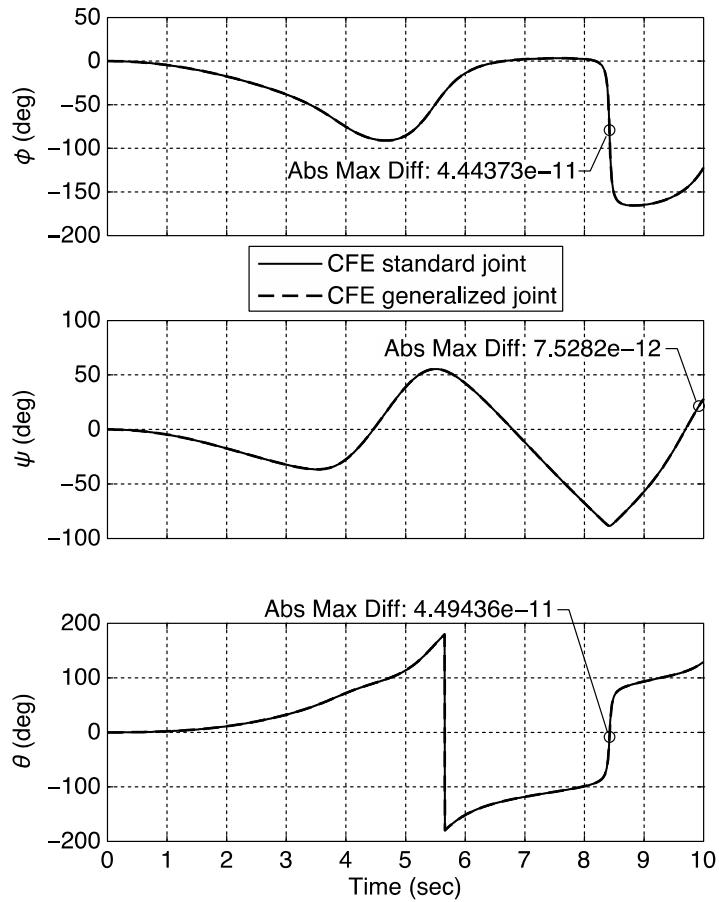
Figure 74. Box 1 Euler angle (1-3-2 sequence) comparison between POST2/CFE standard universal joint and generalized joint.
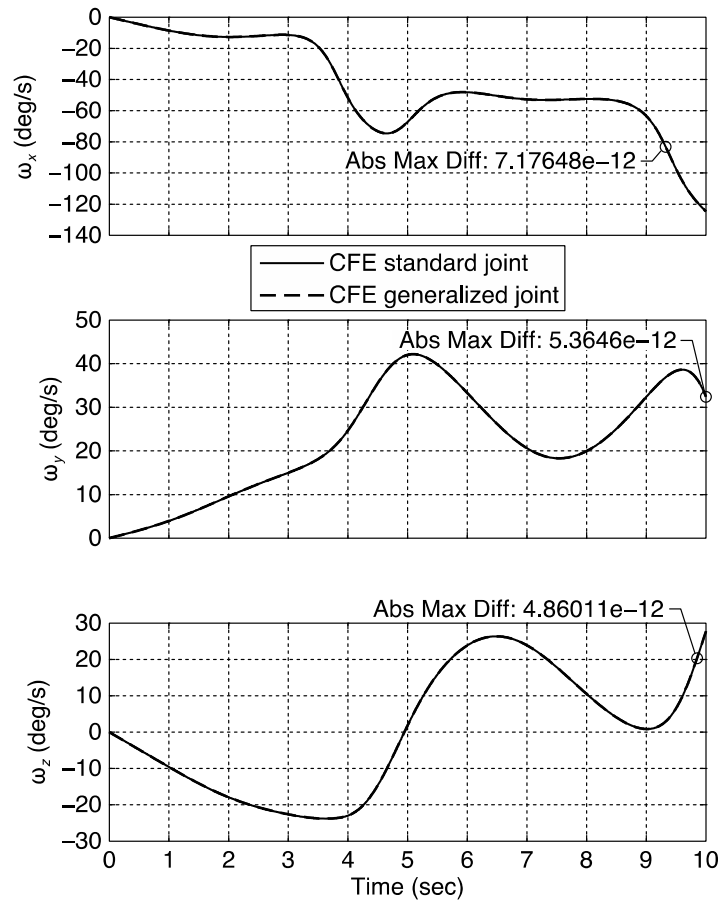
**Figure 75. Box 1 body axis angular velocity comparison
between POST2/CFE standard universal joint and
generalized joint.**
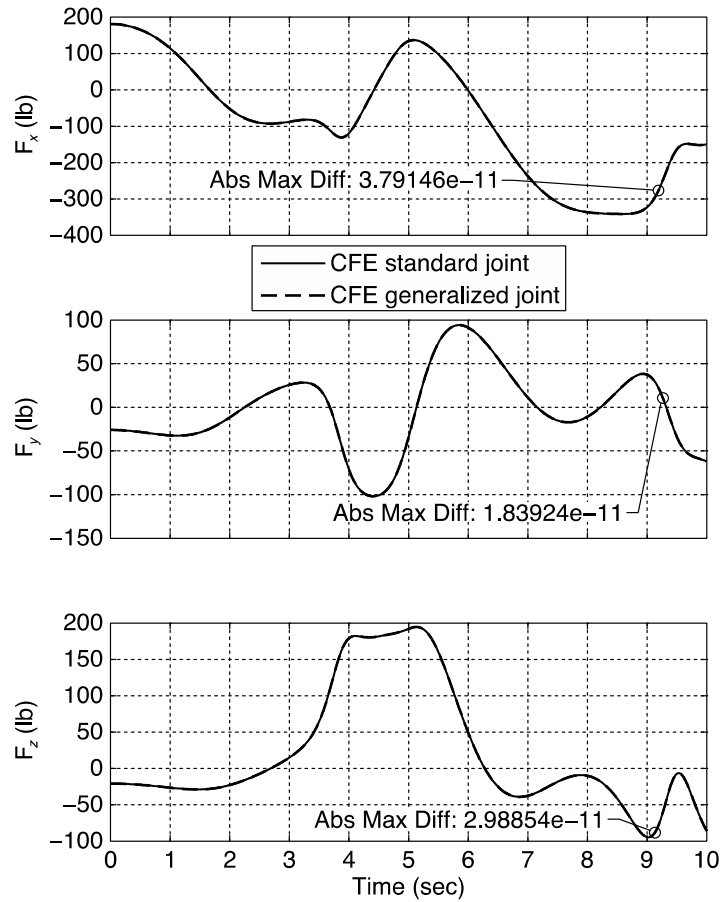
Figure 76. Constraint force comparison between POST2/CFE standard universal joint and generalized joint
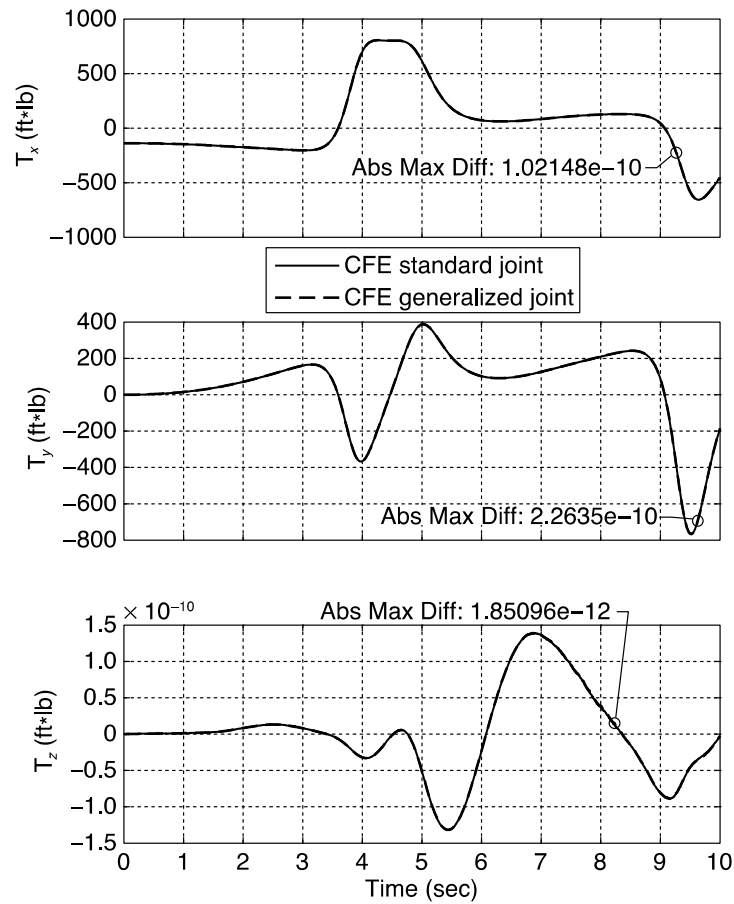
Figure 77. Constraint torque comparison between POST2/CFE standard universal joint and generalized joint.
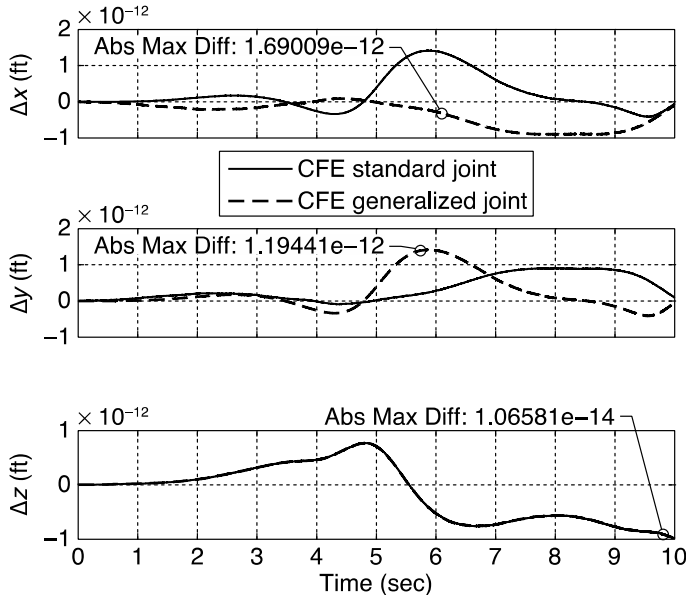
**Figure 78. Comparison of relative joint
separation between the connection points of
Box 1 and 2 for POST2/CFE standard
universal joint and generalized joint.**
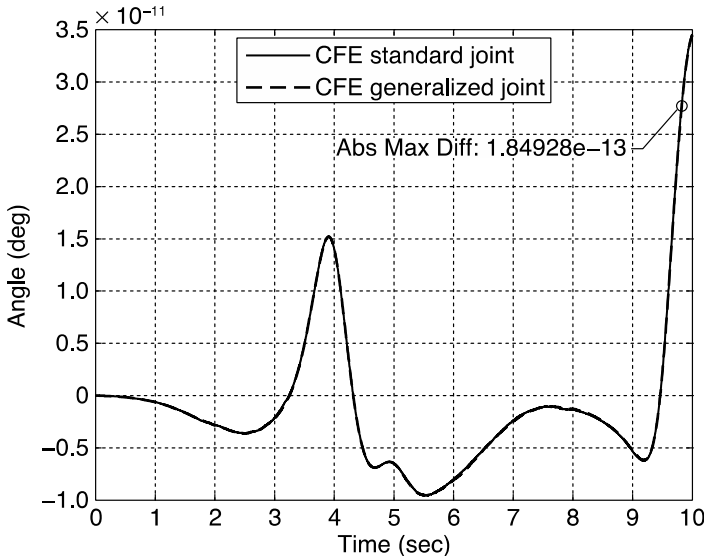
**Figure 79. Comparison of relative joint orientation
error between the joint connections of Box 1 and 2
for POST2/CFE standard universal joint and
generalized joint.**

3.2.3   Generalized Planar Joint

The results for the generalized planar joint were very close to the predefined planar joint type. Slight differences were observed in several of the plots where the scale was on a very small magnitude. Again this is because of joint coordinate system orientation difference between the predefined planar joint, and the way it was defined in the generalized joint version. Figures 80–87 present the results. The relative joint errors $\Delta\phi$ and $\Delta\psi$ shown in fig. 87 were computed in the same way as those shown previously in fig. 64.
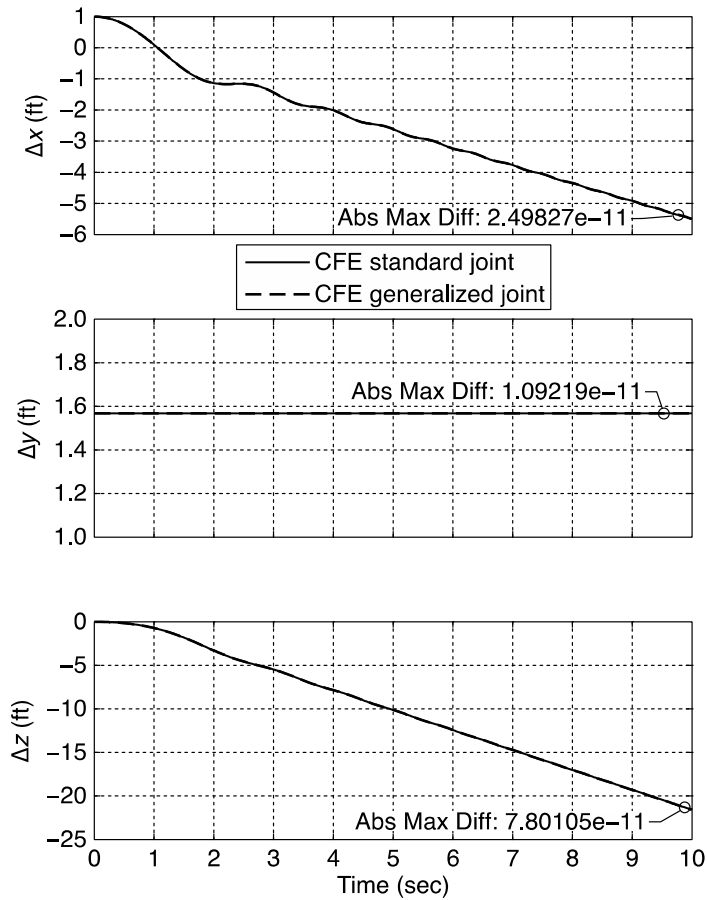
Figure 80. Cylinder inertial position comparison between POST2/CFE standard planar joint and generalized joint.
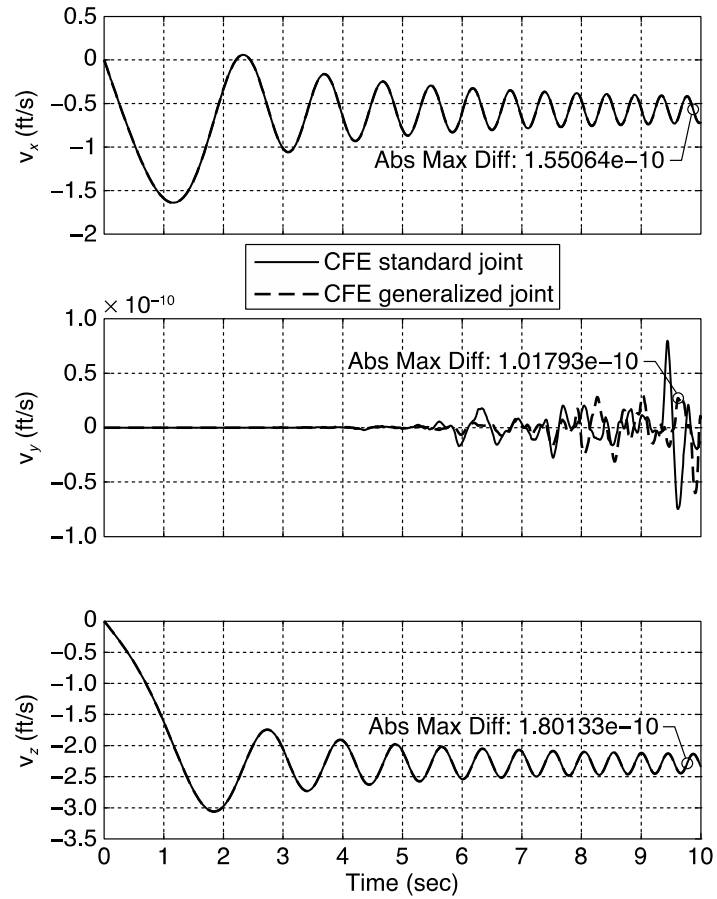
**Figure 81. Cylinder inertial velocity comparison between POST2/CFE standard planar joint and generalized joint.**
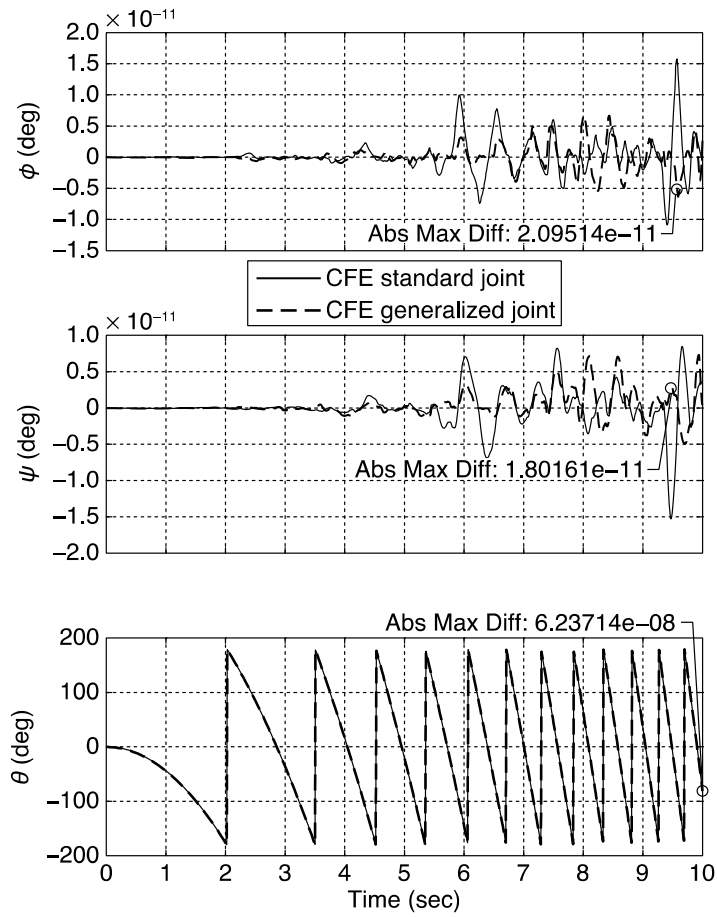
Figure 82. Cylinder Euler angle (1-3-2 sequence) comparison between POST2/CFE standard planar joint and generalized joint.
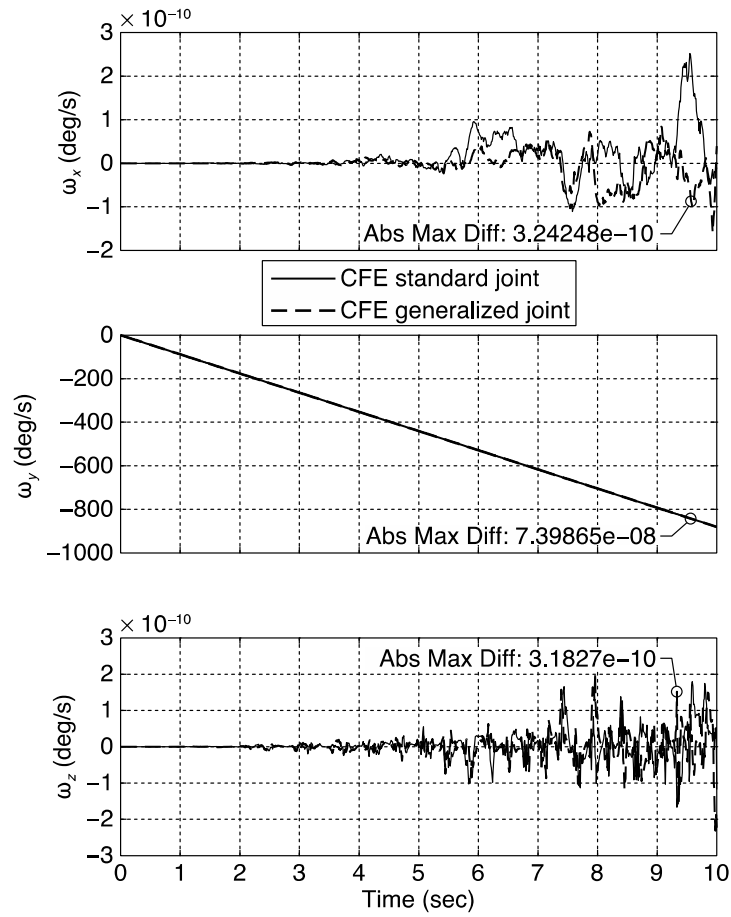
Figure 83.   Cylinder body axis angular velocity comparison between POST2/CFE standard planar joint and generalized joint.
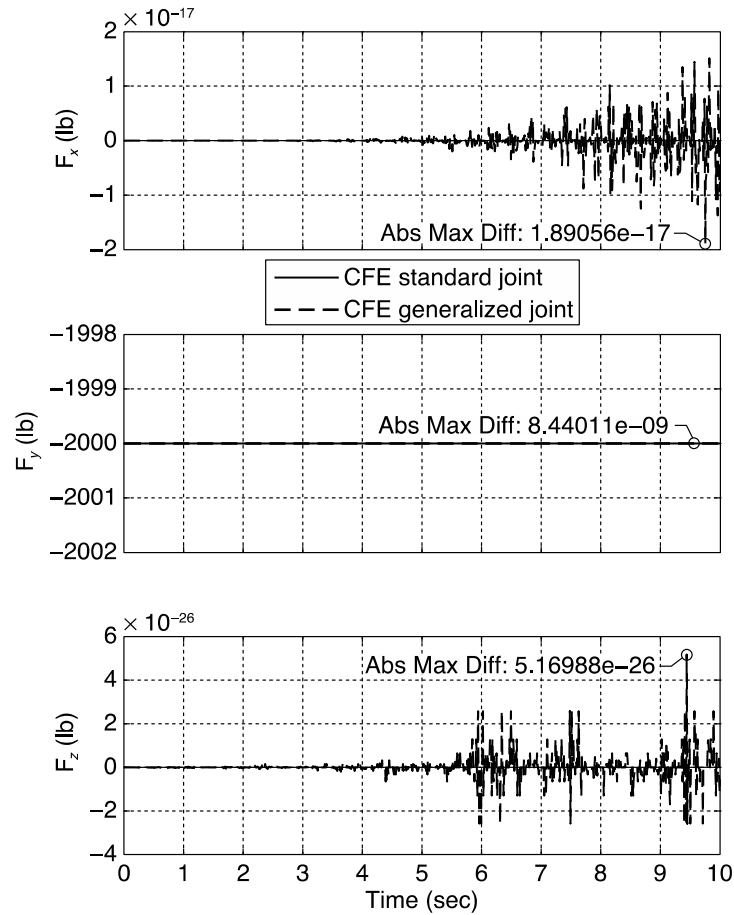
**Figure 84. Constraint force comparison between
POST2/CFE standard planar joint and generalized joint.**
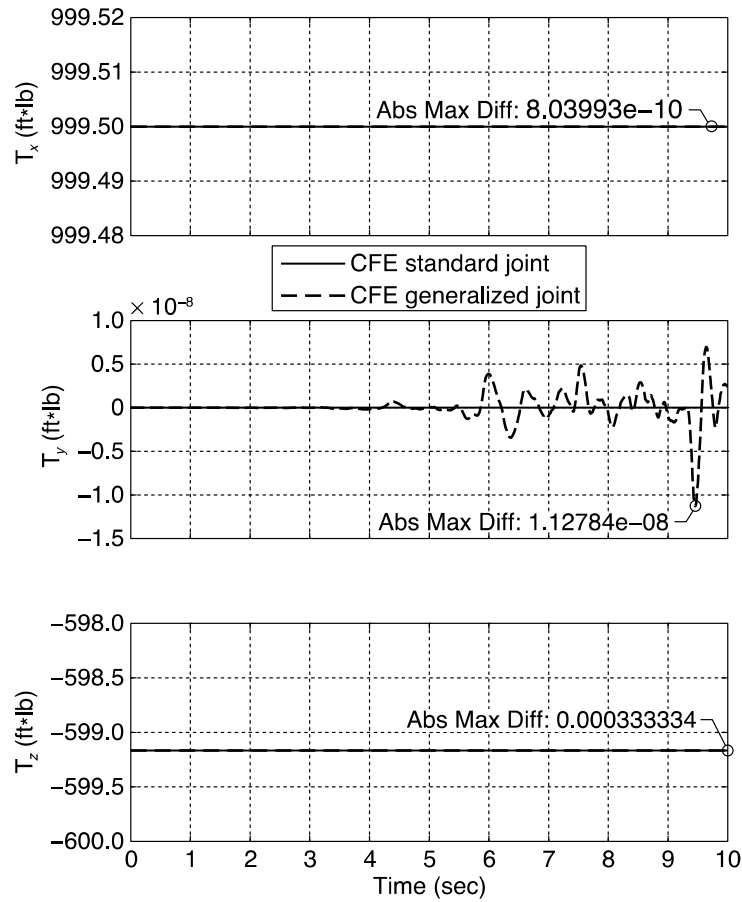
**Figure 85. Constraint torque comparison between POST2/CFE standard planar joint and generalized joint.**
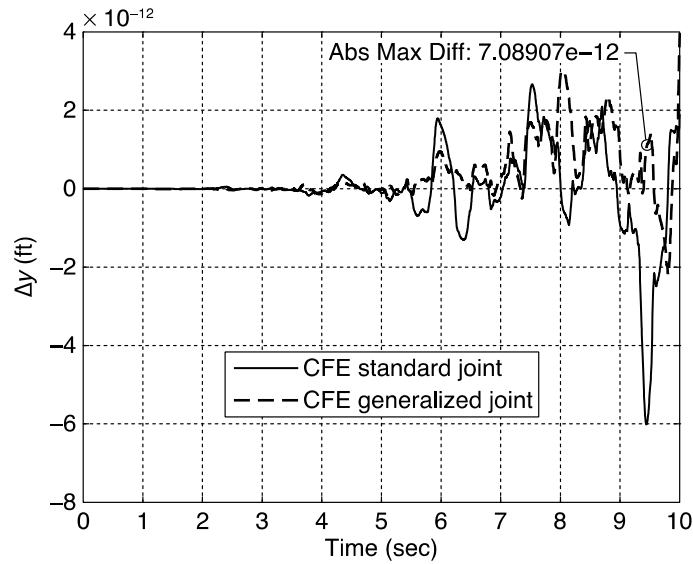
Figure 86. Comparison of relative joint separation between the cylinder and table connection points, represented in inertial frame components, for POST2/CFE standard planar joint and generalized joint.
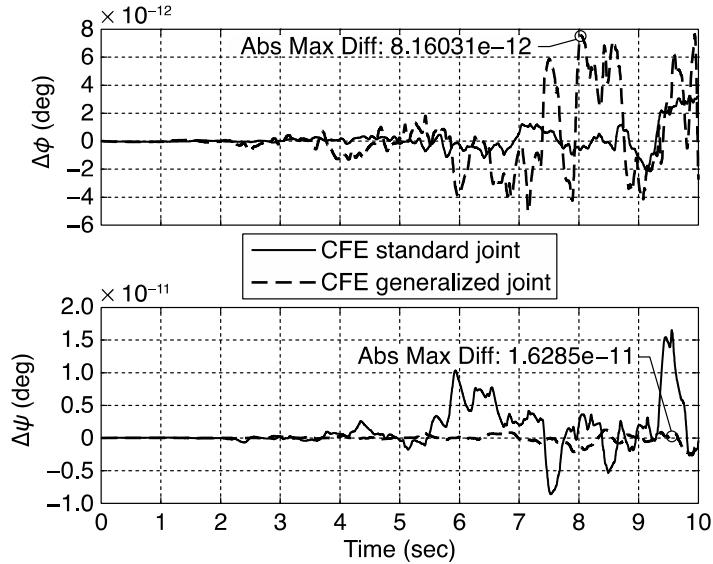

Figure 87. Comparison of relative joint orientation error between the joint connections of the table and cylinder for POST2/CFE standard planar joint and generalized joint.

Section 4. Application of POST2/CFE for Launch Vehicle Stage Separation

This section discusses the application of the POST2/CFE for launch vehicle stage separation. The three cases discussed are (i) the Space Shuttle Solid Rocket Booster (SRB) separation from Orbiter-External Tank (OET) and a comparison of the results with available STS-1 flight test data, (ii) the Hyper X Research Vehicle separation from the Pegasus Booster and a comparison of the results with available flight test data, and (iii) the end-to-end simulation for a bimese TSTO launch vehicle concept from lift-off to orbit insertion or first stage reentry including stage separation dynamics.

4.1   Space Shuttle SRB Separation

The Space Shuttle is designed to launch a variety of payloads into (and/or retrieve from) Earth's orbit. The Shuttle can deliver up to 55,000 lb of cargo to low Earth orbit.. The Shuttle launch configuration consists of the OET and the two SRBs. Figure 88 shows a schematic arrangement of the launch configuration.
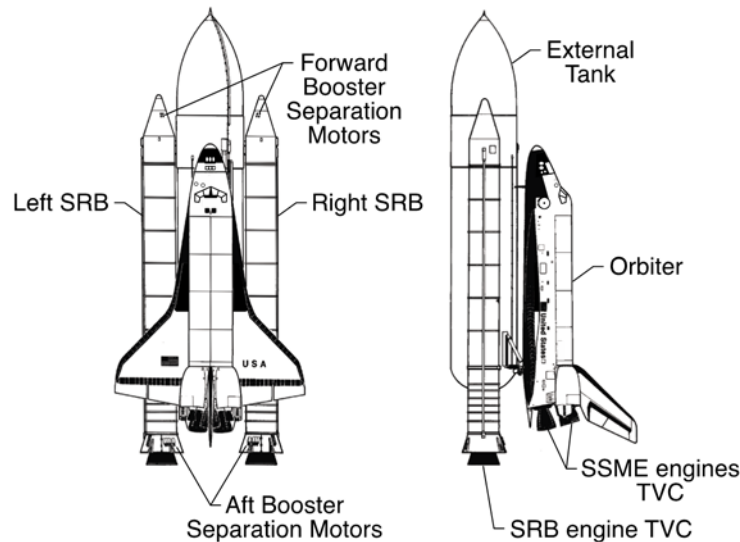
Figure 88.   Space Shuttle vehicle configuration.

The burn time of the SRBs is approximately two minutes. At burn out, the left and right SRBs separate simultaneously. The nominal staging of SRBs occurs from 150,000 ft to 180,000 ft altitude and Mach 3.75 to 4.0. The SRB lateral and vertical separation is aided by a cluster of four booster separation motors (BSMs) located in the forward pods and another cluster of four BSMs on the aft skirts of each SRB. The BSMs provide lateral and normal acceleration of the SRBs away from the OET. The relative axial acceleration is achieved by the thrust from the Space Shuttle main engines (SSMEs). After separation, the SRBs are decelerated by parachutes during their descent for splash-down in the ocean, approximately 141 nautical miles from the launch site. The SRBs are recovered

and refurbished for reuse. Fig. 89 presents a schematic illustration of SRB separation, descent, and recovery.
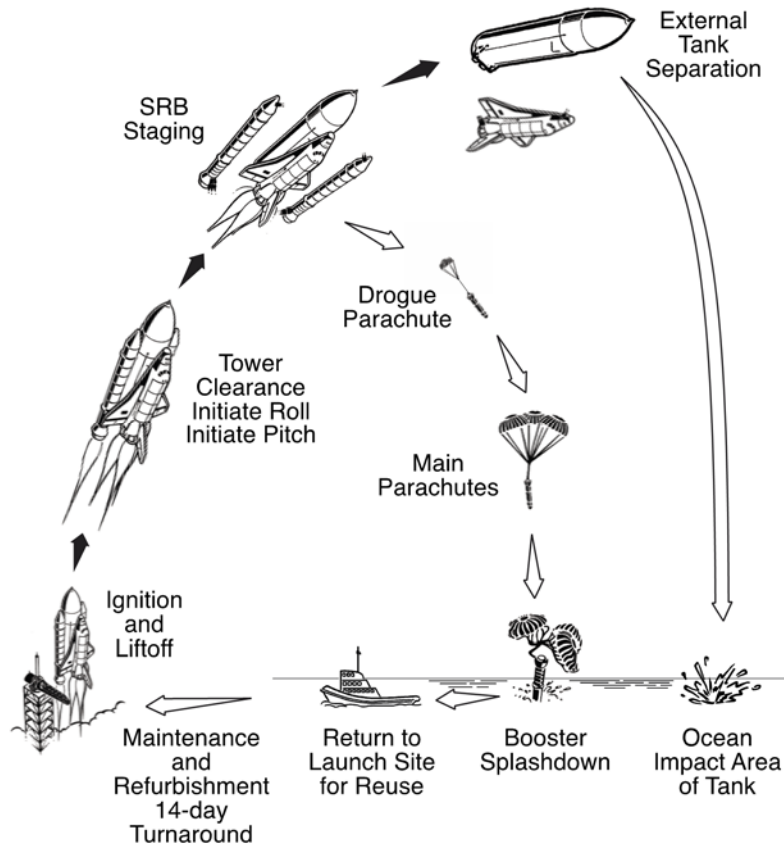
Figure 89. Schematic illustration of Space Shuttle staging events.

The SRBs are attached to the ET at one point on the forward end and at three points on the aft end (fig. 90). The forward attachment point is used to transfer the thrust loads from the SRB to the ET. The aft attachment points consist of three struts. At SRB separation, the bolts holding the forward and aft attachment points are severed, the aft joints are released, and the SRBs still connected to the OET are allowed to rotate about the forward joints up to a maximum of 1 deg prior to release. Upon release, the forward and aft BSMs on each SRB are fired simultaneously to move the SRBs away from the OET. The BSMs burn for 1.6 sec, with a peak duration of about 0.68 sec. The SRB separation is complex and is influenced by several factors. The OET cannot make a lateral maneuver to aid separation because an SRB is coming off each side. Consequently, for the duration of the separation event, the OET is flown in an attitude-hold mode. Because the Orbiter engines are above the OET center of gravity, they were canted upward for achieving moment balance (resultant thrust passing through the OET center of gravity) for attitude-hold mode. As a result, the OET moves downward and towards the SRBs. However, the BSMs' thrust is sufficiently large to move the SRBs away from the OET, resulting in a safe separation.
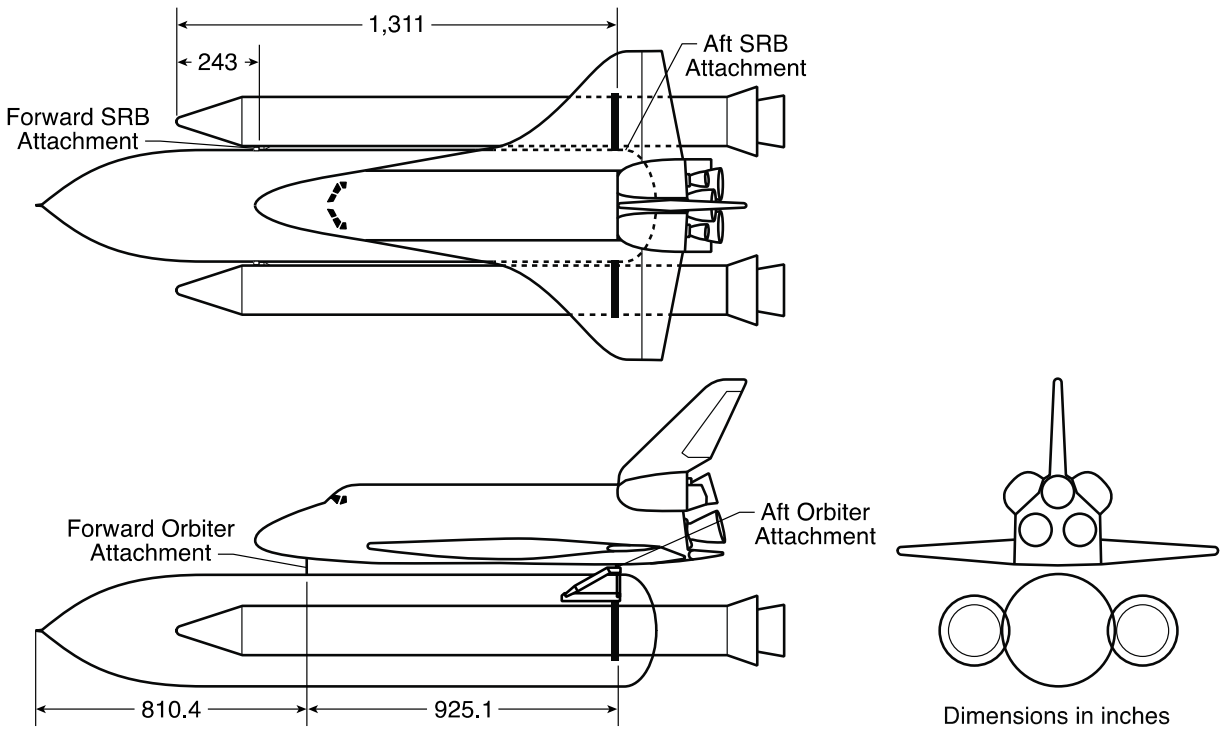
Figure 90.   Attachment of SRBs to OET.

Table 10 presents the STS-1 (Space Transportation System-1) flight parameters at SRB separation and table 11 shows simulation parameters. Figure 91 shows the definition of separation distances. ref. 31 presents complete details of the SRB separation simulations. Here, only the main results are presented to highlight the POST2/CFE capability to simulate multi-body separation in a launch vehicle staging scenario.

Table 10. STS-1 Flight Parameters at SRB Separation.

Parameter	Value
Altitude, ft	173,857
Velocity, ft/sec	4112.0
Mach Number	3.877
Dynamic Pressure, lb/ft^2	12.83
Angle of Attack, deg	3.0
Sideslip, deg	0.75
Flight Path Angle, deg	36.966
Body Roll Rate, deg/sec	−0.3
Body Pitch Rate, deg/sec	0.4
Body Yaw Rate, deg/sec	0
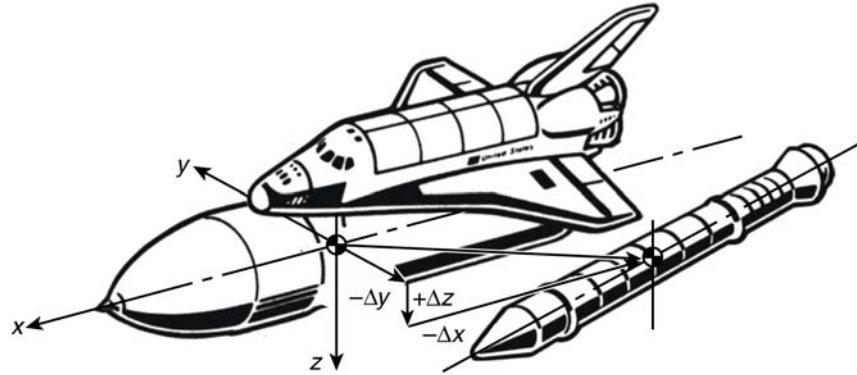
**Figure 91. Relative orientations and locations of
OET and SRBs during separation.**

Table 11. POST2/CFE Simulation Parameters.

Parameter	Value
Simulation time, sec	4.0
Integration step size, sec	0.001
Aft (fixed) joint release, sec	0.02
Front (revolute) joint release, deg	–0.104

Each aft joint was modeled as a fixed joint, released instantaneously, and each forward joint was modeled as a revolute joint permitting the SRBs to rotate with respect to the OET.

At t = 0.02 sec, the fixed aft joint was released allowing the SRBs to rotate about the top revolute joint. By trial and error, it was found that releasing the SRBs when the rotation angle reached –0.104 deg at about t = 0.02 sec, provided a good match with the trends of the STS-1 flight data. Using this criterion, the SRBs were released at t = 0.2 sec and the BSMs were activated.

For a comparison of POST2/CFE results along with STS-1 flight data and Shuttle vehicle dynamic simulation (SVDS) (ref. 31) data for various parameters are presented in figs. 92–98. However, not all the input data used in SVDS were available and engineering judgment was used to generate the missing input data. The input data uncertainty may be a factor contributing to the differences between SVDS results and POST2/CFE predictions.

The predicted POST2/CFE relative locations of the vehicles during separation are in good agreement with the flight data (fig. 92).
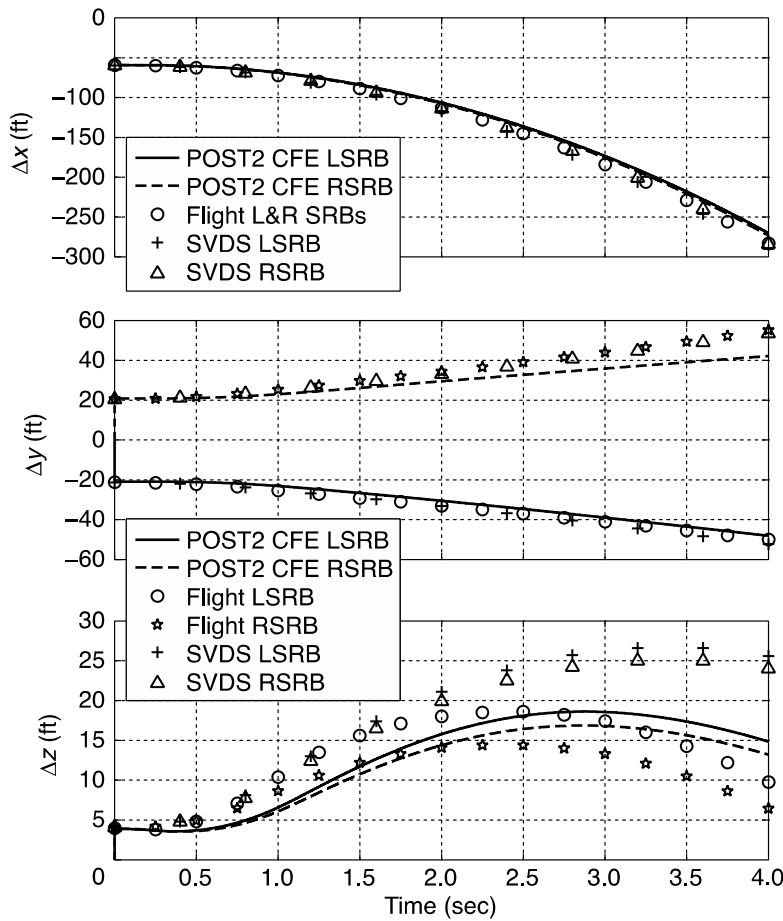
Figure 92. Variation of relative distances Δ*x*, Δ*y* and Δ*z* with time during SRB separation, STS-1.

The *x*, *y*, and *z* components of linear accelerations (in terms of gravitational acceleration G) for OET, left and right SRBs are shown in fig. 93–95. It may be observed that at *t* = 0.2 sec, when the joint is released, there is a steep rise in *x* and *z* components of OET acceleration because of a sudden decrease in the combined vehicle mass as a result of the SRB's release. Similarly, the *y* and *z* components of SRB accelerations show a steep rise at *t* = 0.2 sec when BSMs are turned on and a sharp drop at *t* = 1.0 sec when the BSM thrust starts falling off. The predicted linear accelerations for the OET and the SRBs are in fair agreement with the flight data.
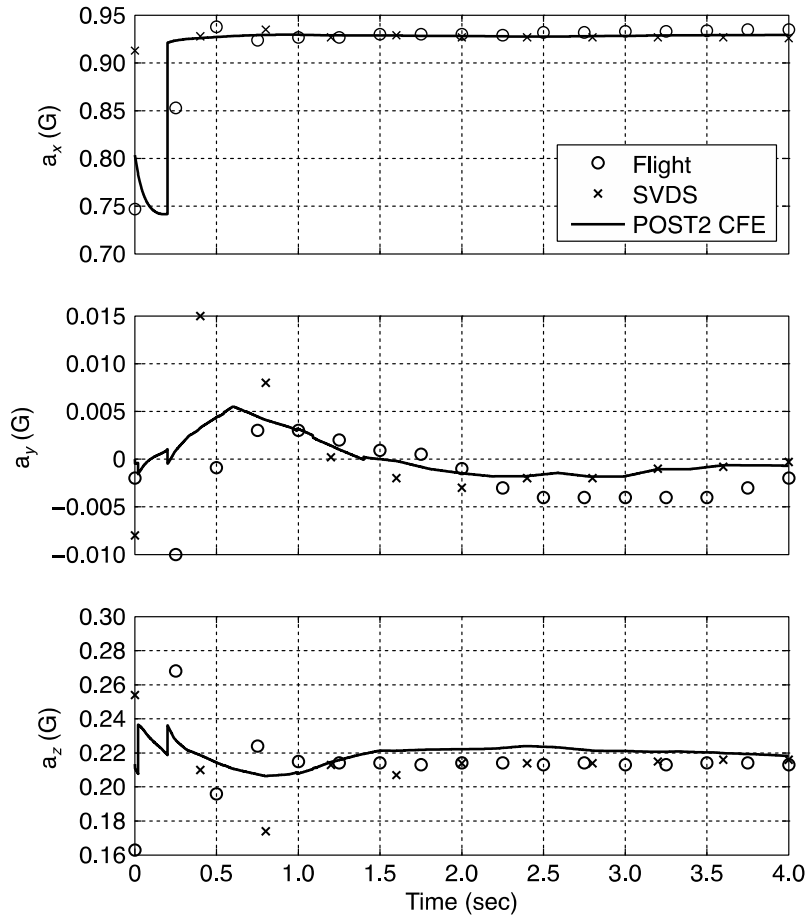
Figure 93. Variation of OET linear acceleration components (excluding gravity) during separation.
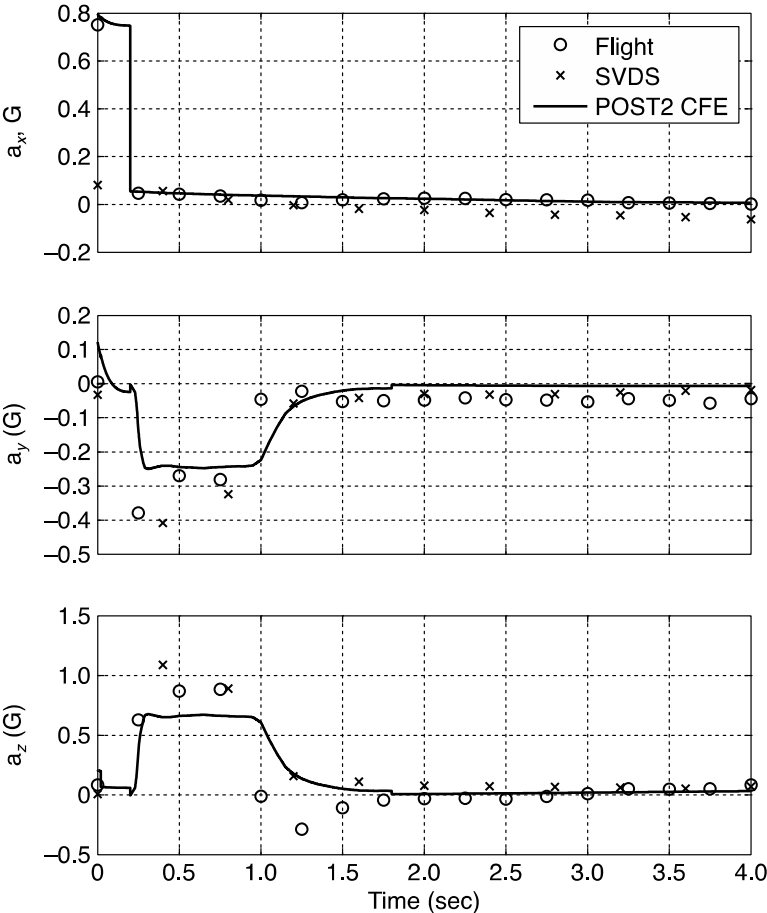
Figure 94. Variation of LSRB linear acceleration components (excluding gravity) during separation.
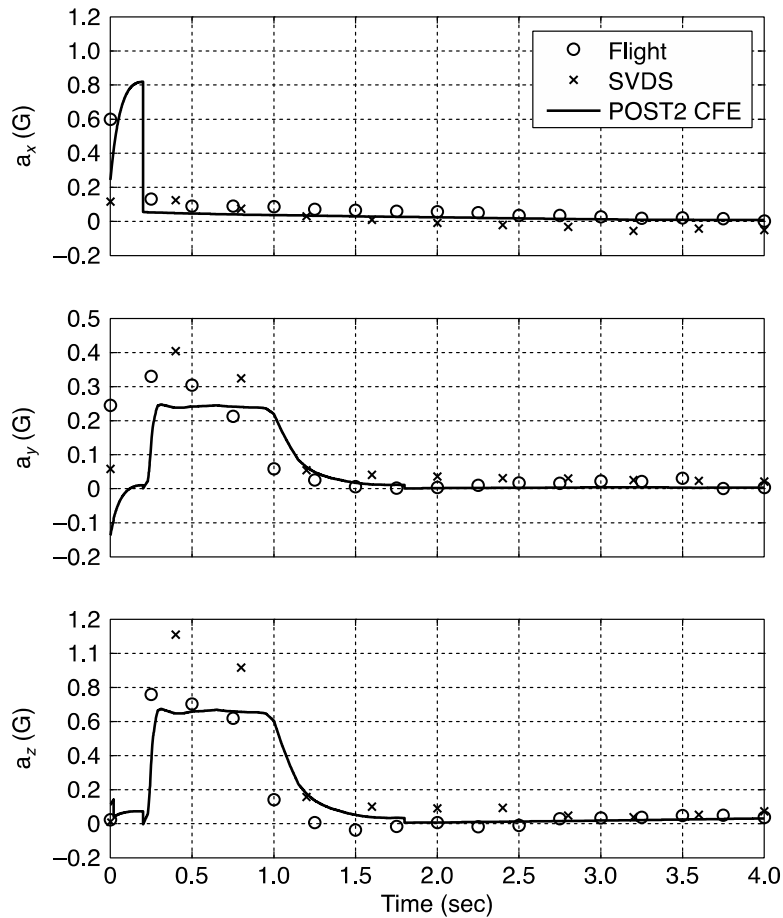
Figure 95. Variation of RSRB linear acceleration (excluding gravity) components during separation.

   The predicted components of the OET and the SRBs were noted to be very sensitive to assumed center-of-gravity locations. In view of this, the angular velocities are presented in fig. 96 for the nominal and two cases of OET center of gravity variation, with SRB centers of gravity at nominal locations. The x location of the OET center of gravity was held fixed while the y and z locations were varied within the uncertainty range estimated for STS-1. For example, the case "OET-Min SRB Nom" corresponds to OET y and z locations at their minimum value and SRB locations at their nominal value. These predictions based on center of gravity variations compared better with the STS-1 flight data for angular velocities in pitch and yaw compared to the nominal case. However, the angular velocity in roll is still outside the range of these predictions involving center of gravity variations.

   The predicted LSRB and RSRB angular velocity components are shown in figs. 97 and 98 for the nominal case and cases with different combinations of center of gravity variations. For the SRBs, the x location of the center of gravity was held at the nominal location, and the y and z locations were varied from the minimum to the maximum uncertainty bounds. The OET center of gravity was located at its nominal position. For example, the case "OET-Nom SRB-Ynom Zmax" corresponds to the OET center of gravity at the nominal location, the SRB y location at the nominal location and the z location at its maximum uncertainty bound. For the LSRB, these predictions involving center of gravity variations compare better with STS-1 flight data than the nominal case. However, for the

91

RSRB, the flight angular velocity in roll still differs significantly from current predictions. There was an anomaly in the RSRB sensor during STS-1, and its flight data is possibly in error (ref. 31). This anomaly is evident because the initial value of roll rate is –1.6 rad/sec instead of –0.3 rad/sec (see table 2). If the flight data were readjusted to cancel this initial offset, the current predictions would compare more favorably as can be observed in fig. 98. However, this readjustment of flight data was not attempted here.
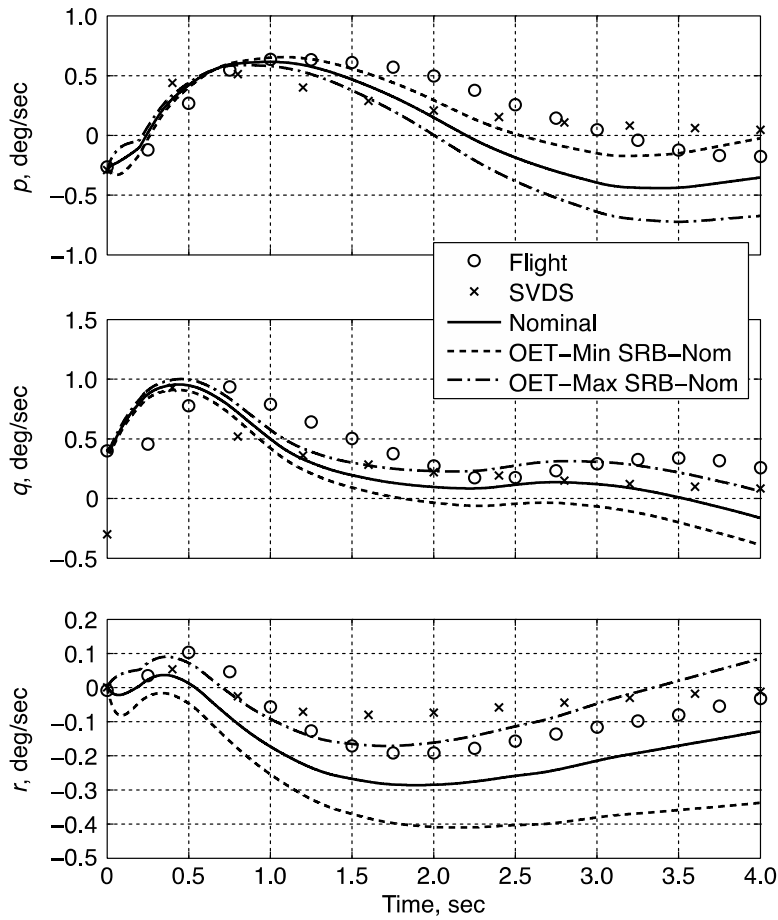
Figure 96. Variation OET of angular velocity components during separation, STS-1.
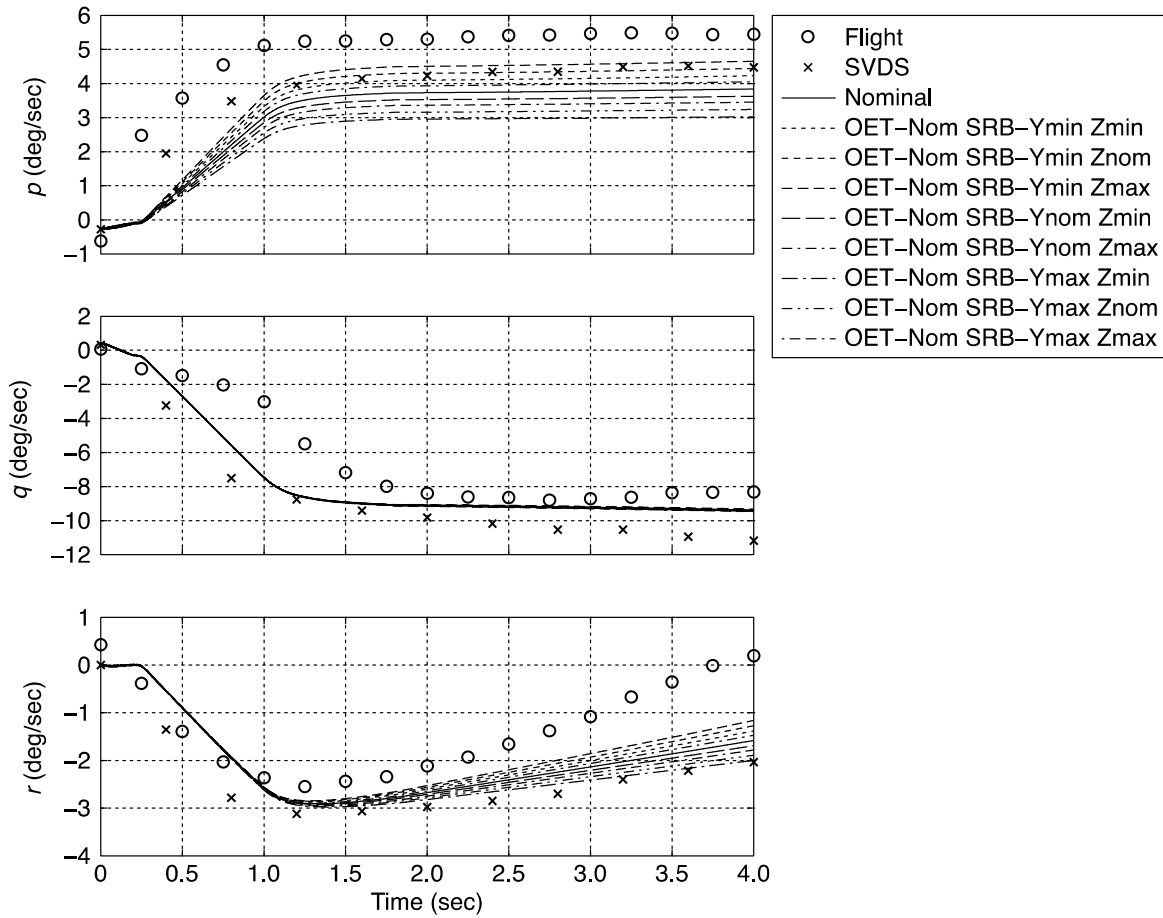
Figure 97. LSRB: Angular velocity components during separation, STS-1.
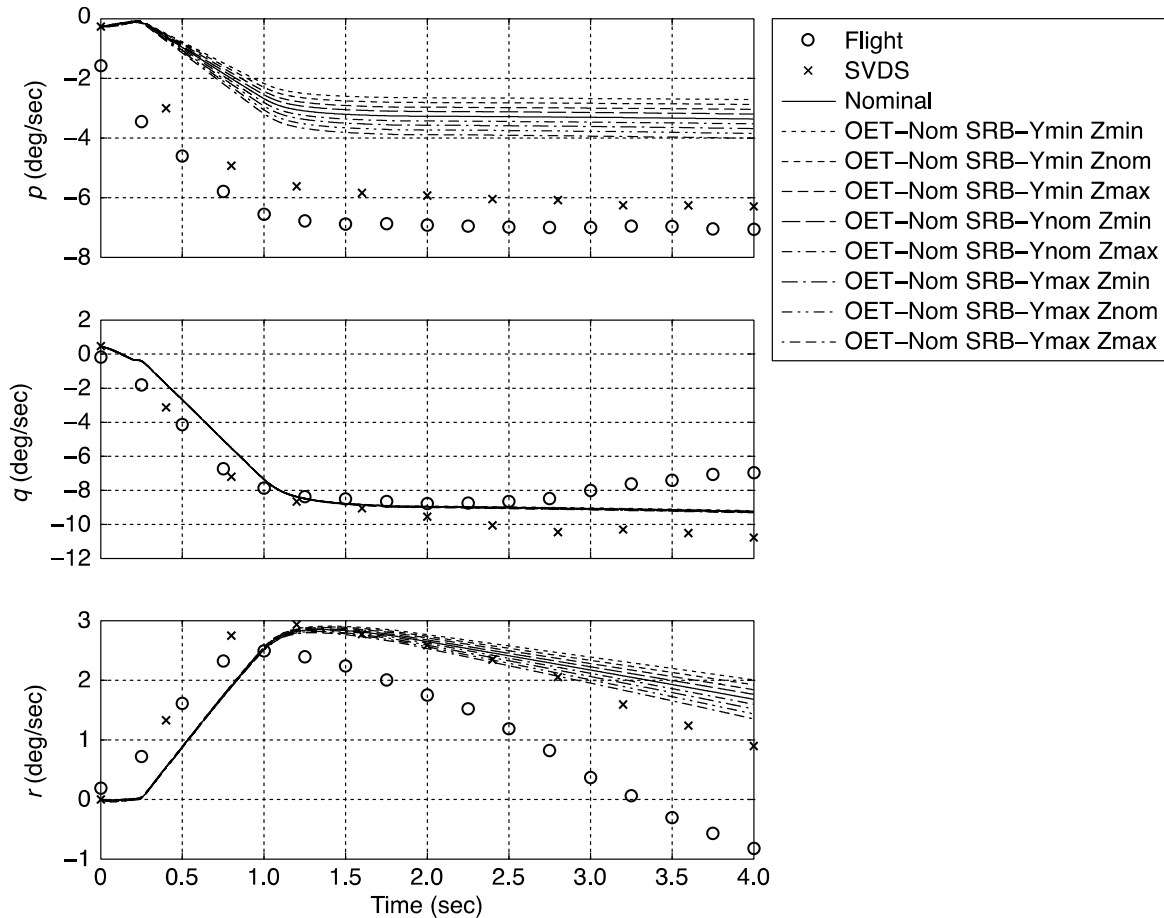
Figure 98. RSRB: Angular velocity components during separation, STS-1.

In general, the results of POST2/CFE simulation compared reasonably well with STS-1 flight data and the SVDS data. Some differences that exist may be the result of incorrect inputs to the POST2/CFE simulation because of unavailability of exact values of key input parameters like SSME initial cant angles. The results indicate that POST2/CFE is capable of satisfactorily predicting multi-body separation dynamics in launch vehicle staging scenario like the Space Shuttle SRB separation.

4.2 Hyper-X Stage Separation

This test case was selected to evaluate the capability of POST2/CFE to model and simulate another case of flight vehicle stage separation and compare results with flight data from NASA's X-43A hypersonic scramjet test vehicle (fig. 99). In 2004, NASA conducted two successful scramjet test flights of the X-43A research vehicle (RV) at speeds near Mach 7 and 10, respectively. The roughly 10 second scramjet test was performed after the RV was boosted to the target flight condition by the Hyper-X Launch Vehicle (HXLV). Figure 100 shows a dimensioned drawing of the mated RV and HXLV. Additional information describing the X-43A RV and HXLV may be found in ref. 32.

Figure 99.   Artistic rendering of X-43A (RV) separation from HXLV booster.
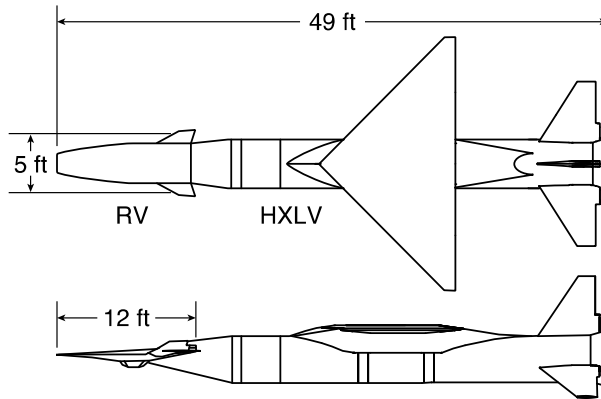
**Figure 100.   Dimensioned drawing of mated X-43A
Research Vehicle and Hyper-X Launch Vehicle.**
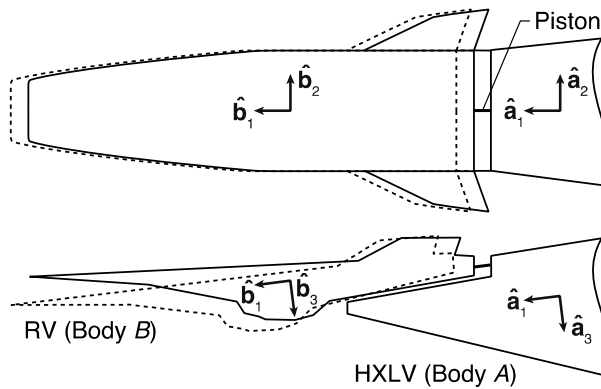
**Figure 101.   CFE modeling of piston contact
for X-43A separation problem.**

The X-43A stage separation event was initiated approximately three seconds after HXLV burnout at a dynamic pressure of 1000 psf. Separation began when two pyrotechnically actuated pistons extending from the booster pushed against the RV to induce ~16 ft/s of relative velocity between the two vehicles. The two pistons, which were positioned roughly 9 in on each side of the RV centerline, were initially in contact with a cup-like ball joint attached to the RV that permitted rotation about the piston contact point and translation only along the line of action of the piston force, which was oriented 4 deg below the horizontal. Both pistons were connected to the same gas chamber and were activated at the same time and remained in contact with the RV for ~0.1 sec until they reached the end of their nine-inch stroke length. Although the ball joint permitted rota-

tion in any direction at each individual piston contact point, the fact that both pistons were fired concurrently and were simultaneously in contact with the RV effectively excluded relative rolling and yawing rotation between the two separating vehicles.

Once the pistons reached the end of their nine-inch extensions, the RV separated from the HXLV. At this time, the HXLV commanded a nose-down pitching moment to move away from the RV, and the RV was steered to its required target condition.

This problem was set up using POST2/CFE to model the piston constraint forces. The two pistons were modeled as a single piston to avoid over-constraining the problem. Thus, a single piston was modeled as a sliding joint in series with a revolute joint; that is, relative translation was allowed in one direction (the piston line of action), and relative rotation was permitted only about the pitch axis. The piston was placed at the centerline of the RV, and the axial force that pushed the vehicles apart was doubled. Figure 101 shows a schematic highlighting these modeling details.

The unit vectors are defined in the HXLV such that $\hat{\mathbf{a}}_1$ is along the direction in which transla-tion or sliding is permitted (along the piston line of action), and $\hat{\mathbf{a}}_2$ indicates the direction in which rotation is free to occur (pitch axis). A similar set of unit vectors, $\widehat{\boldsymbol{b}}_r$, can be defined that are fixed in the RV and initially aligned with the unit vectors $\hat{\mathbf{a}}_r$ fixed in the HXLV. For this case, two con-straint equations with the form of Eq. (7) can be written as

$$\left(\mathbf{r}^{O\bar{B}} - \mathbf{r}^{O\bar{A}}\right) \cdot \hat{\mathbf{a}}_r = 0 \quad (r = 2, 3) \tag{121}$$

Note that $\hat{\mathbf{a}}_2$ and $\hat{\mathbf{a}}_3$ are substituted for $\mathbf{e}_A$. In addition, two constraint equations describing the restriction imposed on relative orientation are formed:

$$\hat{\mathbf{b}}_1 \cdot \hat{\mathbf{a}}_2 = 0, \ \hat{\mathbf{b}}_3 \cdot \hat{\mathbf{a}}_2 = 0 \tag{122}$$

With the assumption that the joint is frictionless, the constraint force and moment in the direc-tions where motion is permitted become (using Eq. (18) and (19))

$$\mathbf{F}_B^{(\text{CON})} \cdot \hat{\mathbf{a}}_1 = 0, \ \mathbf{T}_B^{(\text{CON})} \cdot \hat{\mathbf{a}}_2 = 0 \tag{123}$$

The results are compared with available X-43A flight data and previously published X-43A pre-flight simulation (ref. 32), which was also developed using POST2, but each joint between the pistons and the RV was modeled as a massless spring with a prescribed force profile in the direc-tion along the piston centerline. The spring restoring forces were computed from beam deflection theory in the lateral directions perpendicular to the axis of piston motion. Reference 32 details the development of this preflight POST2 spring model simulation. The primary difference in problem setup between the two approaches is in the modeling of the pistons, where POST2/CFE models only one piston to avoid over-constraining the problem, the spring model implementation models both pistons.

As a measure of how well the joint constraint was satisfied, fig. 102 shows the relative joint dis-placement between the two separating vehicles. This parameter is the distance from the RV joint location to the HXLV joint location and was computed in the piston axial (line of action, $\hat{\mathbf{a}}_1$), lateral ($\hat{\mathbf{a}}_2$), and normal ($\hat{\mathbf{a}}_3$) directions. The results indicate that CFE does a better job of enforcing the translational constraint than the spring model, and there is virtually no joint displacement in the lateral or normal directions. Similar results are seen in fig. 103 for the relative difference in attitude between the two vehicles. Again, CFE does an excellent job of enforcing the rotational constraint, essentially eliminating any relative roll and yaw between the RV and HXLV. Figures 104 and 105,

respectively, show the constraint forces and moments about the vehicle center of mass. In these plots, the forces and moments computed by the spring model include the contributions of both pistons. The results show that both the spring model and POST2/CFE compute very similar forces and moments. However, the spring model results are oscillatory in nature since the joint constraint is not satisfied exactly.
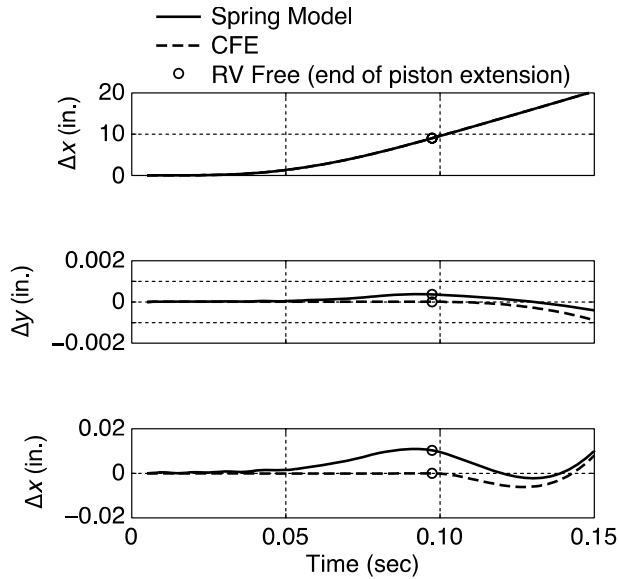
Figure 102. Comparison of joint displacement in x, y, and z directions for CFE and spring model.
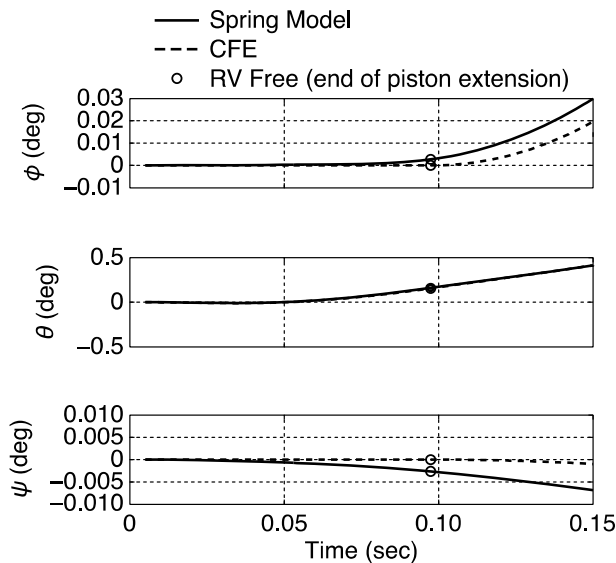
Figure 103. Comparison of relative angular displacement between POST2/CFE and spring model.
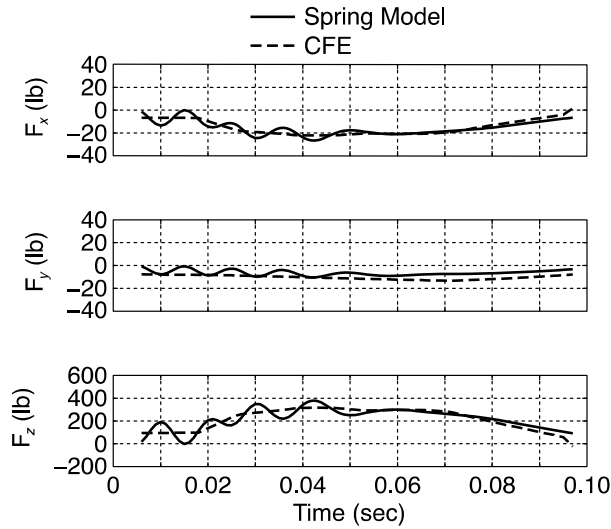
Figure 104. Comparison of constraint forces computed by POST2/CFE and spring model.
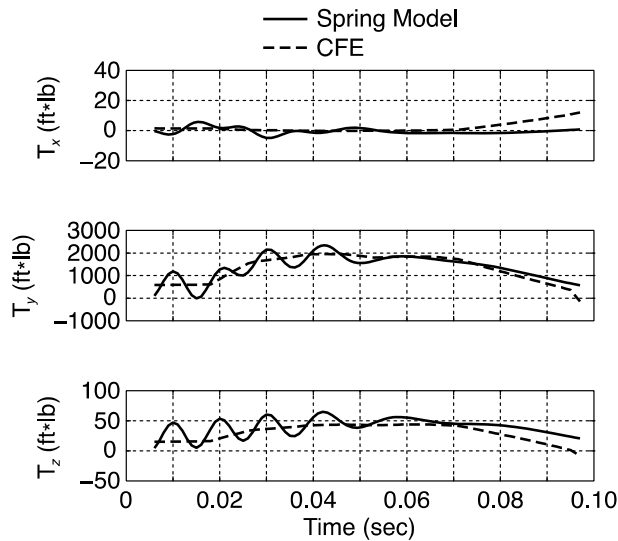
Figure 105. Comparison of constraint (torques) computed by POST2/CFE and spring model.

Figure 106 shows comparisons of the angle of attack and angle of sideslip profiles. Both the spring model and POST2/CFE results for angle of attack match well with flight data. However, there are larger differences in the sideslip response. In addition, both techniques match the observed flight data well. It should be noted that the degree to which the simulation results match the flight data depends on other factors besides CFE modeling, such as aerodynamic force and moments, winds, accuracy of flight data instrumentation, etc. Aerodynamic modeling was especially critical because separation occurred at a dynamic pressure of 1000 psf.
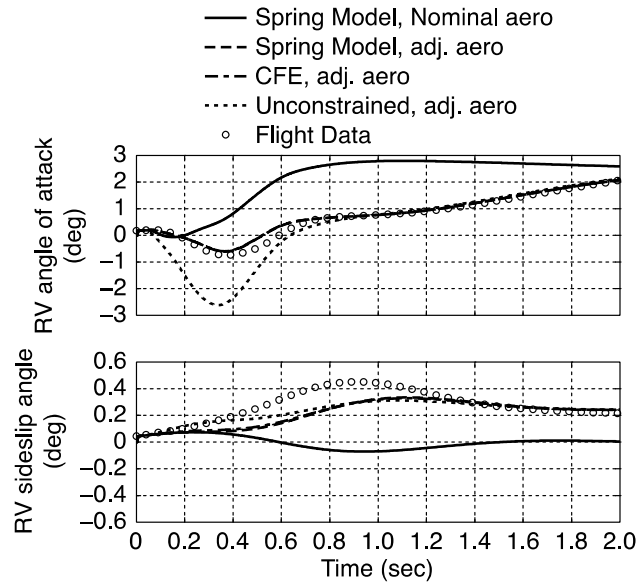
**Figure 106. Simulation versus flight data comparison
of angle of attack and angle of sideslip profiles.**

To illustrate the sensitivity of the simulation results to aerodynamic modeling, computations were made using the nominal (preflight) aerodynamic database and a post-flight reconstructed aerodynamic database in which the uncertainty terms had been adjusted to match the flight data more closely. The variations in angle of attack and sideslip differ significantly depending on which aerodynamic model was used. Note that all POST2/CFE results were generated using the adjusted aerodynamics.

As a further comparison, fig. 106 shows results for an unconstrained case where no constraint forces were applied to model the joint (but the piston axial force that pushed the vehicles apart was still modeled). During the first one second of separation, the unconstrained results differed significantly from the cases that included the constraint, demonstrating the importance of accurate modeling of the piston joint. Even though the differences between the constrained and unconstrained angle of attack and sideslip profiles disappeared after the control system became active and was able to compensate, it is important to capture the dynamics during the first second of flight since during that period the risk of re-contact was highest.

Figure 107 shows similar comparisons for the linear accelerations. The vertical (i.e., Body z direction) acceleration results were the most sensitive to the way in which the piston constraint was modeled and were also the most important for assessing the risk of re-contact. Again, the spring model and CFE results were nearly identical and provided a good match to the flight data. The differences between the constrained and unconstrained cases were actually larger than the differences because of aerodynamics.
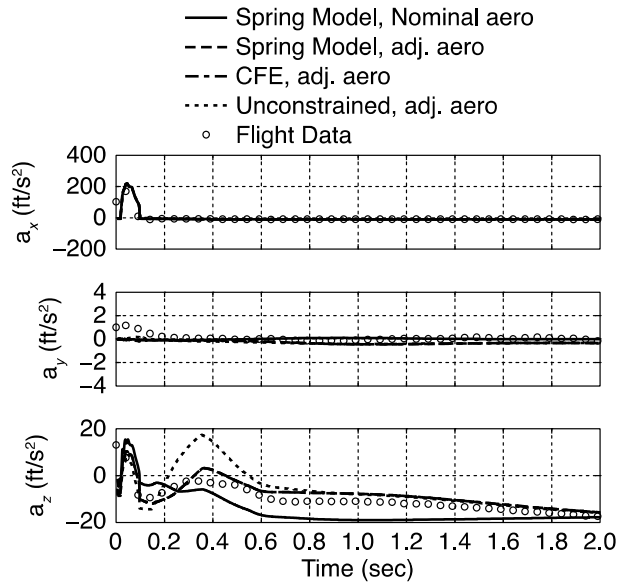
Figure 107. Simulation versus flight data comparison of *x*, *y*, and *z* accelerations in the local body frame.

Figure 108 compares the angular velocity results with the flight data. Once again there is excellent agreement between the spring model and CFE simulation results. Both simulations match the pitch rate flight data very well and do a much better job at predicting the pitching motion than the unconstrained case. The comparison between simulation and flight for yaw rate and roll rate is not as good. Much of the difference can be attributed to inadequate lateral-directional aerodynamic modeling as is evident in the large difference in results between the cases with nominal aerodynamics and adjusted aerodynamics.
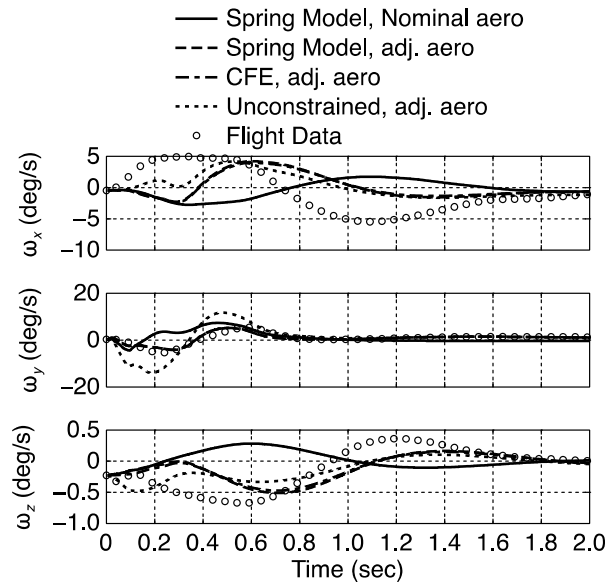
Figure 108. Hyper-X simulation versus flight data comparison of body roll, pitch, and yaw rate profiles.

4.3   End-To-End Simulation of Bimese TSTO Vehicle

Typically, the ascent trajectories are three DOF trajectories, while stage separation, which is usually a six DOF simulation, is not part of ascent trajectories and is simulated separately, and most of the times, using different simulation software. In this scenario, there is a two-way handoff, first from ascent part to set initial condition for separation, and then from separation to ascent of the upper stage or booster return. The challenge is to ensure that both of these handoffs are smooth, compatible and seamless without errors. The end-to-end simulation with stage separation as integral part eliminates the possibility of handoff errors. However, there is the challenge to merge the three DOF ascent simulation with the six DOF separation simulation. The objective of this exercise is to demonstrate the capability of POST2/CFE to handle this challenge and simulate a complete end-to-end mission, including stage separation dynamics.

The vehicle configuration selected for this exercise is the NASA Langley in-house TSTO Langley Glide Back Booster (LGBB) bimese configuration, consisting of a reusable booster and orbiter with the same outer mold line (fig. 109). Complete details of the bimese vehicles and end-to-end simulation are presented in ref. 33. Here, only the main results are presented.
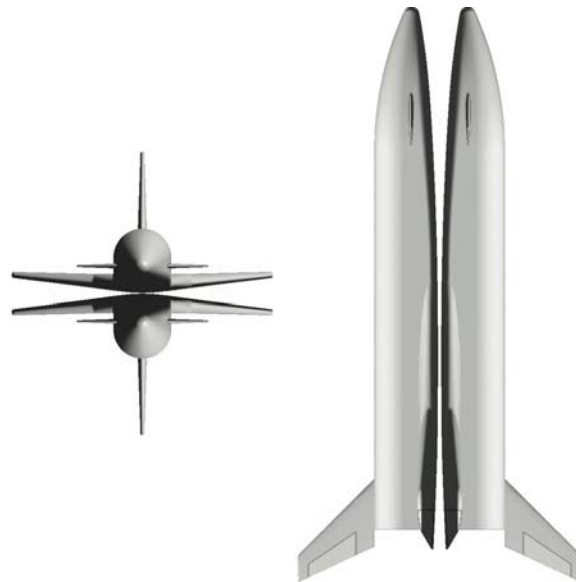
Figure 109. Schematic of the bimese booster and orbiter configuration.

Figure 110 shows the schematic diagram of the attachment of the orbiter to the booster. The booster is attached to the orbiter at two points. The forward joint is a fixed support and the aft joint is designed to permit rotation in pitch. At separation, the orbiter is operating at full thrust and the booster at no thrust.

Figure 111 shows the bimese flight profile to a low earth orbit mission. The launch vehicle stack is vertically launched and ascends up to the staging using the fuel in the booster. The staging occurs when the booster fuel is exhausted. After separation, the booster returns unpowered to a runway landing near the launch site, while the orbiter continues its assent up to low earth orbit. Table 12 gives flight parameters at staging.
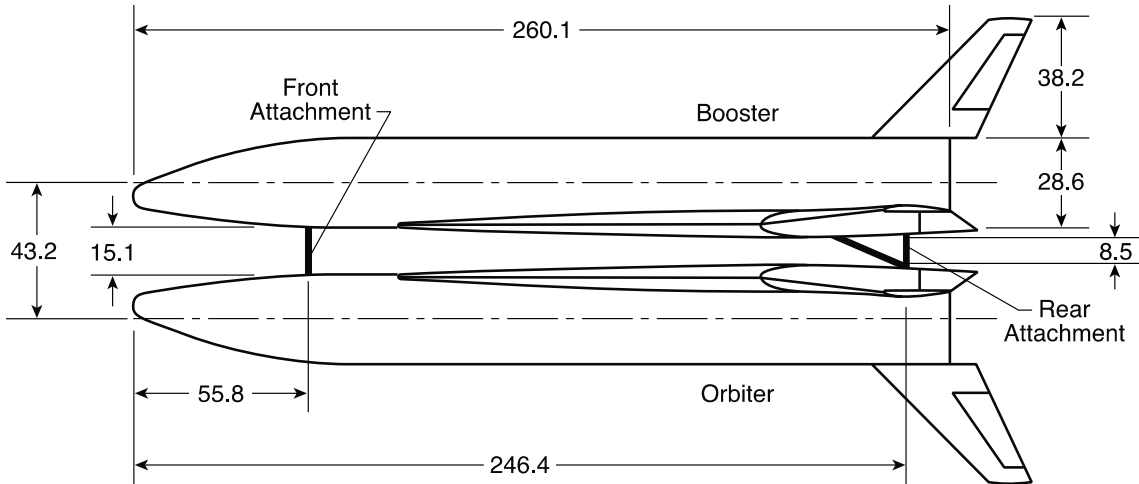
Figure 110. Booster and orbiter dimensions and attachments (dimensions in feet).
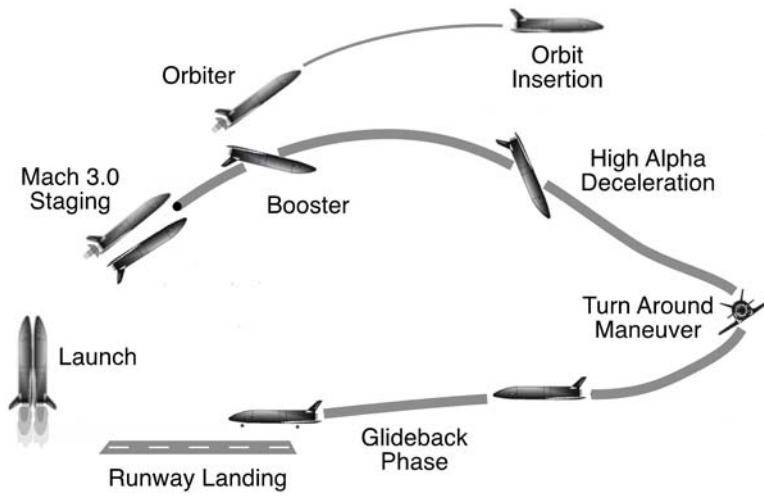
Figure 111. Flight profile for the bimese configuration.

Table 12. Flight Parameters at Staging.

Mach	3.79
Altitude, ft	93,975
Latitude, deg	28.57 N
Longitude, deg	79.76 W
Relative velocity, ft/sec	3741
Relative flight path angle, deg	34.57
Angle of attack, deg	0
Dynamic pressure, psf	308.0

To simplify modeling within POST2, the orbiter and booster stack were initially modeled as a single vehicle stack with two LOX-H2 rocket engines operating from liftoff until staging. After liftoff, the vehicle stack was controlled using pitch angles until five seconds before separation, at which point, the vehicle stack was guided using aerodynamic angles to adjust the angle of attack to zero at separation. The booster and orbiter were then modeled as two separate vehicles prior to separation with the booster positioned belly-to-belly (180 degrees in roll) relative to the orbiter.

To begin with, the rear attachment between the vehicles (fig. 110) was assumed to be a fixed joint. At staging, the front attachment was released and the rear attachment was changed to a revolute joint free to rotate in the pitch plane. Once the relative pitch between the vehicles reached 1.0 degree, the rotational joint was released, and the vehicles were set free to move apart in response to aerodynamic forces and thrust from the orbiter engine.

The simulation was three DOF from launch to staging, six DOF during separation, three DOF again post separation. Once the axial separation distance between the vehicles exceeded 2.1 vehicle lengths, staging was assumed to be complete, and the orbiter was then guided to a 50 nmi altitude (303,800 ft) with an inclination of 51.6 deg using pitch angle guidance. Once the specified orbital velocity was reached (25,855ft/sec), the orbiter engine was turned off, and the orbiter portion of the simulation was terminated. Meanwhile, the unpowered booster was guided back to the launch site using bank angle and angle of attack control. The landing target was the longitude and latitude of the launch site. The simulation was terminated when the booster was within 1 mile of the launch site with an altitude margin of about 1000 ft. The alignment with the runway and landing were not simulated.

Figures 112 and 113 show altitude and velocity as a function of time for the overall mission.
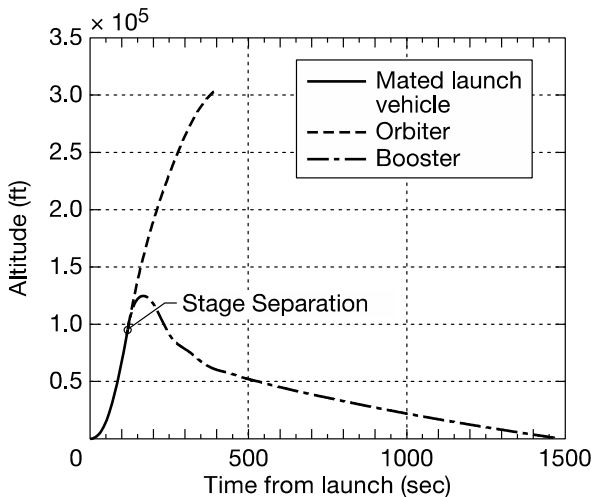
Figure 112. Velocity profile for the complete mission.
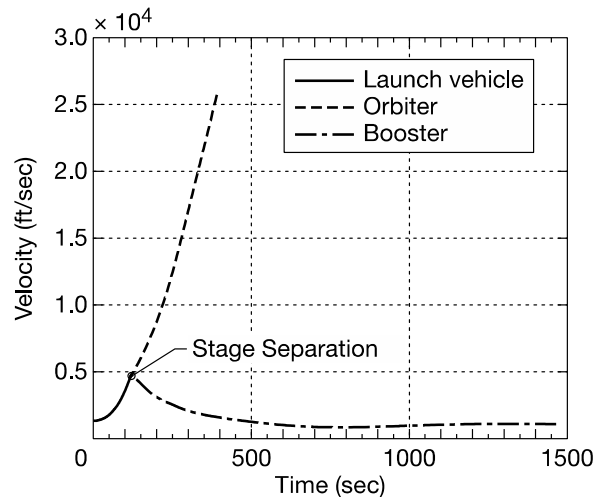
Figure 113. Altitude profile for the complete mission.

The staging occurs around $t = 119$ sec. and lasts for about five sec. The vehicles separated once the relative pitch between vehicles reached 1.0 deg. Separation distance between the booster and orbiter is presented in fig. 114 in terms of axial and normal distances, $\Delta x/L_{ref}$ and $\Delta z/L_{ref}$, where L_{ref} is the vehicle length of 260.1 ft. Figure 115 shows the angle of attack variations for the booster and orbiter during separation phase.
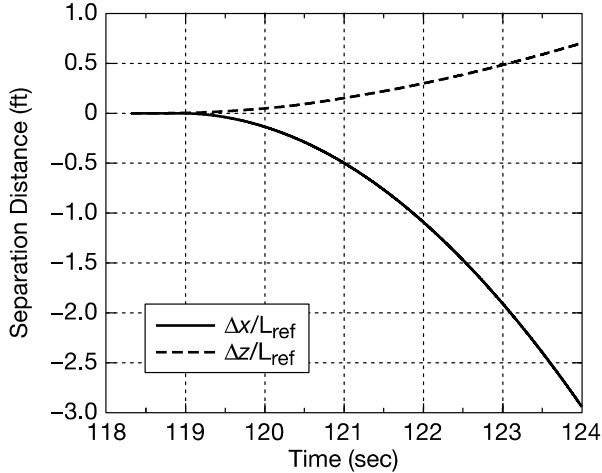
Figure 114. Relative separation distances between orbiter and booster.
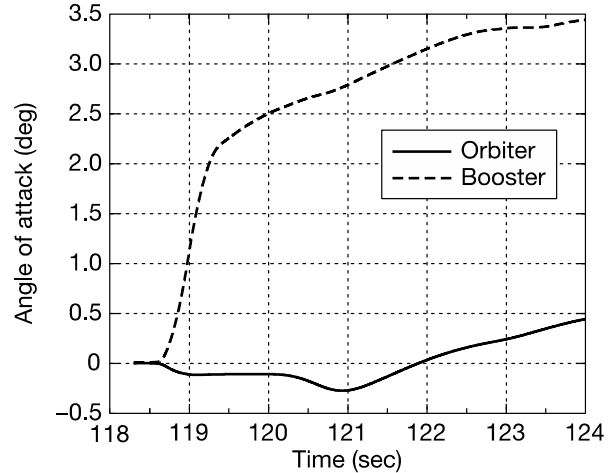
Figure 115. Angle-of-attack variation during separation.

To further evaluate POST2/CFE separation results, a separate, isolated stage separation case was run with the same conditions as in ref. 14 and compared with the results obtained using ConSep/ADAMS®. The separation distance between the orbiter and booster is in terms of $\Delta x/L_{ref}$ and $\Delta z/L_{ref}$ over a six second period after initiation of the separation event. The POST2/CFE separation distance (fig. 116) is in excellent agreement with ConSep/ADAMS®. Figures 117 and 118 show the angle of attack and the pitch rate, respectively, of the orbiter and booster obtained from POST2/CFE and ConSep/ADAMS®. Again excellent agreement between the two methods is observed. This exercise provides confidence that POST2/CFE correctly simulated the separation dynamics in the complete, end-to-end bimese mission.
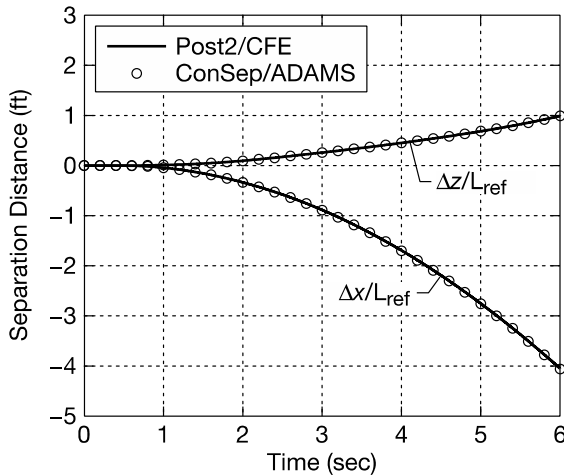

Figure 116. Comparison of separation distances between orbiter and booster.
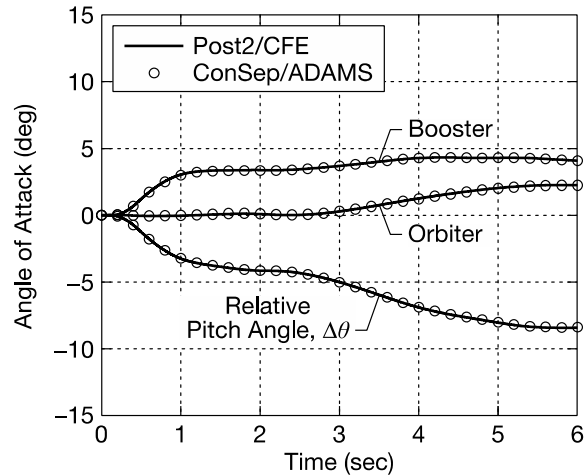
Figure 117. Comparison of booster and orbiter angles of attack during separation.
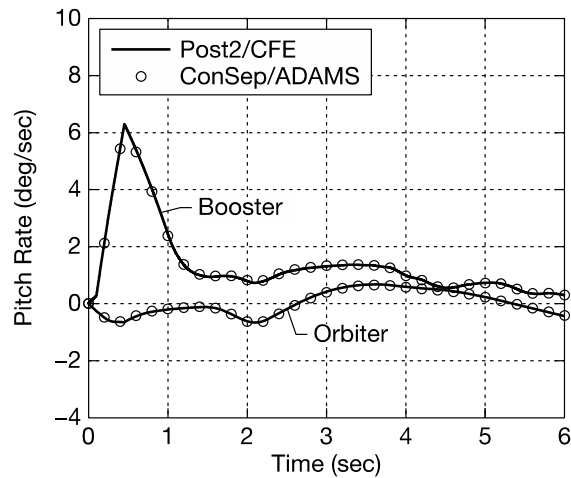
**Figure 118. Comparison of booster and
orbiter pitch rates during separation.**

After separation, the booster descended unpowered back to the runway. The booster was guided using angle of attack and bank angle as control variables, to a target of 28.5 deg N latitude and 80.0 deg W longitude, ±0.0145 deg. (or ±1 mile) at an altitude of 1000 ft. The runway landing was not simulated in this study.

Section 5. Summary and Concluding Remarks

The CFE methodology provides a framework for modeling constraint forces and moments acting at joints that connect multiple vehicles. Several stand-alone test cases involving various types of simple joints were developed to validate the CFE methodology and comparisons were made with those predicted using industry standard benchmark software like ADAMS® and Autolev. The CFE results were in excellent agreement with ADAMS® or Autolev. Then, the CFE methodology was implemented in POST2. With implementation in POST2, the CFE provides a capability to simulate stage separation dynamics of launch vehicles as well as end-to-end trajectories of launch vehicles including stage separation. The POST2/CFE simulation methodology was applied to the STS-1 Space Shuttle SRB separation and X-43A RV separation from Pegasus launch vehicle as a further test and validation for POST2/CFE for launch vehicle stage separation. The results are in fair agreement with corresponding flight data. The POST2/CFE was applied for end-to-end simulation of the bimese TSTO concept and the results of stage separation for this bimese vehicle compared well with previous ConSep/ADAMS results. All these comparison data demonstrate that POST2/CFE software can be used for performing stage separation analysis.

References

1. Dillenius, M. F. E., Perkins, S. C., and Nixon, D., Pylon Carriage and Separation of Stores, AIAA Progress in Astronautics and Aeronautics: Tactical Missile Aerodynamics—General Topics, M. J. Hemsch, ed., Vol. 141, 1992.

2. Taylor, R. T. and Alford, W. J., Jr., A wind tunnel investigation of the carry loads and mutual interference effects of 1/40-scale models of the X-15 and B-52 airplanes in combination, NASA TM X–184, December 1959.

3. Hurley, M. J., "Digital Program P5255, A Six-Degree, Multiple Body Separation Simulation for Hinged and/or Linked Lifting Entry Vehicles," Vols. 1 and 2, GDC–ERR–1377, December 1969, Convair Aerospace Division of General Dynamics, San Diego, CA.

4. Hurley, M. J., Carrie, G. W., "Stage Separation of Parallel-Staged Shuttle Vehicles: A Capability Assessment," *Journal of Spacecraft*, Vol. 9, No. 10, October 1972, pp. 764–771.

5. Decker, J. P. and Wilhite, A.W., "Technology and Methodology of Separating Two Similar Size Aerospace Vehicles Within the Atmosphere," AIAA Paper 1975–29.

6. Decker, J. P., Experimental Aerodynamics and Analysis of the Stage Separation of Reusable Launch Vehicles, NASA–SP–148, January 1967.

7. Decker, J. P. and Gera, J., An Exploratory Study of Parallel-Stage Separation of Reusable Launch Vehicles, NASA TN D–4765, October 1968.

8. Decker, J. P., Aerodynamic Interference Effects Caused by Parallel-Staged Simple Aerodynamic Configuration at Mach Numbers of 3 and 6, NASA TN D–5379, Aug. 1969.

9. Wilhite, A. W., Analysis of Separation of the Space Shuttle Orbiter from a Large Transport Airplane, NASA TM X–3492, June 1977.

10. Naftel, J. C. and Wilhite, A. W., "Analysis of Separation of a Two-Stage Winged Launch Vehicle," AIAA Paper 86–0195.

11. Naftel, J. C. and Powell, R. W., "Aerodynamic Separation and Glideback of a Mach 3 Staged Orbiter," AIAA Paper 90–0223.

12. Naftel, J. C., and Powell, R. W., "Analysis of the Staging Maneuver and Booster Glideback Guidance for a Two-Staged, Winged, Fully Reusable Launch Vehicle", NASA TP–3335, 1993.

13. Murphy, K. J., Buning, P. G., Pamadi, B. N., Scallion, W. I., and Jones, K. M., "Status of Stage Separation Tool Development for Next Generation Launch Vehicle Technologies," AIAA Paper 2004–2595.

14. Pamadi, B. N., Neirynck, T. A., Covell, P. F., Hotchko, N. J., and Bose, D. M., "Simulation and Analyses of Two-Stage Reusable Launch Vehicles," *Journal of Spacecraft and Rockets*, Vol. 44, No. 1, January–February 2007, pp. 66–80.

15. Pamadi, B. N., Hotchko, N. J., JSamareh, J., Covell, P. F., and Tartabini, P. V., "Simulation and Analyses of Multi-Body Separation in Launch Vehicle Staging Environment," AIAA Paper 2006–8083.

16. Reubush, D. E., Nguyen, L. T., and Rausch, V. L., "Review of X-43A Return to Flight Activities and Current Status," AIAA 2003–7085.

17. "Using ADAMS/Solver," Mechanical Dynamics Inc., 1999.

18. Greenwood, D. T., *Principles of Dynamics*, Prentice-Hall, Englewood Cliffs, NJ, 1965, pp. 267-269.

19. Wang, J. T., and Huston, R. L., "Kane's Equations with Undetermined Multipliers: Application to Constrained Multibody Systems," *Journal of Applied Mechanics*, Vol. 54, No. 2, 1987, pp. 424-429.

20. Anderson, K. S., "An Order n Formulation for the Motion Simulation of General Multi-Rigid-Body Constrained System," *Computers and Structures*, Vol. 43, No. 3, 1992, pp. 565-579.

21. Roithmayr, C. M., and Hodges, D. H., "Identifying Sets of Constraint Forces by Inspection," *Journal of Applied Mechanics*, Vol. 80, No. 2, 2013.

22. Kane, T. R., and Levinson, D. A., *Autolev 4 User's Manual*, OnLine Dynamics, Inc., Sunnyvale, CA, 2005.

23. Brauer, G. L., Cornick, D. E., and Stevenson, R., "Capabilities and Applications of the Program to Optimize Simulated Trajectories (POST)," NASA CR-2770, 1977.

24. Bose, D. M., Toniolo, M. D., Cheatwood, F. M., Hughes, S. J., and Dillman, R. A., "Impact of Vehicle Flexibility on IRVE-II Flight Dynamics," AIAA Paper 2011-2571.

25. Toniolo, M. D., Tartabini, P. V., Pamadi, B. N., and Hotchko, N. J., "Constraint Force Equation Methodology for Modeling Multi-Body Stage Separation Dynamics," AIAA Paper 2008–219.

26. Tartabini, P. V., Roithmayr, C. M., Toniolo, M. D., Karlgaard, C., and Pamadi, B. N., "Modeling Multibody Stage Separation Dynamics Using Constraint Force Equation Methodology," *Journal of Spacecraft and Rockets*, Vol. 48, No. 4, July-August, 2011, pp. 573-583.

27. Baumgarte, J., "Stabilization of Constraints and Integrals of Motion in Dynamical Systems," *Computer Methods in Applied Mechanics and Engineering*, Vol. 1, 1972, pp. 1–16.

28. Roithmayr, C. M., and Hodges, D. H., "Forces Associated with Nonlinear Nonholonomic Constraint Equations," *International Journal of Non-Linear Mechanics*, Vol. 45, No. 4, 2010, pp. 357-369.

29. Roithmayr, C. M., and Hodges, D. H., "An Argument Against Augmenting the Lagrangean for Nonholonomic Systems," *Journal of Applied Mechanics*, Vol. 76, No. 3, 2009, article 034501.

30. Toniolo, M. D., Tartabini, P. V., and Pamadi, B. N., "Implementation of Constraint Force Equation Methodology in POST2 for Simulation of Multi-body Separation Dynamics: User's Guide," To be published as NASA TM.

31. Pamadi, B. N., Tartabini, P. V., Toniolo, M. D., Roithmayr, C. M., Karlgaard, C. D., and Samareh, J. D.; "Application of Constraint Force Equation Methodology for Launch Vehicle Stage Separation," *Journal of Spacecraft and Rockets,* Vol. 50, No. 1, January-February 2013, pp. 191-205.

32. Tartabini, P. V., Bose, D. M., McMinn, J. D., Martin, J. G., and Strovers, B. K., "Hyper-X Stage Separation Trajectory Validation Studies," AIAA Paper 2003–5819.

33. Albertson, A. W., Tartabini, P. V., and Pamadi, B. N., "End-To-End Simulation of Launch Vehicle Trajectories Including Stage Separation Dynamics," AIAA Paper 2012–4863.

REPORT DOCUMENTATION PAGE

1. REPORT DATE *(DD-MM-YYYY)* 01- 07 - 2016	2. REPORT TYPE Technical Publication	3. DATES COVERED *(From - To)*

4. TITLE AND SUBTITLE

Development of Constraint Force Equation Methodology for Application to Multi-Body Dynamics Including Launch Vehicle Stage Separation

5a. CONTRACT NUMBER

5b. GRANT NUMBER

5c. PROGRAM ELEMENT NUMBER

6. AUTHOR(S)

Pamadi, Bandu N.; Toniolo, Matthew D.; Tartabini, Paul V.; Roithmayr, Carlos M.; Albertson, Cindy W.; Karlgaard, Christopher D.

5d. PROJECT NUMBER

5e. TASK NUMBER

5f. WORK UNIT NUMBER
869021.05.07.09.05

7. PERFORMING ORGANIZATION NAME(S) AND ADDRESS(ES)

NASA Langley Research Center
Hampton, VA 23681-2199

8. PERFORMING ORGANIZATION REPORT NUMBER

L-20644

9. SPONSORING/MONITORING AGENCY NAME(S) AND ADDRESS(ES)

National Aeronautics and Space Administration
Washington, DC 20546-0001

10. SPONSOR/MONITOR'S ACRONYM(S)

11. SPONSOR/MONITOR'S REPORT NUMBER(S)
NASA-TP-2016-219326

12. DISTRIBUTION/AVAILABILITY STATEMENT

Unclassified - Unlimited
Subject Category 15
Availability: NASA STI Program (757) 864-9658

13. SUPPLEMENTARY NOTES

14. ABSTRACT

The objective of this report is to develop and implement a physics-based method for analysis and simulation of multi-body dynamics including launch vehicle stage separation. The constraint force equation (CFE) methodology provides a convenient framework for modeling constraint forces and moments acting at joints when the vehicles are still connected. Several test cases involving various types of joints were developed to check and verify the CFE methodology. The results were compared with ADAMS and AUTOLEV, industry standard benchmark codes for multi-body dynamic analysis and simulations. After this check/validation exercise, the CFE algorithm was implemented in POST2 to provide a capability to simulate end-to-end trajectories of launch vehicles including stage separation. The POST2/CFE methodology was applied to the STS-1 Space Shuttle solid rocket booster (SRB) separation and Hyper-X Research Vehicle (HXRV) separation from the Pegasus booster as a further test and validation for application of POST2/CFE methodology for launch vehicle stage separation problems. Finally, to demonstrate end-to-end simulation capability, POST2/CFE was applied to the ascent, orbit insertion, and booster return of a reusable two-stage-to-orbit (TSTO) vehicle concept.

15. SUBJECT TERMS

Launch Vehicle Stage Separation; Multi-Body Dynamics

16. SECURITY CLASSIFICATION OF:			17. LIMITATION OF ABSTRACT	18. NUMBER OF PAGES	19a. NAME OF RESPONSIBLE PERSON STI Help Desk (email: help@sti.nasa.gov)
a. REPORT	**b. ABSTRACT**	**c. THIS PAGE**			
U	U	U	UU	124	**19b. TELEPHONE NUMBER** *(Include area code)* (757) 864-9658

Standard Form 298 (Rev. 8/98)